

Determination of Three Dimensional Time Varying Flow Structures

Samuel Gillooly Raben

A Dissertation submitted to the faculty of the Virginia Polytechnic Institute and State University in partial fulfillment of the requirements for the degree of

Doctor of Philosophy
In
Mechanical Engineering

Pavlos P. Vlachos
Shane D. Ross
Mark R. Paul
Mark A. Stremler
Kenneth S. Ball

08.20.2013
Blacksburg, Virginia

Keywords: Particle Image Velocimetry, Proper Orthogonal Decomposition, Finite Time Lyapunov Exponents, Lagrangian Coherent Structures, Wall Jets

Copyright 2013, Samuel G. Raben

Determination of Three Dimensional Time Varying Flow Structures

Samuel Gillooly Raben

Abstract

Time varying flow structures are involved in a large percentage of fluid flows although there is still much unknown regarding their behavior. With the development of high spatiotemporal resolution measurement systems it is becoming more feasible to measure these complex flow structures, which in turn will lead to a better understanding of their impact. One method that has been developed for studying these flow structures is finite time Lyapunov exponents (FTLEs). These exponents can reveal regions in the fluid, referred to as Lagrangian coherent structures (LCSs), where fluid elements diverge or attract. Better knowledge of how these time varying structures behave can greatly impact a wide range of applications, from aircraft design and performance, to an improved understanding of mixing and transport in the human body.

This work provides the development of new methodologies for measuring and studying three-dimensional time varying structures. Provided herein is a method to improve replacement of erroneous measurements in particle image velocimetry data, which leads to increased accuracy in the data. Also, a method for directly measuring the finite time Lyapunov exponents from particle images is developed, as well as an experimental demonstration in a three-dimensional flow field. This method takes advantage of the information inherently contained in these images to improve accuracy and reduce computational requirements. Lastly, this work provides an in depth look at the flow field for developing wall jets across a wide range of Reynolds numbers investigating the mechanisms that contribute to their development.

Acknowledgements

There are many people I would like to thank that have helped me over the years while I was reaching my goal of obtaining a Ph.D. in mechanical engineering. First, I would like to thank my advisors, Dr. Vlachos and Dr. Ross, whose guidance and support has helped me tremendously. I would also like to thank my committee members who have been very supportive and have been helpful in meetings and discussions about my research.

I want to thank all of my lab mates in the AETHER lab who have helped me out. Specifically I would like to thank John Charonko, Rod La Foy, as well as some former members, Dave Hubble, Kelley Stewart, Chris Wieland, Nick Cardwell and Mike Brady. I would also like to thank all of my friends in Blacksburg, Eric, Andrea, Matt, Jake, Pierce, and Betsy.

The mechanical engineering department staff has also be very helpful to me and I would like to specifically thank, Ben Poe, Jamie Archual, Diana Isreal, Jackie Woodyard, Cathy Hill, Melissa Williams and Mandy Collins. Their help has been instrumental in helping me accomplish my goals and keeping me sane.

I would like to thank my parents for their love and support. They have been extremely supportive in all my endeavors even if they weren't sure they were always the best ideas. I would also like to thank my brother who seems to always have some interesting story about something going on. I would like to thank my in-laws, Jim and Sue, as well as my brother in-law Carl for their help and support over the years.

Most importantly I would like to thank my lovely wife Jaime, who not only agreed to marry me but also agreed to put up with all of my craziness like my addiction to sports and my singing of silly songs. Your love and support are a major reason I was able to accomplish any of this. Thank you.

Table of Contents

Abstract	ii
Acknowledgements	iii
List of Figures	vii
List of Tables	xiii
Attributions	xiv
1. Introduction	1
1.1. Motivation	1
1.2. Objective and Structure of the Dissertation	1
2. Adaptive gappy proper orthogonal decomposition for particle image velocimetry data reconstruction	3
2.1. Abstract	3
2.2. Introduction	3
2.3. Nomenclature.....	7
2.4. Proper Orthogonal Decomposition and Reconstruction Methodologies.....	8
2.4.1. Everson-Sirovich Method.....	9
2.4.2. Venturi-Karniadakis Method.....	10
2.4.3. Reduced POD Method.....	11
2.4.4. Adaptive POD Reconstruction Method.....	11
2.4.5. Convergence Methods.....	12
2.4.6. Additional Reconstruction Methods for Comparison	14
2.5. Velocity Field Data and PIV Processing – DNS of a Turbulent Boundary Layer	16
2.6. Results and Discussion – Turbulent Boundary Layer	19
2.6.1. Adaptive POD Reconstruction	19

2.6.2. Eigenspectra Comparison.....	20
2.6.3. Error Comparison.....	22
2.7. Velocity Field DATA and PIV Processing – Experimental Data Case.....	30
2.8. Results and Discussion – Experimental Case.....	33
2.9. Conclusions	35
2.10. References	37
3. Computation of Finite Time Lyapunov Exponents from Time Resolved Particle Image Velocimetry Data.....	40
3.1. Abstract	40
3.2. Introduction	40
3.3. Flow Map Determination.....	44
3.3.1. Flow Map Computation using Particle Tracking Methods	44
3.3.2. Numerical Particle Trajectory Method.....	46
3.4. FTLE Computation	46
3.5. Synthetic Data.....	47
3.5.1. Artificial Image Generation.....	48
3.6. PIV and PTV Procedure.....	49
3.7. Experimental Data	50
3.8. Results and Discussion	52
3.8.1. Synthetic Data	52
3.8.2. Experimental Data.....	64
3.9. Conclusions	68
3.10. References	69
4. Experimental Three Dimensional Lagrangian Coherent Structures of Inertial Particles in Flows	74

4.1. Abstract	74
4.2. References	82
5. The Developing Region of Wall-Jets	85
5.1. Abstract	85
5.2. Introduction	85
5.3. Experimental Methods and Facilities	88
5.4. Results and Discussion	92
5.4.1. Development Length and Scaling of Streamwise Velocity.....	94
5.4.2. Scaling of $Y^{T,B}_{1/2}$ and $Y_{U_{max}}$ Locations	98
5.4.3. Turbulent Statistics and Scaling	103
5.4.4. Vortex Identification	107
5.5. Conclusion	113
5.6. References	115
6. Conclusions.....	118

List of Figures

Figure 2.1. Vector field from unvalidated PIV with erroneous vectors removed.....	17
Figure 2.2. Convergence data for both the U and V PIV velocity fields, a and b respectively. The X and Y locations chosen for this test were 1024 and 192 pixels respectively.....	18
Figure 2.3. Original and reconstructed field using adaptive POD reconstruction, A) and B) respectively. A horseshoe vortex near the wall produced elevated numbers of erroneous vectors in the PIV processing, (frame 27 in 2003 PIV Challenge set B (Stanislas, Okamoto et al. 2005))	21
Figure 2.4. Spatial distribution of the final mode used by the adaptive POD reconstruction for frame 27.21	
Figure 2.5. Histogram of the final modes used in reconstruction for all of the points. The inset to this figure shows that the maximum mode was used for more than 50% of the gappy locations.	22
Figure 2.6. Eigenspectra Comparison for all of the different reconstructions. The upper right shows a zoomed in portion of the complete figure demonstrating the Eigenspectra divergence in the high modes.	22
Figure 2.7. RMS error for the U and V velocity components, A) and B) respectively. Due to the high error values in the linear interpolation method it is not shown for clarity. Because the E-S method does not rely on information from the previous mode's convergence it is shown with only symbols. The open symbols show the minimum locations in A) of 58, 64, and 58 and in B) of 36, 100, and 36 for Everson – Sirovich, Adaptive POD and Gunes et al. method respectively.....	27
Figure 2.8. Average and RMS error magnitude for all included points, A) and B), and with edge points excluded, C) and D), for the different reconstruction methodologies. The open symbols denote the minimum location in A) of 35, 49, and 38, B) of 26, 42, and 26, C) of 57, 100, and 57, D) of 59, 100, and 59, for the Everson – Sirovich, Adaptive POD, and Gunes et al. method respectively.	28

Figure 2.9. Average and RMS error magnitude for all included points, A) and B) and with edge points excluded C) and D), for the different reconstruction methodologies now solving the linear system proposed by Everson and Sirovich. The open symbols denote the minimum location in A) of 26, 48, and 26, in B) of 26, 44, and 26, in C) 47, 53, and 48, and in D) 48, 53, and 48 for the Everson – Sirovich, Adaptive POD, and Gunes et al. method respectively..... 29

Figure 2.10. Effect of varying gappiness percentages on RMS reconstruction error. The symbol shapes (■, ▲, ▼, ►, ●, ◆) represent gappiness percentages of 5%, 10%, 20%, 40%, 60% and 80% respectively. The closed symbols belong to the Adaptive POD reconstruction while the open symbols belong to the Gunes et al. method. Kriging is shown with a dashed line with only every 4th symbol shown for clarity..... 30

Figure 2.11. Schematic for vertical water tunnel facility showing the lower receiving chamber and test section..... 32

Figure 2.12. Vector field from the original (A) and gappy field (B) from the turbulent channel experiment. The contour is vertical velocity (V). 33

Figure 2.13. Cumulative sum of the eigenspectra for the turbulent channel flow field. The inset shows a zoomed in look at the first 70 modes. 33

Figure 2.14. Reconstructed field after 70 modes using the adaptive POD reconstruction. Visually no discernable difference can be seen when compared to the original field..... 34

Figure 2.15. Average and RMS error for reconstruction of the turbulent channel flow field. The closed symbols denote average error while the open symbols are RMS. 35

Figure 3.1. Flow chart showing the common procedure for computation of the FTLEs from experimental data and our novel procedure denoted with the red dashed line. 43

Figure 3.2. Vector field snap-shot of the double gyre flow field.....	48
Figure 3.3. Resulting FTLE field from using the benchmark flow field. This field will be used as the basis of comparison for the synthetic data analysis.	52
Figure 3.4. FTLE results for the 500 particles case where A), B) and C) represent numerical integration of the PIV velocity fields, sequential Lagrangian tracking, and the PTV flow map interpolation method respectively.....	55
Figure 3.5. FTLE results for the 5000 particles case where A), B) and C) represent numerical integration of the PIV velocity fields, sequential Lagrangian tracking, and the PTV flow map interpolation method respectively.....	56
Figure 3.6. FTLE results for the 20000 particles case where A), B) and C) represent numerical integration of the PIV velocity fields, sequential Lagrangian tracking, and the PTV flow map interpolation method respectively.....	57
Figure 3.7. Normalized average (A) and Root-Mean-Squared (RMS) (B) error for all three of the methods tested.....	59
Figure 3.8. Separatrix analysis for the case of 500 particles. The solid grey line represents the separatrix from the benchmark solution.....	61
Figure 3.9. Separatrix analysis for the case of 5000 particles. The solid grey line represents the separatrix from the benchmark solution.....	61
Figure 3.10. Separatrix analysis for the case of 20000 particles. The solid line represents the separatrix from the benchmark solution.....	62
Figure 3.11. Percent overlap between the measure and true separatrix for the different methods.	63

Figure 3.12. Hausdorff distance for all three methods compared with the solution.	64
Figure 3.13. Velocity field with the corresponding vorticity field magnitude calculated from PIV data for the experimental laminar vortex ring.	65
Figure 3.14. Results for the experimental data from a laminar vortex ring. A), B), and C) show the FTLE results for the numerical integration, sequential Lagrangian tracking, and the PTV flow map interpolation respectively.	67
Figure 3.15. Separatrix overlaid with the non-dimensional vorticity field for the numerical integration (A) and the PTV flow map interpolation (B).....	68
Figure 4.1. Normalized particle diameter distribution within the measurement volume.....	78
Figure 4.2. Iso-surfaces of the forward (A) and backward (B) FTLE fields based on the different components in the flow.	80
Figure 4.3. Contours of Backward time FTLE values for the total location of particles A), the small particle sizes B) the medium particles sizes C) and finally the large particle sizes, D). The thick line shows iso-contour for -3 std (surface shown in Figure 4.2), while the thick line shows an iso-contour for -1.5 std and the dashed line is the zero iso-contour.....	81
Figure 5.1. Diagram showing the two vertical locations used for scaling. The top and bottom regimes are the locations where the U velocity is one half the maximum.	87
Figure 5.2. Experimental Setup. The red box represents the field of view of the camera while the green line is the laser plane entering from the right.....	90
Figure 5.3. Time average velocity profiles for different Reynolds numbers at different X/H locations: A) X/H=1, B) X/H = 4, C) X/H = 8, D) X/H = 11.	94

Figure 5.4. Development length as a function of Reynolds number.....	96
Figure 5.5. Decay of streamwise velocity as a function of distance (A), and decay of maximum velocity scaled by the growth of the $Y_{\frac{1}{2}}^T$ (B). In (A) and (B) markers are shown at only every 10 th measurement location for clarity. The development length for each case is noted in (A) with a vertical line using the same line markers at either end.	97
Figure 5.6. Growth the $Y_{\frac{1}{2}}^T$ height as a function of streamwise distance, (A), as well Growth of the $Y_{\frac{1}{2}}^B$ height as a function of streamwise distance. For each Reynolds number only every 10 th marker is shown for clarity.....	99
Figure 5.7. Growth of the momentum thickness of the wall jet, where markers are shown at only every 10 th measurement location for clarity.....	100
Figure 5.8. Growth of $Y_{\frac{1}{2}}^B$ normalized by the momentum thickness as a function of streamwise location normalized by the development length (A). (B) provides a zoomed in look at the early lengths....	101
Figure 5.9. Ratio of profile velocity at the momentum thickness to the maximum U velocity. (B) provides a zoomed in view of (A).....	102
Figure 5.10. Location of U_{\max} as a function of streamwise location.	103
Figure 5.11. Profiles of streamwise velocity fluctuation, u' , normalized by the exit velocity, U_0 , for down stream distances of $X/H = 1$ (A), $X/H = 4$ (B), $X/H = 8$ (C), and $X/H = 10$ (D).	104
Figure 5.12. Profiles of wall normal velocity fluctuation, v' , normalized by the exit velocity, U_0 , for down stream distances of $X/H = 1$ (A), $X/H = 4$ (B), $X/H = 8$ (C), and $X/H = 10$ (D).	105

Figure 5.13. Locations of maximum streamwise, u' , and wall normal, v' , Reynolds stress normalized by the $Y^T_{1/2}$ and $Y^B_{1/2}$ locations. A) and B) show maximum u' locations normalized by the $Y^T_{1/2}$ and $Y^B_{1/2}$ heights respectively while C) show locations for v' normalized by $Y^T_{1/2}$ 107

Figure 5.14. Snap shots of near wall vortex ejection for the Re 1000 case. The color contour shows normalized vorticity while the white circles indicate vortices identified with the λ_{ci} method. The iso-contour lines enclose Q2 events that are seen in the field..... 109

Figure 5.15. Histogram of burst versus their vertical location scale by $Y^T_{1/2}$ (A) and $Y^B_{1/2}$ (B). 110

Figure 5.16. Normalized histograms for the vortex locations in the vertical direction with the vertical axis normalized by the $Y^T_{1/2}$ and $Y^B_{1/2}$ respectively..... 111

Figure 5.17. Normalized histogram of normalized circulation strengths for the different Reynolds numbers(A) as well as peak circulation values from the histogram (B), and their relative contribution in the distribution (B). The open symbols show negative circulation (clock wise rotation) while the closed symbols represent positive circulation (counter-clock wise rotation) 113

List of Tables

Table 2.1. Processing times for the different POD reconstruction. Due to computational expense, only the first 70 modes were reconstructed using the linear system while all of the modes were reconstructed using the POD coefficients.	26
Table 2.2. Error values for the different methods at 36 modes which corresponds to the minimum using the Gunes et al. convergence method, and 70 modes which is the maximum number of modes reconstructed using the linear system of equations.	27
Table 5.1. Experimental Parameters.	89

Attributions

This dissertation is composed of an introduction, four main chapters and a conclusion. The four chapters are written in journal format and either have or will be submitted to archival journals for separate publication. The following individuals are co-authors on one or more chapters.

Dr. Pavlos P. Vlachos Ph.D. – (Professor in Mechanical Engineering, Virginia Tech) served as a committee co-chair and has provided advice on the works presented in each chapter. Dr. Vlachos is a co-author on each of the papers.

Dr. Shane D. Ross Ph.D. – (Associate Professor in Engineering Science and Mechanics, Virginia Tech) served as a committee co-chair and provided advice on the works presented in each chapter. Dr. Ross is a co-author on chapters 3 and 4.

Dr. John J. Charonko Ph.D. – (Research Assistant Professor in Mechanical Engineering, Virginia Tech) Dr. Charonko was instrumental in helping with the development of the Gappy Data Reconstruction. Dr. Charonko is co-author on chapter 2.

1. Introduction

1.1. Motivation

Time varying flow structures are an important part of fluid mechanics. They play important roles in the transport, mixing and development of a large number of fluid flow environments. However, while their importance is relatively well known, their behavior is not fully understood. The difficulty in understanding these structures is partially limited by a lack of accurate measurement methods capable of studying such flow environments. This work provides novel methodologies to improve investigations of these time varying structures, a demonstration in a fully turbulent three-dimensional flow field, as well as a study of the development region of turbulent wall jets.

1.2. Objective and Structure of the Dissertation

The objective of this work is to provide improved measurement methodologies for detecting and studying time varying flow structures in both two-dimensional and three-dimensional flow fields. To accomplish this effort, four separate studies were undertaken which resulted in the four main chapters of my dissertation. This section provides a brief discussion of the work performed in each of the chapters.

Experimental data can often be affected by erroneous measurements, which in some cases can misrepresent the true results. Proper orthogonal decomposition (POD) is a method that can be used to replace these erroneous measurements and improve the accuracy of the data set. Chapter 2 provides the methodology as well as a demonstration for applying “Gappy” POD to experimental data. This method has shown that when sufficient information is provided, high accuracy reconstruction can be achieved to outperform methods typically used for data reconstruction.

The use of finite time Lyapunov exponents (FTLE) is one method to investigate complex time depended flow structures. The method is performed by determining the flow map for a given field, which describes the motion of a fluid element or particle over a fixed period of time. Chapter 3 provides a novel

methodology for directly determining the FTLE field from the information that is inherently contained in experimental particle image data. Through the use of particle tracking, this method removes the requirement of numerical integration for the determination of the field's flow map. This method is not only more computationally efficient in comparison to conventional techniques, but is also shown to produce improved accuracy when particle seeding is reduced.

Chapter 4 demonstrates the use of particle tracking for determining flow maps on inertial particles in a turbulent three-dimensional flow field. Through the use of tomographic imaging, neutrally buoyant flow tracers as well as inertial particles were simultaneously imaged. Using a similar methodology to that described in Chapter 3, this work demonstrates the ability to determine the flow maps, and thus the FTLE field for inertial particles and shows a difference in behavior between the different types of particles. This work also compares the behavior of the inertial particles as denoted by the FTLE fields with standard methods that have been used previously to describe particle behavior in turbulent environments.

In the final chapter, the development region for a wall jet was studied for a wide range of Reynolds numbers. Although wall jets are utilized in many engineering applications, few studies have investigated their behavior in the development region. The majority of previous studies have focused their attention on the fully developed region where self-similar behavior exists and scaling with streamwise location and Reynolds number becomes more simplistic. This work however, focuses on the development region of the wall jet and investigates the effect of momentum transfer from the core of the jet on the different scaling parameters that are used to describe wall jets. This work also provides new scaling relationships as a function of Reynolds number in the development region.

The following chapters are presented in journal format with the second Chapter accepted into archival publication in Measurement Science and Technology. The remaining chapters have been or are in the processes of being submitted for publication.

2. Adaptive gappy proper orthogonal decomposition for particle image velocimetry data reconstruction

By Samuel G. Raben, John J. Charonko, Pavlos P. Vlachos

The following is article that has been published Measurement Science and Technology

2.1. Abstract

This work presents a novel method for replacing erroneous measurements in Digital Particle Image Velocimetry (DPIV) data using an adaptive reconstruction with gappy Proper Orthogonal Decomposition (POD). Previous studies have shown that gappy POD can be used to replace erroneous data with high accuracy. Conventional gappy POD methods employ a spatially constant number of modes for reconstructing the missing information across the entire field. In contrast, the method presented herein proposes a locally adaptive criterion that allows for determination of the optimum number of POD modes required for the reconstruction of each replaced measurement. This reconstruction produces higher accuracy results using more POD modes than with previous POD methods. The new method was compared against commonly utilized techniques for DPIV vector replacement, namely Kriging, bootstrapping, and basic interpolation, as well as previously presented POD reconstruction techniques. The results showed that the adaptive gappy POD reconstruction provides higher accuracy and robustness.

Keywords: DPIV, Proper Orthogonal Decomposition, Outlier Replacement.

2.2. Introduction

Proper Orthogonal Decomposition (POD) is a method for producing reduced order representations of high order systems. It has been shown that this method can also be useful in reconstructing missing data from incomplete datasets (Everson and Sirovich 1995; Venturi and Karniadakis 2004). Properly calculated, these reconstructions have been shown to produce superior estimations of the missing data, even when compared to spatial interpolation techniques such as Kriging (Venturi and Karniadakis 2004;

Gunes, Sirisup et al. 2006; Venturi 2006; Druault and Chaillou 2007). However, these gappy POD methods are subject to several practical limitations. When applied to experimental data, where the true solution is not known a-priori, it is difficult to determine a convergence criterion based on the eigenspectrum of the modes. Moreover, the convergence of the reconstruction is based on the whole field of data, without any consideration to the spatial variations present (Venturi and Karniadakis 2004). In addition, the method can be impractical because of excessive computational cost (Murray and Ukeiley 2007; Lee and Mavris 2010), and its accuracy can be limited if assumptions are made about the data as a whole (Gunes, Sirisup et al. 2006). This work aims to develop a novel gappy POD implementation for improving the estimation of the individual replacement values, improve on the accuracy of these reconstructions and reduce the computational costs.

Everson and Sirovich first proposed the idea of using POD to reconstruct missing or “Gappy” data in 1995 (Everson and Sirovich 1995). Images were reconstructed using two different methods: first, the reconstruction was based on information from the complete solution; and second, the reconstruction was independent of the “true” solution. Neither of these reconstruction methods, however, provides a criterion for determining the optimum reconstruction. Venturi and Karniadakis showed that the use of an iterative POD reconstruction with gappy data (“Gappy POD”) provides a more accurate reconstruction with a larger number of resolved POD modes than with previous methods (Venturi and Karniadakis 2004). It is important to note that their method depended on knowledge of the “true” field in order to determine an “optimal ” reconstruction, which renders its direct implementation impractical for reconstruction of experimental velocity fields. It has also been shown that the accuracy of this method is dependent on the amount of temporal information available during reconstruction (Gunes, Sirisup et al. 2006). Subsequently, Gunes et al. proposed an approach for termination of Venturi and Karniadakis’ method that would make the reconstruction applicable to experimental data. This method stated that by selectively removing an additional percentage of the good data, the relative error in the reconstruction could be quantified and monitored and thus provide information on the relative error of the complete

reconstruction (Gunes, Sirisup et al. 2006). While this method provided a convergence point for the reconstruction, the technique required that all of the gappy points in the data be reconstructed using the same amount of information, i.e. the same number of modes is necessary for all of the gappy points. In the work presented here, we will show that the aforementioned convergence does not always produce the highest accuracy solution, and we will present an alternative approach that addresses this limitation and is applicable to experimental data.

For experimental measurements, gappy fields are generated when erroneous measurements are detected in a data set. Because erroneous measurements are always present in experimental data, the need for recovery and reconstruction of these measurements is common. In particular, Digital Particle Image Velocimetry (DPIV) is subject to invalid measurements due to not only experimental error, but processing error as well, and therefore, there is typically a need to perform measurement validation and outlier removal (Huang, Dabiri et al. 1997; Hart 1998; Hart 2000; Westerweel and Scarano 2005; Pun, Susanto et al. 2007). Advancements in PIV processing have helped to reduce correlation errors (Eckstein, Charonko et al. 2008; Eckstein and Vlachos 2009b); however, inhomogeneous seeding and varying image intensity would still produce incorrect measurements (Hart 1998; Eckstein and Vlachos 2009b; Fore 2010).

Regardless of the source, the problem of identifying erroneous measurements and outliers is endemic to DPIV work, and various techniques for solving this problem have been proposed (Westerweel 1994; Vedula and Adrian 2005; Westerweel and Scarano 2005; Pun, Susanto et al. 2007). One of the most common methods used in DPIV for detection of bad measurements is a linearly weighted spatial validation where individual measurements are compared with their neighbors (Westerweel and Scarano 2005). Both linear temporal and advanced nonlinear temporal validation methods have also been implemented for DPIV data (Fore, Tung et al. 2005). While both approaches help to improve overall measurement accuracy, validating spatially without concern for temporal information limits their effectiveness with the same being said for validating temporally alone. For temporal validation to be effective, the time scale of the validation window must be on the same order or smaller than the scale of

physical events in the flow. While this is sometimes possible, many cases exist where this requirement would not be satisfied (Murray and Ukeiley 2007; Murray and Seiner 2008). Despite its importance, the validation procedure will not be considered in this paper and accepted methodologies will be implemented as needed. Instead, the replacement of missing data in PIV fields will be our focus.

Once bad measurements have been identified, the task then becomes how best to replace these measurements. One option is a simple linear interpolation of the surrounding points, which while providing limited accuracy is very robust (Nogueira, Lecuona et al. 1997). With the growth of computational power, higher order replacement techniques are becoming feasible. Kriging is an advanced spatial interpolation method that can produce high accuracy results (Oliver and Webster 1990; Myers 2002; Gunes, Sirisup et al. 2006). Kriging is a form of a least squares estimator that takes advantage of radial basis functions for the interpolation (Gunes, Sirisup et al. 2006; Gunes and Rist 2007). Kriging first became popular in the geophysical community where interpolation between highly scattered data was required (Oliver and Webster 1990; Myers 2002). The technique has also been used for more densely populated experimental data such as PIV to replace erroneous measurements (Gunes and Rist 2007; Gunes and Rist 2008). Principle Component Analysis (PCA) is another decomposition technique that has shown the ability to repair missing experimental data (Tipping and Bishop 1999). By combining PCA with an Expectation Maximization algorithm it is possible to recover missing information as well as account for noise in the original measurements (Tipping and Bishop 1999). While having some inherent differences, these two techniques, POD and PCA, have been shown to produce similar results (Lee and Mavris 2010). However, only POD-based approaches will be considered in this paper.

The work described herein proposes a new approach based on the Venturi and Karniadakis method (Venturi and Karniadakis 2004), as discussed previously, for the reconstruction of DPIV fields that does not require any *a-priori* information about the true solution and allows individual points to converge independently from the remainder of the gappy field. The method assumes that an appropriate “outlier vector” identification scheme is available and has already correctly identified the bad measurements in the

field. The performance of the method is characterized through comparisons using different POD reconstruction methods as well as standard interpolation techniques.

2.3.Nomenclature

$U(\vec{x})$	Measured velocity field.
$\phi(\vec{x})$	POD eigenfunction.
λ	Eigenspectra produced from POD.
$K_{i,j}$	Discrete correlation matrix for POD calculation.
U_i	Discrete velocity field
$\phi^{(s)}$	POD eigenfunction determined using method of snapshots
$\alpha^{(s)}$	POD projection coefficient associated with the method of snapshots
$F_{n,l}$	Kernel for the method of snapshots reduced eigenvalue problem.
\tilde{U}	Reconstructed velocity field.
\hat{U}	Velocity field with the gappy locations filled in with the ensemble average values.
\bar{U}	Intermediate reconstructed velocity field maximizing the local smoothness
P	Covariance matrix of the POD eigenfunctions.
L	Cross covariance matrix between the reconstruction velocity and the eigenfunctions.
$\hat{\zeta}$	Projection coefficients from the linear system of equations.
$M(x, y; t)$	Mask locating correct (0) and bad data (1).
$E(U)$	Measure of the smoothness for the available velocity field information U.
ϵ	Measure of the error for the reconstructed fields.
σ^2	Total variance from the velocity information.
$\langle \cdot \rangle_t$	Ensemble Average. Here the ensemble average was taken with respect to time.

⊗ Outer product used to create the kernel used for the POD formulation.

2.4. Proper Orthogonal Decomposition and Reconstruction Methodologies

For completeness, the basics of Proper Orthogonal Decomposition using the method of snapshots will now be described. For more in-depth treatment, the reader is referred to prior works on the subject (Sirovich 1989; Everson and Sirovich 1995; Zoldi and Greenside 1997; Venturi and Karniadakis 2004; Murray and Ukeiley 2007). The basic formulation of POD starts with the Fredholm integral in equation 1,

$$\int \langle U(\vec{x}) \otimes U(\vec{x}') \rangle \phi(\vec{x}') d\vec{x}' = \lambda \phi(\vec{x}) \quad (1)$$

where the eigenfunctions, ϕ , are the orthogonal modes that represent the data defined by U.

To apply POD to discrete data, as would be done with experimental data, the equation must be discretized, as shown in equation 2. Here, $\mathbf{K}_{i,j}$ is the two point correlation tensor which is an ensemble average over the total number of frames or snapshots (equation 3).

$$\sum_p \sum_q K_{i,j}(x, y; p, q) \phi_j^{(s)}(p, q) = \lambda^{(s)} \phi_i(x, y)^{(s)} \quad (2)$$

$$K_{i,j} = \langle U_i(x, y; t) U_j(x, y; t) \rangle_t \quad (3)$$

To minimize computation time, the method of snapshots is used (Sirovich 1987). The method assumes that the eigenfunctions created in equation 2 are a linear combination of the flow field snapshots multiplied by a corresponding projection coefficient.

$$\phi_j^{(s)}(x, y) = \sum_t \alpha^{(s)}(t) U_j(x, y; t) \quad (4)$$

Applying the method of snapshots, equation 4, to equation 2, a reduced eigenvalue problem is produced (equation 5) with equation 6 representing the kernel.

$$\sum_n F_{n,l} \alpha^{(s)}(n) = \lambda^{(s)} \alpha^{(s)}(l) \quad (5)$$

$$F_{n,l} = \frac{1}{N} \sum_x \sum_y U_i(x, y; n) U_j(x, y; l) \quad (6)$$

Because of the orthogonality of the eigenfunctions, equation 4 can be rearranged to solve for the reconstructed flow field (equation 7), where s is the number of snapshots used in reconstruction.

$$\tilde{U}_t(x, y; t) = \sum_s \alpha^{(s)}(t) \phi_i^{(s)}(x, y) \quad (7)$$

Before POD can be utilized as a missing data reconstruction method, the locations of the missing data must be identified. These locations will be stored in a mask variable shown in equation 8 wherein good measurements are denoted with a 0 and bad measurement are equal to 1.

$$M(x, y; t) = \begin{cases} 0 & \text{for locations of correct data} \\ 1 & \text{for locations of missing data} \end{cases} \quad (8)$$

2.4.1. Everson-Sirovich Method

Everson and Sirovich, who were the first to propose data reconstruction using POD, used the above methodology adding additional steps to reconstruct the missing points (Everson and Sirovich 1995). This method will be referred to as the E-S method from hereon.

- i. Begin with ensemble average values as initial guesses at $\mathbf{M}(\mathbf{x}, \mathbf{y}; \mathbf{t}) = \mathbf{1}$ to produce $\hat{\mathbf{U}}(\mathbf{x}, \mathbf{y}; \mathbf{t})$ for s snapshots. Because POD is only applied to the fluctuating component of the velocity, the initial value estimates are set to zero;
- ii. Perform POD on $\hat{\mathbf{U}}(\mathbf{x}, \mathbf{y}; \mathbf{t})$ to produce s spatial modes with corresponding projection coefficients;
- iii. Construct the matrix $[\mathbf{P}]_{i,j} = (\phi_i^{(s)}, \phi_j^{(s)})_{M=0}$ and $[\mathbf{L}]_i = (\tilde{U}, \phi_i^{(s)})_{M=0}$;
- iv. Solve the linear system $\mathbf{P}\tilde{\zeta} = \mathbf{L}$, for the new projection's coefficients, $\tilde{\zeta}$;
- v. Using equation 7, reconstruct the field using the new projection's coefficients and the determined number of modes, \mathbf{N} ;

$$U_N(x, y; t) = \sum_N \tilde{\zeta}^{(s)}(t) \phi^{(s)}(x, y)$$

- vi. Overwrite previous guess with the newly constructed field $\tilde{\mathbf{U}}(\mathbf{x}, \mathbf{y}; \mathbf{t}) = \mathbf{U}_N(\mathbf{x}, \mathbf{y}; \mathbf{t})$ only if $\mathbf{M}(\mathbf{x}, \mathbf{y}; \mathbf{t}) = \mathbf{1}$.
- vii. If the solution has converged, stop, otherwise return to step (ii).

Convergence is determined by a point-wise comparison of the eigenspectra from the current and previous iteration. This comparison is synonymous with iterating until the fields themselves stop changing between steps. This technique has been shown to work for repairing missing data, (Everson and Sirovich 1995; Tan, Willcox et al. 2003; Murray and Ukeiley 2007) and as N is increased, an optimum reconstruction is reached (Venturi and Karniadakis 2004). As highlighted previously, however, the method does not establish a metric for determining the optimum number of modes and is computationally expensive due to the linear system of equations that needs to be solved in step 4 (Tan, Willcox et al. 2003). This method is also affected by the initial guess used in the reconstruction but has been shown to produce the most accurate results when the time averaged data is used (Venturi and Karniadakis 2004).

2.4.2. Venturi-Karniadakis Method

Venturi and Karniadakis proposed an extension of this reconstruction method eliminating the dependence on the initial guess as well as increasing the resolvable number of modes. For brevity, this method will be referred to as the V-K method and consists of the following steps (Venturi and Karniadakis 2004);

1. Perform the standard E-S method employing only two modes ($N=2$) in the reconstruction;
2. Using the converged results from the previous step as a new initial guess, repeat the reconstruction now using 3 modes ($N=3$);
3. Proceed similarly for the n^{th} iteration until the eigenvalues no longer change.

In using the converged information from the previous mode, Venturi and Karniadakis increased the resolvable number of modes by as much as an order of magnitude in some cases (Venturi and Karniadakis 2004). However, this method lacks an inherent criterion for determining convergence when applied to experimental data. Convergence was determined by monitoring the divergence of the new eigenspectra from that of the “true” solution. However, this requirement limits the applicability of the method on data sets without known “true” solutions such as experimental cases. Methods to overcome this limitation including an improved reconstruction procedure will be described in sections 3.3-3.5 below.

2.4.3. Reduced POD Method

Previous works have also looked at using POD reconstruction without solving the linear system of equations for the new projection coefficients (steps three through six of the E-S method) (Gunes, Sirisup et al. 2006; Murray and Seiner 2008). This variation consisted of repairing data using \tilde{U}_i from equation 7, and has been shown to be much more computationally efficient as well as producing higher accuracy reconstruction when used in conjunction with PIV data (Murray and Seiner 2008). This method was first proposed by Gunes et al. and therefore will be referred to as the Gunes method.

$$\tilde{U}(x, y; t) = \begin{cases} U_i(x, y; t) & \text{at } M(x, y; t) = 0 \\ \tilde{U}_i(x, y; t) & \text{at } M(x, y; t) = 1 \end{cases} \quad (9)$$

2.4.4. Adaptive POD Reconstruction Method

In this section, we will show that an increase in accuracy can be achieved if the individual points in the field are allowed to converge adaptively through the use of a field smoothness parameter. This adaptive reconstruction allows for spatially varying features of the flow to be reconstructed with a varying number of modes. This method will be referred to as AR-POD.

In order to implement this new approach a modified reconstruction procedure is necessary. This modified reconstruction procedure consists of the following steps.

1. Begin with time average values as initial guesses at $M(x, y; t) = 1$ to produce $\hat{U}(x, y; t)$ for s snapshots;
2. Determine the initial field smoothness, $E(\hat{U})_{M=1}$ (an equation for smoothness will be provided in the next section).
3. Perform POD on $\hat{U}(x, y; t)$ to produce s spatial modes with corresponding projection coefficients;
4. Reconstruct the field using equation 9 from the Gunes method using $N=2$ modes to produce a complete field, $\tilde{U}(x, y; t)$;
5. Repeat steps ii and iii using $\tilde{U}(x, y; t)$ as the new guess until the fields converge.
6. Evaluate the field smoothness at all gappy locations, for both the new reconstructions, $E(\tilde{U})_{M=1}$, and the previous best points, $\hat{E}(\hat{U})_{M=1}$;
7. Create a new reconstruction where the gaps are filled using

$$\overline{U}_N(\mathbf{x}, \mathbf{y}; t) = \begin{cases} \hat{U}_N(\mathbf{x}, \mathbf{y}; t) & \text{if } E_N(\tilde{U})_{M=1} > \hat{E}_N(\hat{U})_{M=1} \\ \tilde{U}_N(\mathbf{x}, \mathbf{y}; t) & \text{if } E_N(\tilde{U})_{M=1} \leq \hat{E}_N(\hat{U})_{M=1} \end{cases}$$

8. Repeat steps v and vi until \overline{U}_N converges, then set $\tilde{U}(\mathbf{x}, \mathbf{y}; t) = \overline{U}_N(\mathbf{x}, \mathbf{y}; t)$;
Set $\hat{U}(\mathbf{x}, \mathbf{y}; t) = \tilde{U}(\mathbf{x}, \mathbf{y}; t)$ and return $\tilde{U}_N(\mathbf{x}, \mathbf{y}; t) = \begin{cases} U_N(\mathbf{x}, \mathbf{y}; t) & \text{if } E_N(\tilde{U})_{M=1} > \hat{E}_N(\hat{U})_{M=1} \\ \tilde{U}_N(\mathbf{x}, \mathbf{y}; t) & \text{if } E_N(\tilde{U})_{M=1} \leq \hat{E}_N(\hat{U})_{M=1} \end{cases}$
9. Replace the value of \hat{E} with those of E_N at the locations where \tilde{U} was replaced;
10. Return to step ii increasing the number of modes used by 1, ($N=3,4,\dots$).

The reconstruction process will be repeated until all of the available modes are used. It is important to note that gappy locations may be replaced at any time if E_N has reached a new minimum. This means that a location may be updated on some iterations, but not on others.

It should be mentioned that there are limitations to all POD methodologies. First, these methods cannot resolve an area obstructed in every snapshot (Venturi and Karniadakis 2004; Gunes, Sirisup et al. 2006), although for symmetric fields, measurements can sometimes be determined in such regions (Ma, Karniadakis et al. 2003). Secondly, such techniques also have the constraint that a snapshot cannot be missing, i.e. the field cannot be completely ‘‘gappy’’ in a single snapshot (Venturi and Karniadakis 2004; Gunes, Sirisup et al. 2006). In either of these cases, reconstruction of the missing information is not possible.

2.4.5. Convergence Methods

Determining convergence or termination for these methods is of critical importance to their accuracy. For the E-S method, Venturi and Karniadakis proposed that optimum reconstruction is obtained when total energy of the eigenspectra has reached a maximum (Venturi and Karniadakis 2004). To this end, they used equation 10, which is the sum of the squared eigenvalues after each reconstruction where N is the number of modes used in the reconstruction. Once all of the reconstructions are calculated, this equation can be used to retroactively select the reconstruction that produces the maximum value.

$$e(N) = \sum_{j=1}^N \lambda_N^2 \tag{10}$$

Gunes et al. proposed a method for determining an optimum reconstruction for the V-K method as well as their reduced reconstruction POD (Gunes, Sirisup et al. 2006). They suggested that by removing an additional 1-3% of good vectors from the field, the relative error associated with them could be evaluated and would be used as an estimate for determining the optimum mode for reconstruction of the entire field.

For the AR-POD method, convergence is performed concurrently with the reconstruction using the smoothness parameter from equation 11.

$$E(U) = \left(\frac{\partial^2 u}{\partial x^2}\right)^2 + 2\left(\frac{\partial^2 u}{\partial x \partial y}\right)^2 + \left(\frac{\partial^2 u}{\partial y^2}\right)^2 + \left(\frac{\partial^2 v}{\partial x^2}\right)^2 + 2\left(\frac{\partial^2 v}{\partial x \partial y}\right)^2 + \left(\frac{\partial^2 v}{\partial y^2}\right)^2 \quad (11)$$

The smoothness parameter chosen for this work has been shown to be a good measure of field smoothness and has previously been used in conjunction with Radial Basis Functions for data interpolation (Powell 1992; Karri, Charonko et al. 2009). The use of this parameter is contingent to the assumption that the field is locally smooth, i.e. the velocity resolution is adequate for resolving the structures present in the flow field.

When determining smoothness, the local value for each previously reconstructed point was evaluated ($\hat{E}_N(\hat{U})_{M=1}$), one location at a time, filling in any surrounding gappy points with values from the current best approximation (\overline{U}_N). This smoothness value was compared to the smoothness at the same location calculated using each newly reconstructed value ($E_N(\tilde{U})_{M=1}$), surrounded again by points from the current best approximation. This process should be repeated, replacing at each location points of increasing smoothness until the field no longer changes, i.e. an iterative approach. The result will be a mixture of old and new points that gives the best overall field smoothness. An alternative to this approach that was also considered, although not shown here, was to simultaneously evaluate the smoothness of the entire field using all the points from the current iteration (\tilde{U}) and compare that to the smoothness originally calculated from the previous field (\hat{U}). The value with the best smoothness at each

point would then be selected without regard to the surrounding values. It was seen that this method provided lower reconstruction error for some fields, but this was due in part to the fact that the center of gappy clusters could be biased to the lower, and smoother, modes. However, when the same method was applied to experimental data with groups with more than one adjacent outlier, the centers of these clusters often remained at a low mode number while the edges continued to update, leaving what appeared as outliers in the field. For this reason, this alternative method was not included in the analysis herein.

2.4.6. Additional Reconstruction Methods for Comparison

In order to determine the effectiveness of the newly proposed reconstruction methodology, AR-POD was compared against other accepted reconstruction methodologies for PIV. It is common in PIV data to identify bad measurements through a statistical detection process (Westerweel 1994; Westerweel and Scarano 2005). Following this identification, either a statistical replacement or an interpolation is typically performed to fill in the missing data. This work compares POD reconstruction with both linear and higher order interpolation (Lophaven, Nielsen et al. 2002) as well as a bootstrapping algorithm (Pun, Susanto et al. 2007) specifically designed for PIV data.

The most basic replacement method used here was a simple linear interpolation where after each gappy point was identified, a surrounding grid of 7×7 points was used to linearly interpolate back the value at the missing location. A 7×7 grid was chosen as it provided enough points to achieve statistical significance while not encompassing too large an area, which could result in over smoothing of the field. A visual inspection before and after reconstruction was performed, as is common with PIV data, to insure that data was not becoming over-smoothed. If bad measurements are contained in the surrounding points, they are removed before the interpolation is done so that only valid points are contributing. This process was also designed so that, at a minimum, three good measurements were used and, if needed, the window was enlarged in order to ensure this fact. This simple linear interpolation method works well when the field is smooth and contains only low frequency spatial features. As field variations increase, their spatial frequency increases and the method becomes ineffective.

As previously discussed, Kriging is a higher order interpolation method that has been shown to be highly effective at interpolating data (Lophaven, Nielsen et al. 2002; Gunes, Sirisup et al. 2006). This interpolation was implemented in MATLAB using the DACE toolbox and used a second order polynomial for the regression, in conjunction with a Gaussian correlation model (Lophaven, Nielsen et al. 2002). These parameters were shown in other studies to provide the best interpolations given that the data is continuously differentiable (Venturi and Karniadakis 2004; Gunes, Sirisup et al. 2006). The interpolation was implemented both locally and for the full field. The local interpolation was performed similarly to the linear interpolation described above. For local Kriging a larger stencil, 11x11, (compared to the 7x7 used for the linear interpolation) was used, as Kriging requires a larger number of points for use in the regression model. Smaller stencils were tested (5x5, 7x7, 9x9) but they yielded higher average errors (0.5599, 0.4797, 0.1129 respectively) than the 11x11 stencil (average error of 0.0825). Because the full field Kriging had an average error of 0.0805, the 11x11 stencil provided a good choice for producing the high-accuracy results while limiting computational cost. Again, the surrounding good points were used to generate the model and then individual points were interpolated back with a minimum of 8 good points, otherwise the stencil was expanded. For the full field interpolation, all of the valid measurements across the entire field in a single frame were used to approximate back all of the missing locations simultaneously. This approach proved to be far more computationally expensive than local Kriging and did not produce better results, particularly as the ratio of good measurements to interpolation sites increased.

An iterative interpolation method using bootstrapping was also used to evaluate the missing locations (Pun, Susanto et al. 2007). This method removes a small random sample of points from the field, which were used to interpolate back an estimate of the complete field. This process was repeated until a large number of interpolations were generated at each point. Using the statistical distribution of these samples at each point, a measurement can be determined to be erroneous, as well as simultaneously provide an estimate of its correct value. It is important to note that while this method will also inherently detect

erroneous measurements, only the predetermined locations for the bad measurements were replaced in the error analysis.

2.5. Velocity Field Data and PIV Processing – DNS of a Turbulent Boundary Layer

In order to test the proposed methodology, the data from a Direct Numerical Simulation (DNS) of a turbulent boundary layer used to generate artificial PIV images for the 2003 PIV challenge (Stanislas, Okamoto et al. 2005) were adopted. This dataset was chosen due to its high spatio-temporal resolution and given that it is well characterized, it serves as an ideal benchmark case. By processing the simulated PIV images using standard techniques the data also was imparted with noise and uncertainty typical of experimentally determined data. While this case provides high temporal resolution, through the use of the method of snapshots, this is not a requirement of the AR-POD method. The resolution per vector was 0.195 wall units for a Reynolds number of 640, based on the frictional velocity and channel half height. The temporal resolution was adjusted such that out-of-plane particle motion was one-half of the assumed laser plane thickness. While this data set only provided 100 snapshots of the flow, the energy fraction from the POD showed that only 63 modes were required to capture 99% of the fluctuating energy leading to the conclusion that enough snapshots were present to fully resolve the behavior of the field. Furthermore, subsample convergence testing as described below reinforced this conclusion. Additional information on the dataset parameters can be found in Stanislas et al. (Stanislas, Okamoto et al. 2005).

The PIV data was processed in MATLAB with an in-house software that uses a Robust Phase Correlation technique (Eckstein, Charonko et al. 2008; Eckstein and Vlachos 2009b; Eckstein and Vlachos 2009a) combined with an iterative multigrid process (Scarano and Riethmuller 2000; Murray and Seiner 2008). The first pass used a rectangular window of 64x32 pixels (x,y) and grid resolution of 32x16 pixels, while the second pass utilized a 16x16 pixel window with a grid resolution of 8x8 pixels. This processing produced a field of 191x63 vectors over the complete domain. No intermediate or final validation was performed during the PIV processing.

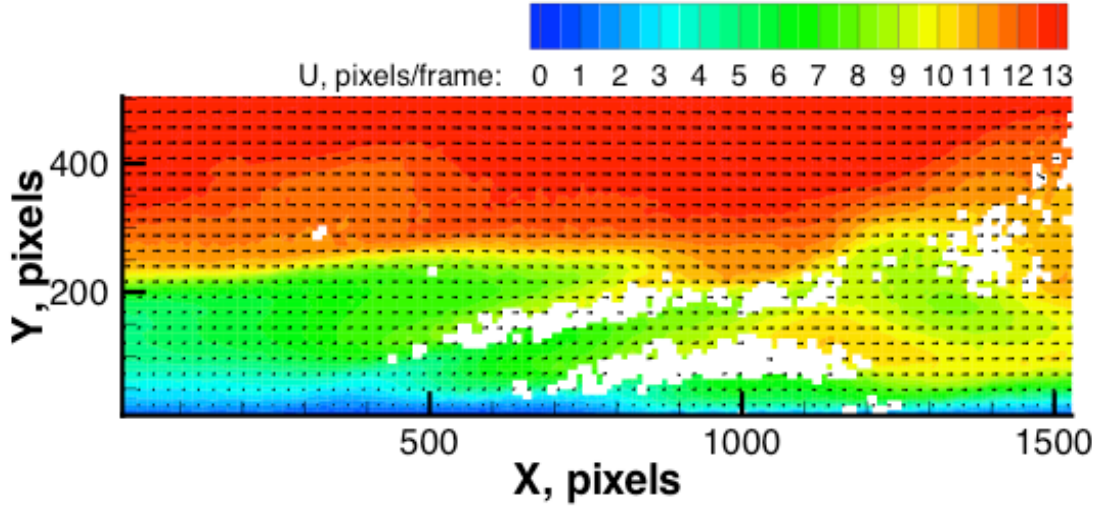


Figure 2.1. Vector field from unvalidated PIV with erroneous vectors removed.

In order to determine the locations of the bad vectors a Universal Outlier Detection (UOD) method was implemented (Westerweel and Scarano 2005). Here, it will be assumed that all bad vectors have been correctly identified and only good measurements remain. The complete dataset had a gappiness percentage of 1.3% with the largest percentage per frame being 6.3% and the smallest being 0.04%. The locations of all bad points were stored into the mask shown in equation 8. The same assumption regarding the accurate detection of bad measurements was made by Everson and Sirovich and Venturi and Karniadakis (Venturi and Karniadakis 2004) for their reconstruction. A single snapshot output from the PIV processing is shown in Figure 2.1.

To insure that the data has statistically converged and that enough snapshots are available, the variance as a function of a subset of points was compared to the total field variance. This method was proposed by Murray and Ukeiley and has been shown to work well with POD reconstruction of highly turbulent data (Murray and Ukeiley 2007; Murray and Seiner 2008). By defining a subsample number of points P , where $P < N$ and N is the total number of snapshots, a subsample variance can be estimated, (Equation 12). A relationship between the subsample variance and the total variance, σ^2 , can be

expressed by equation 13. A data set can be considered converged when the subset variance has reduced below that of the total variance.

$$\epsilon_P^2 = \text{var}_{N_p} = \frac{1}{P} \sum_{i=1}^P ((\overline{U_N} - \overline{U})^2)_i \quad (12)$$

$$\text{var}_{N_T} = \frac{N-1}{N} \sigma^2 \quad (13)$$

It can be seen from Figure 2.2 that the data has reached statistical convergence at 100 snapshots satisfying that the number of snapshots considered herein is sufficient. The measurement point used for this convergence test was randomly selected. Additional locations were investigated but the results showed no dependence on the spatial location.

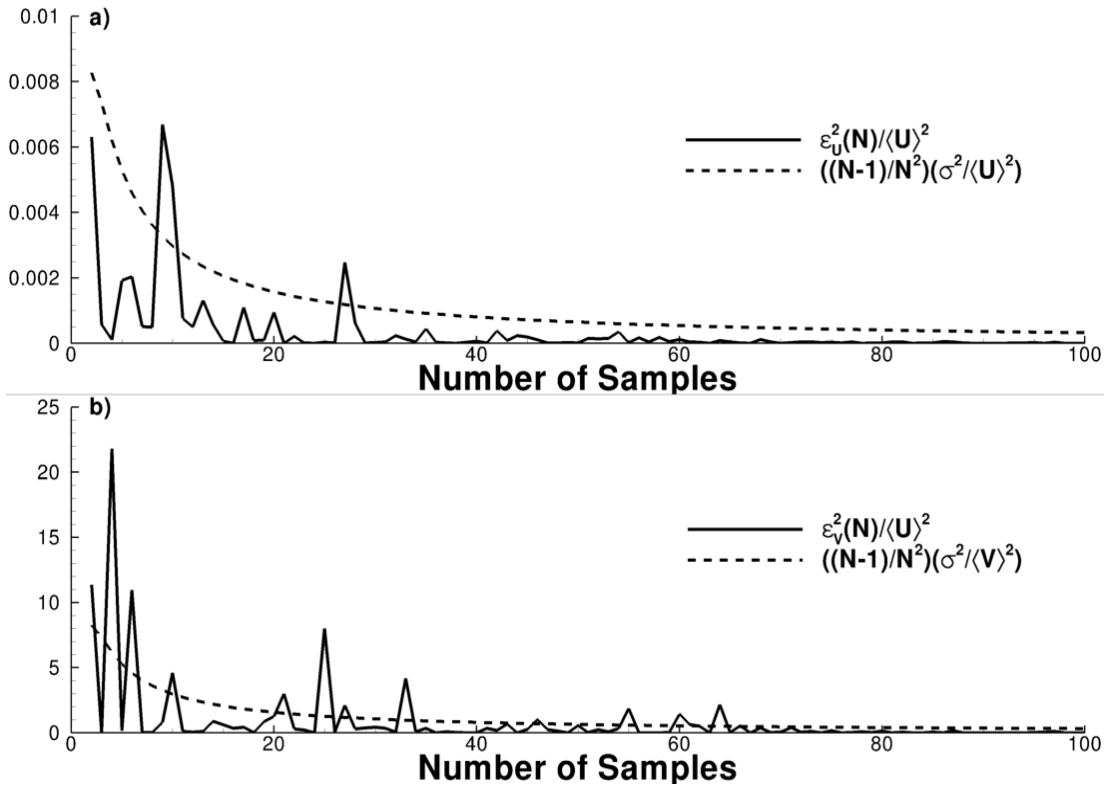


Figure 2.2. Convergence data for both the U and V PIV velocity fields, a and b respectively. The X and Y locations chosen for this test were 1024 and 192 pixels respectively.

2.6. Results and Discussion – Turbulent Boundary Layer

In this section the error analysis results from the AR-POD will be presented. This method will be compared with the aforementioned POD reconstruction methods along with interpolation techniques that are commonly used to repair PIV data.

2.6.1. Adaptive POD Reconstruction

Figure 2.3 shows a single snapshot reconstructed using the Adaptive POD Reconstruction method. From this figure it can be seen that this new method appears to reasonably reconstruct the field. To illustrate the ability of the reconstruction to adapt to local conditions, Figure 2.4 shows the location of the erroneous measurements colored by the final mode number used during the reconstruction for the flow field of Figure 2.3. While many features are seen to reconstruct with lower mode numbers (1-20), other features continue to add information even from the final mode. Because points are allowed to adaptively converge, i.e. not update on every mode's iteration, points that would normally converge to a local minimum are allowed to update later during the reconstruction if a smoother solution is achieved using a different subset of reconstructed modes. This means that while a high final convergence mode may be seen, the individual points may have excluded some of the previous, and possibly erroneous, reconstructions to reach its final values. This idea is again shown in Figure 2.5. While the number of points that updated on the final mode is high, their selectivity during the reconstruction helps to produce the most accurate results. A more in depth error analysis will be presented later in this section.

As mentioned, this work takes advantage of the computational efficiency of the Reduced Gappy POD reconstruction (Gunes, Sirisup et al. 2006; Murray and Seiner 2008). Some studies have stopped the reconstruction prematurely due to this computational cost and thus possibly sacrificed optimal reconstruction (Murray and Ukeiley 2007; Murray and Seiner 2008). If POD reconstruction is to become more commonplace in the PIV community the computational efficiency must be enhanced to make its utilization more tractable. By improving the accuracy of reconstruction using the Reduced Gappy POD,

through this newly proposed Adaptive Reconstruction, implementation of a POD process will become more feasible for the community.

2.6.2. Eigenspectra Comparison

Venturi and Karniadakis stated that optimum reconstruction was achieved when the eigenspectra of the reconstructed field closely matched that of the true solution (Venturi and Karniadakis 2004). For this reason Figure 2.6 shows a comparison of the eigenspectra of the different reconstructions with that of the true solution. For the interpolation methods the POD eigenspectra was calculated after reconstruction using the procedure described in section 3. We observe that the unvalidated PIV data is clearly not in agreement with the true solution. All other reconstruction methods show varying degrees of improvement compared to the true eigenspectra. The eigenspectra of the Kriging and POD methods show strong resemblance to that of the true solution for the first 50 modes. Unfortunately, the comparison of the eigenspectra does not provide a quantitative measure of the reconstruction, since it does not offer any information on the mode shapes. Cases could arise where the eigenspectra shows strong agreement but the spatial information contained in the modes and therefore the reconstruction could deviate significantly. For these reasons, error analysis with respect to the true solution must be performed.

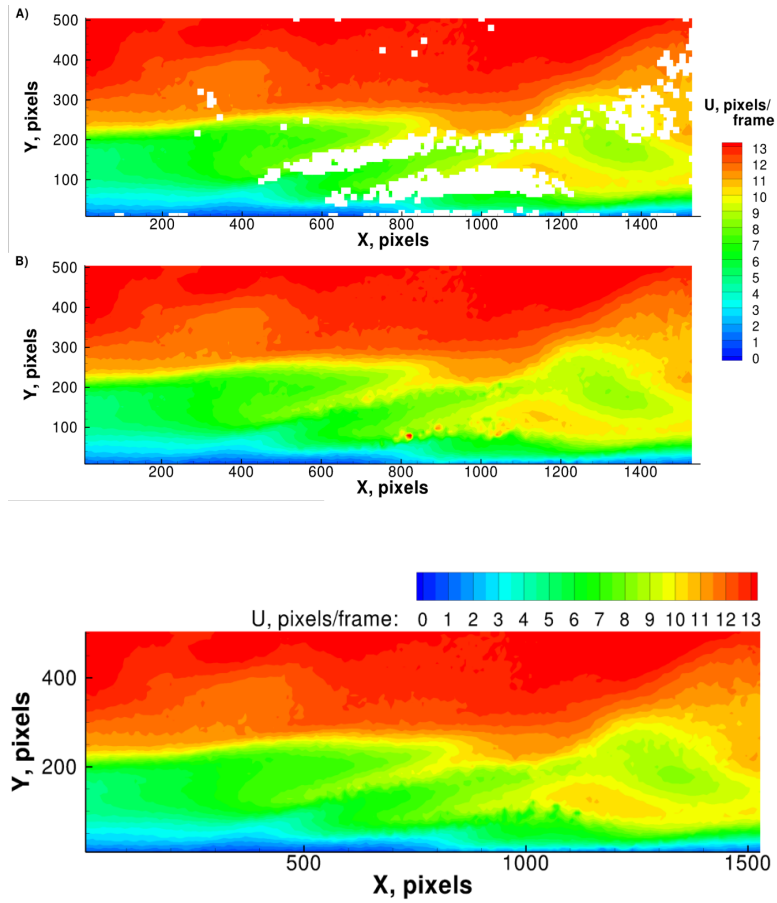


Figure 2.3. Original and reconstructed field using adaptive POD reconstruction, A) and B) respectively. A horseshoe vortex near the wall produced elevated numbers of erroneous vectors in the PIV processing, (frame 27 in 2003 PIV Challenge set B (Stanislas, Okamoto et al. 2005))

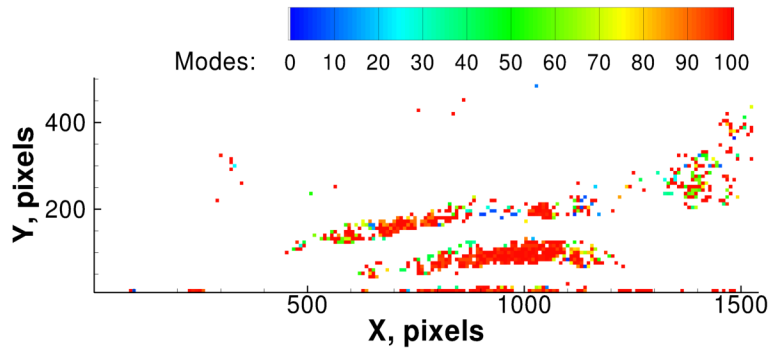


Figure 2.4. Spatial distribution of the final mode used by the adaptive POD reconstruction for frame 27.

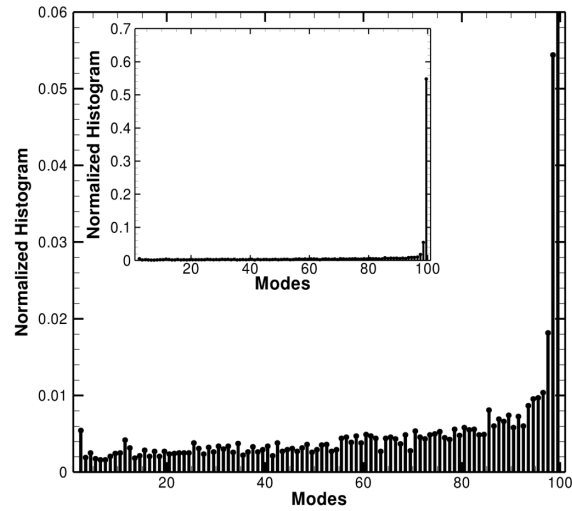


Figure 2.5. Histogram of the final modes used in reconstruction for all of the points. The inset to this figure shows that the maximum mode was used for more than 50% of the gappy locations.

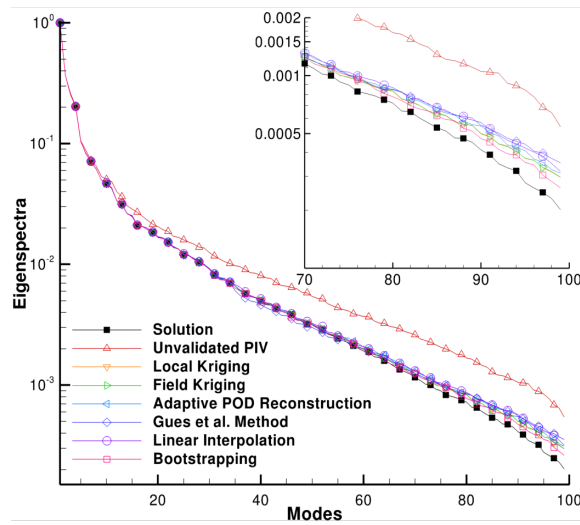


Figure 2.6. Eigenspectra Comparison for all of the different reconstructions. The upper right shows a zoomed in portion of the complete figure demonstrating the Eigenspectra divergence in the high modes.

2.6.3. Error Comparison

With access to a true solution for this dataset, an error analysis can be performed to determine which reconstruction method most effectively reconstructs the true solution. To perform this comparison the U and V error along with the error magnitude were used as shown in equation 14, where U_R is the

reconstructed velocity and U_S is that of the solution. The error magnitude provides a percent error based on the magnitude of the velocity at each point. The average and Root Mean Squared (RMS) errors were also evaluated using the error data from equation 14. The average error was also used to monitor convergence as proposed by Gunes et al (Gunes, Sirisup et al. 2006).

$$\begin{aligned} \text{Error, } \epsilon_u(x, y; t) &= \frac{(U_R - U_S)}{U_S} \\ \epsilon_v(x, y; t) &= \frac{(V_R - V_S)}{V_S} \\ \epsilon_{mag}(x, y; t) &= \left(\frac{(U_R - U_S)^2 + (V_R - V_S)^2}{U_S^2 + V_S^2} \right)^{1/2} \end{aligned} \quad (14)$$

$$\text{Average} = \frac{1}{N} \sum^N \epsilon(x, y; t) \quad (15)$$

$$\text{RMS} = \sqrt{\frac{1}{N} \sum^N (\epsilon^2)} \quad (16)$$

The RMS error, as used by previous works (Venturi and Karniadakis 2004; Gunes, Sirisup et al. 2006), has been shown to be the strongest metric for characterizing the performance of these methods since it is greatly affected by the presence of outliers in the data. Figure 2.7 shows the RMS error associated with the U and V velocity components. Because the results for the interpolation methods do not vary based on the number of modes they are illustrated with horizontal lines. It can be seen that the AR-POD method performs the best for the U velocity. Error for this case drops below that of the local Kriging at a mode number of 32 and remains lower throughout most of the reconstruction, rising slightly at the very end. The other methods, E-S and Gunes, do not drop below that of either of the Kriging interpolations but come closest at mode 58 where they both find their minimum value of 0.50 and 0.51 respectively. The RMS error reduction in U is 13% when comparing the final reconstruction of the adaptive method with the minimum error from the other POD methods. The reconstruction of the V velocity using AR-POD performs well but not as well compared to the Kriging interpolations. Here the error value never falls below that of the Kriging interpolations. The adaptive method does again perform better than the other POD methods, reducing the RMS error by 5% when again comparing the final

reconstruction of the adaptive method to the minimum error from the other methods. It is also important to note that since the AR-POD method is intended to use the maximum number of available modes, errors for both U and V tend to decrease toward a minimum and not rise substantially with the addition of further modes.

The E-S and Gunes et al. also show dramatically increasing error as the maximum number of modes is reached, with an almost 400% increase in error compared to the minimum value. This is due to the fact that as the reconstruction advances, erroneous information that is typically contained in the higher modes, and thus is ignored during the early stages of the reconstruction, is ultimately re-introduced increasing the error. What appears as a change point, where the error goes from being relatively flat to increasing quickly, is a function of primarily the original error percentage but can also be problem specific (Gunes, Sirisup et al. 2006). It is important to note that the newly proposed AR-POD method is not as affected by the end-rise problem. Because the AR-POD method allows individual points to converge independently and does not force unnecessary information to be included, it greatly outperforms current POD reconstruction methodologies as the total number of frames is reached. With the final average error lower than the minimum error of the Gunes et al. method, it can be stated that the AR-POD method provides a more accurate reconstruction for the data shown here.

Figure 2.8 shows the average and RMS of the error magnitude, U and V combined together as shown in equation 14. The error magnitude is the strongest metric for accuracy as it is normalized by the velocity magnitude at each location. For the average error, Figure 2.8A, it can be seen that the error from the AR-POD reconstruction does dip below that of the Kriging interpolations at mode 28 but rises above at mode 74. While this method does not terminate at an average error value below Kriging, its value is comparable to the other POD methodologies, 0.102 for E-S and 0.103 for Gunes et al. and 0.104 for the Adaptive method. For the RMS error, Figure 2.8B, the adaptive method consistently outperforms the Kriging interpolations and the other POD methodologies. While the final RMS error value for the adaptive method is higher than the minimum value from the other POD methods, 0.21 as compared to the

Gunes method's error of 0.14, both methods outperform the field Kriging at 0.25 and the AR-POD method is close to that of local Kriging at 0.20. This in part can be attributed to the fact that at the edges the Kriging is performing an extrapolation which can produce very high errors. For comparative purposes Figure 2.8 C) and D) show the error analysis results from these different reconstructions ignoring points that are within 3 grid units of the boundary and thus removing any cases of extrapolation. It can be seen from this figure that all the reconstruction methods (interpolation and POD) perform better when these edge points are removed with the Kriging becoming the most accurate method overall. It can also be seen that the AR-POD method improves significantly when the edge points are removed. Because this method performs derivative estimation to compute the smoothness, when the edge points are not considered (traditionally difficult for derivative schemes) this method shows great improvement compared to the other POD.

It should be noted that when the Everson – Sirovich method is performed without solving the linear system of equations its results are remarkably similar to that of the reduced iterative procedure of Gunes et al.. Also, it has been shown that when solving the linear system of equations on turbulent experimental data, the non-iterative approach performs better (Murray and Seiner 2008). This suggests that while the iterative procedure performs well with smooth, low noise data (Venturi and Karniadakis 2004; Gunes, Sirisup et al. 2006), it will be compromised when applied to experimental data.

Figure 2.9 shows the average and RMS of the error with solving the linear system of equations proposed by Everson and Sirovich. As mentioned this method is much more computationally intense as the system of equations grows. For the Gunes et al. method the reconstruction was run in MATLAB 2010b on a Dell Precision R5400 Dual Quad Core 2.0 GHz machine for 45 days at which point they had only completed 70 of the 100 total modes. The processing times for Adaptive POD reconstruction with direct replacement and with the iterative replacement were compared and found to be comparable. The method with iterative replacement started some time after the other methods and has only reach 53 modes. By not solving the linear system the complete set (100 snap shots) was solved in 31.75 hours,

20.66 hours, and 32.50 hours for the Everson and Sirovich method, Gunes et al. Method and Adaptive POD reconstruction method respectively. A list of computational times for both reconstruction procedures can be seen in Table 2.1. This table also shows that on average the computational time increases 3500% by solving this additional linear system of equations. In addition, it is shown that the linear system of equations produces a slightly less accurate solution, which has been seen in previous studies (Murray and Seiner 2008). Table 2.2 shows the average and RMS error values for the three POD reconstruction methodologies at 36 modes, which is the minimum using the Gunes convergence method with the POD coefficients, and 70 modes which was the maximum number of modes used when solving the linear system of equations due to computational constraints. These results suggest that the combined computational efficiency and improved accuracy of the Reduced Gappy POD offer a more appropriate method for PIV data.

Table 2.1. Processing times for the different POD reconstruction. Due to computational expense, only the first 70 modes were reconstructed using the linear system while all of the modes were reconstructed using the POD coefficients.

Method	Using POD Coefficients (Full 100 modes)	Using Linear System (First 70 modes)	Percent Increase
Everson and Sirovich	31.75 hours	1078.0 hours	3400%
Gunes et al. Method	20.66 hours	934.2 hours	4520%
Adaptive POD	32.50 hours	1066.8 hours	3300%

The uniqueness of this new adaptive reconstruction method, in comparison to the other POD methods, resides in the fact that individual points in the field are only updated subject to an objective convergence criterion. If adding an additional mode to the reconstruction does not reduce the local value of the smoothness parameter, then the data at that location will not be updated and the value from the previous reconstruction will be utilized. By allowing these spatial points to converge independently, flow features are reconstructed independently rather than requiring high frequency features to be reconstructed with the same information as low frequency features or vice versa. This independence leads to a higher accuracy reconstruction.

Table 2.2. Error values for the different methods at 36 modes which corresponds to the minimum using the Gunes et al. convergence method, and 70 modes which is the maximum number of modes reconstructed using the linear system of equations.

Method	Average ₃₆	RMS ₃₆	Average ₇₀	RMS ₇₀
Using POD Coefficient				
Everson and Sirovich	0.1020	0.1512	0.1725	0.3474
Adaptive POD	0.0765	0.1210	0.0813	0.1457
Gunes et al. Method	0.1032	0.1535	0.1838	0.3822
Using Linear System				
Everson and Sirovich	0.1052	0.1531	0.2196	0.4782
Adaptive POD	0.0785	0.1218	0.0852	0.1488
Gunes et al. Method	0.1059	0.1545	0.1838	0.3515

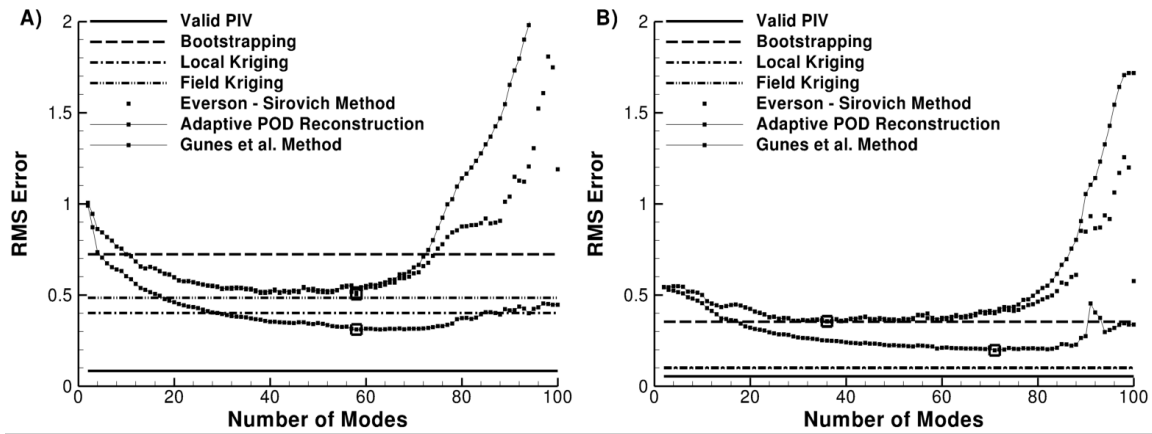


Figure 2.7. RMS error for the U and V velocity components, A) and B) respectively. Due to the high error values in the linear interpolation method it is not shown for clarity. Because the E-S method does not rely on information from the previous mode's convergence it is shown with only symbols. The open symbols show the minimum locations in A) of 58, 64, and 58 and in B) of 36, 100, and 36 for Everson – Sirovich, Adaptive POD and Gunes et al. method respectively.

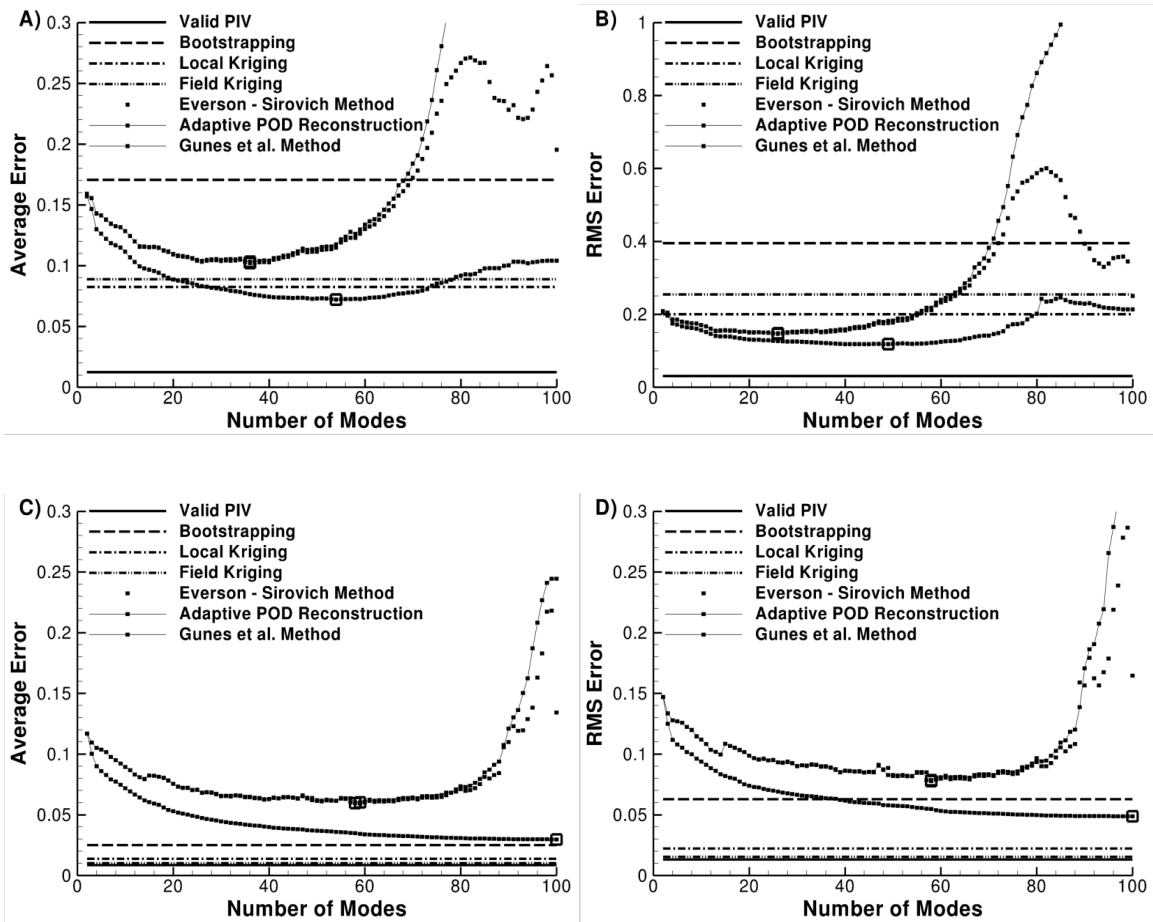
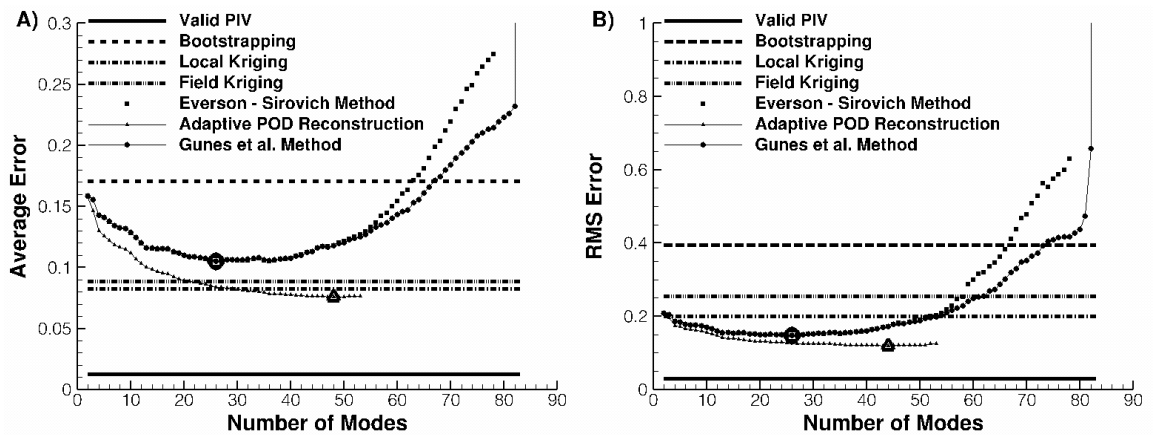


Figure 2.8. Average and RMS error magnitude for all included points, A) and B), and with edge points excluded, C) and D), for the different reconstruction methodologies. The open symbols denote the minimum location in A) of 35, 49, and 38, B) of 26, 42, and 26, C) of 57, 100, and 57, D) of 59, 100, and 59, for the Everson – Sirovich, Adaptive POD, and Gunes et al. method respectively.



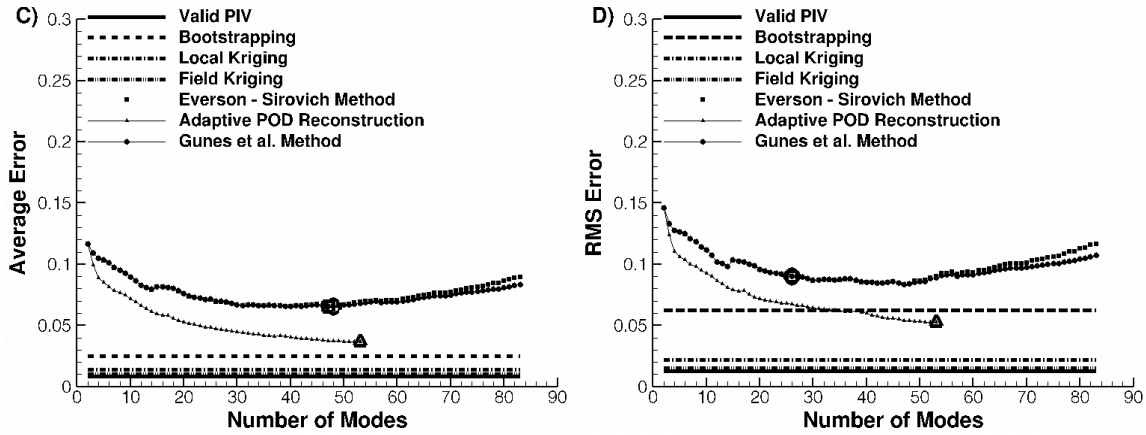


Figure 2.9. Average and RMS error magnitude for all included points, A) and B) and with edge points excluded C) and D), for the different reconstruction methodologies now solving the linear system proposed by Everson and Sirovich. The open symbols denote the minimum location in A) of 26, 48, and 26, in B) of 26, 44, and 26, in C) 47, 53, and 48, and in D) 48, 53, and 48 for the Everson – Sirovich, Adaptive POD, and Gunes et al. method respectively.

In order to investigate the effect of gappiness percentage on reconstruction accuracy an additional test was performed. For this study, the PIV data was compared to the true solution and then a threshold was determined at which data would be removed. This threshold was varied in order to produce 6 gappiness levels of 5%, 10%, 20%, 40%, 60%, and 80%. These new fields were then reconstructed using local Kriging, the Gunes et al. method or the newly proposed Adaptive POD reconstruction. The local Kriging and Gunes et al. method were chosen as they were the strongest competition in terms of reconstruction for the interpolation and POD methods respectively. Due to the increased computation cost associated with higher gappiness levels not all of the reconstructions reach 100 modes. For the Adaptive POD reconstruction the terminal mode was 100, 95, 79, 68, 62, 100 for the 5%, 10%, 20%, 40%, 60%, and 80% gappiness levels respectively. The reason that the 80% case finished quicker is because with less information to work with the POD iterations converge quickly while the other cases with more information take more time to converge to a solution..

It can be seen from Figure 2.10 that both the Gunes et al. method and the Adaptive POD reconstruction showed improved performance as the gappy percentage is reduced, but while the Adaptive

POD method shows consistent performance as the mode number is increased the Gunes et al. method quickly becomes affected by the end rise problem discussed earlier. This problem with the Gunes et al. method at high gappiness percentages was originally reported by the authors (Gunes, Sirisup et al. 2006). While local Kriging has shown to be very effective at low gappiness percentages it can be seen here that it quickly becomes ineffective as the gappiness level is increased. Not shown in this figure is local Kriging for 40% gappiness, which had an RMS error of 3.72. This figure illustrates the robustness of the new Adaptive POD reconstruction method over the currently available techniques.

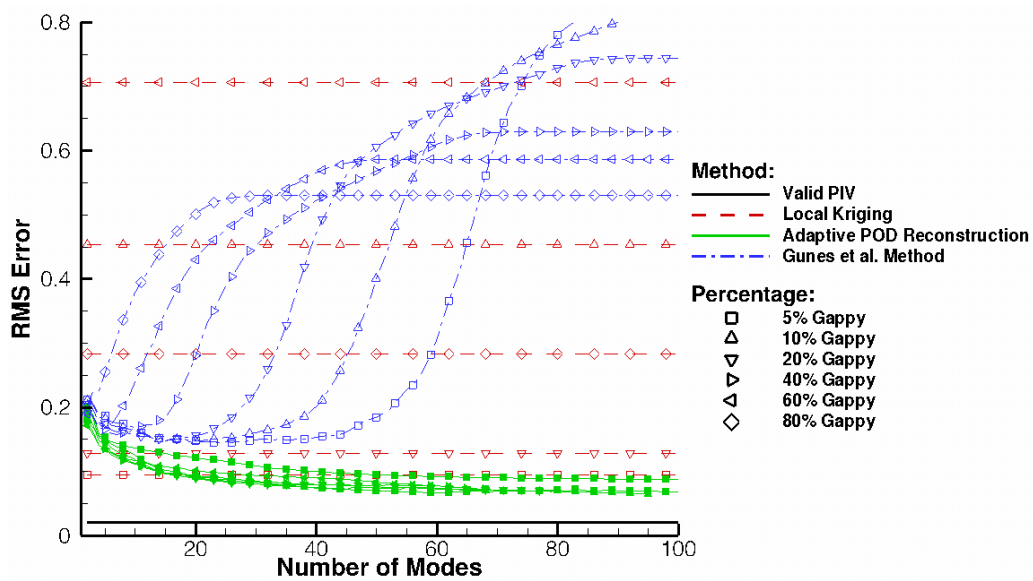


Figure 2.10. Effect of varying gappiness percentages on RMS reconstruction error. The symbol shapes (■, ▲, ▼, ►, ●, ◆) represent gappiness percentages of 5%, 10%, 20%, 40%, 60% and 80% respectively. The closed symbols belong to the Adaptive POD reconstruction while the open symbols belong to the Gunes et al. method. Kriging is shown with a dashed line with only every 4th symbol shown for clarity.

2.7. Velocity Field DATA and PIV Processing – Experimental Data Case

In order to demonstrate the applicability of this reconstruction procedure to experimentally obtained data, a dataset from a turbulent channel flow experiment was tested. The facility used to obtain this data was a vertically-oriented water tunnel as seen in Figure 2.11. This tunnel consisted of three major sections: lower receiving chamber, test section, and settling chamber (not shown). For this experiment,

water was drawn from the settling chamber via a Kohler 0.5 Hp pump (model: 60934) and injected into 4 locations in the top of the lower receiving chamber (5.08x5.08 cms from the corners of the chamber). This injection not only provided the water for the tunnel but also generated large-scale turbulent structures from the injection process. The water was then directed vertically upward into the test section through a contraction that prevented the flow from separating. The top of the test section was open to atmosphere and allowed the water to spill over a dividing wall before being returned to the settling chamber. The square test section, which was concentric about the center of the lower receiving chamber, had a hydraulic diameter of 20.32 cms. The average velocity of the water through the test section was set to 4.3 cm/s, which provided a Reynolds number of 8738.

To capture the velocity information for this experiment a Time Resolved Stereo PIV (TR-SPIV) system was used. Two Photron APX-RS cameras both with Nikon 85 mm Scheimpflug lenses were used to record the particle field illuminated a New Wave Pegasus Nd:YAG laser. The cameras were tilted approximately 30 degrees off perpendicular to the laser plane. These cameras have 1024 pixel by 1024 pixel CMOS sensors which provided a magnification of 84.66 um/pixel. The velocity field was sampled at 250 Hz, which corresponded to a 2.0 pixel displacement between consecutive frames. Because the displacement was so small between consecutive frames a frame step of two was used for the correlations, which allowed for the sampling rate to be maintained at 250 Hz while allowing a 4 pixel displacement between frames. The images, from both cameras, were processed using a two pass multigrid method in conjunction with Robust Phase Correlation (RPC) (Scarano and Riethmuller 1999; Eckstein and Vlachos 2009a; Eckstein and Vlachos 2009b). Validation using the Universal Outlier Detector (UOD) was used both intermediately and on the final pass (Westerweel and Scarano 2005). The Soloff et al. method of stereo reconstruction was used for this data (Soloff, Adrian et al. 1997). This method consisted of a third order polynomial that was used in conjunction with the calibration information to dewarp the vector fields and then properly combine them and obtain the additional velocity information.

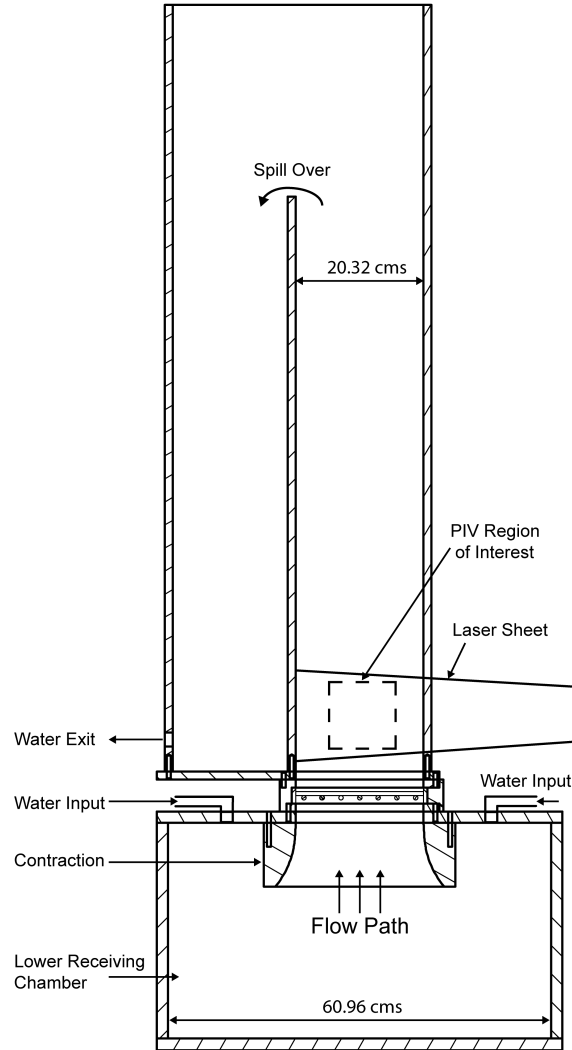


Figure 2.11. Schematic for vertical water tunnel facility showing the lower receiving chamber and test section.

In order to make this field “gappy”, clusters of points were randomly removed from the field. The cluster size ranged from 1 – 5 vectors in both the X and Y direction. The total percentage of vectors removed for this case was 20 percent. An example image of the field before and after data was removed can be seen in Figure 2.12. This data set consisted of 500 snapshots. When looking at the cumulative sum of the eigenspectra, Figure 2.13, it was seen that 95% of the total energy was captured by the first 15 modes and 99% of the energy was capture by 156 modes. This supports the statement that while only 500 snap shots were used it was in fact more than sufficient to completely resolve the fluctuations found in the field.

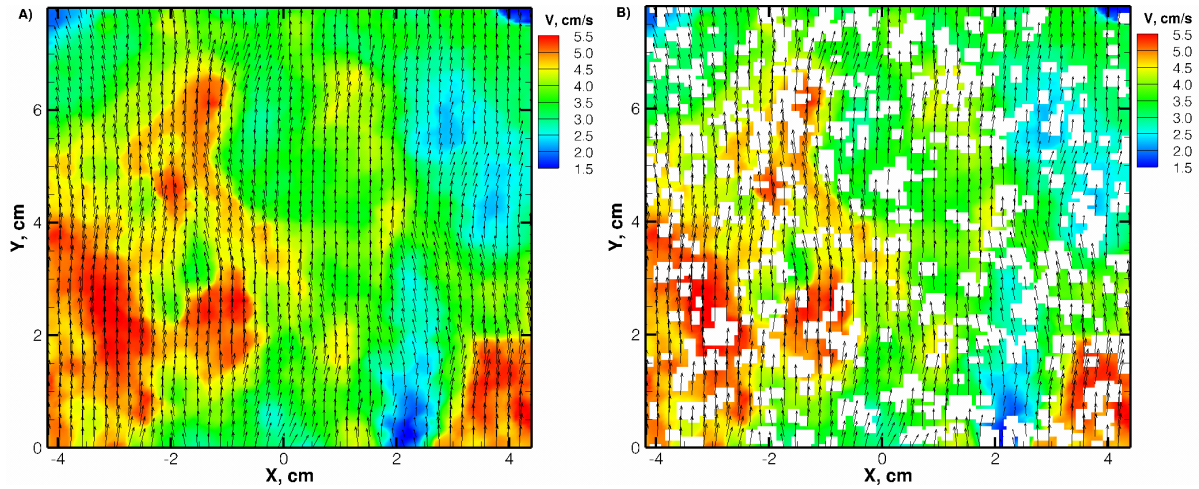


Figure 2.12. Vector field from the original (A) and gappy field (B) from the turbulent channel experiment. The contour is vertical velocity (V).

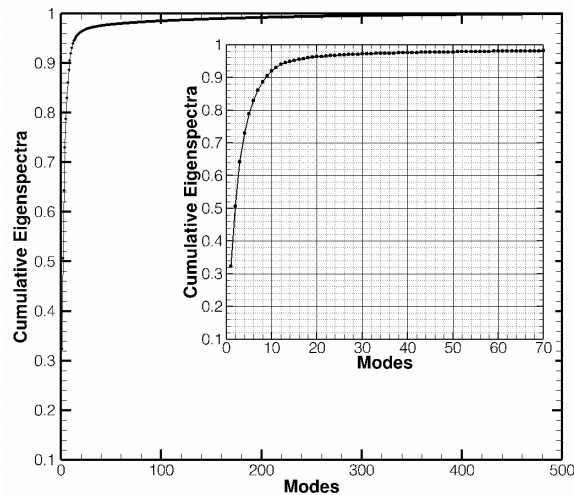


Figure 2.13. Cumulative sum of the eigenspectra for the turbulent channel flow field. The inset shows a zoomed in look at the first 70 modes.

2.8. Results and Discussion – Experimental Case

Figure 2.14 shows a reconstructed snap shot from the AR-POD method. Visually this field strongly resembles the original field, which helps to support the assertion that this method can be applied to experimentally obtained data sets and that it can perform well even with fields containing high gappiness percentages. Because this is an experimental field, obviously no true solution exists for the purpose of

comparison. For the error analysis performed in this section, the original values from the field will be used as the “true” solution similar to Gunes et al.. It should be noted that this gives an obvious advantage to the Gunes et al. method as it is developed in such a way that it tries to find the best solution based on the valid information provided.

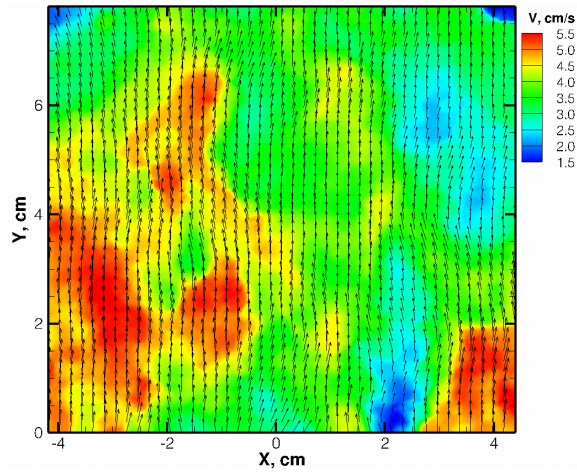


Figure 2.14. Reconstructed field after 70 modes using the adaptive POD reconstruction. Visually no discernable difference can be seen when compared to the original field.

Continuing to use the error analysis procedure presented in section 5, Figure 2.15 shows the average and RMS error for the first 70 modes of the reconstruction. In addition to the AR-POD method the Gunes et al. method as well as local Kriging were performed to provide comparisons. These two methods were chosen as they were the strongest competitors to this new method from the categories of POD- and interpolation-based methods, respectively. It can be seen from this figure that the AR-POD method consistently outperformed the Gunes et al. method both in average and RMS error and after 48 modes the AR-POD outperformed the local Kriging with respect to average error. After 70 modes the AR-POD method performed 25% better than the Gunes et al. method and 5% better when compared to Kriging with respect to the average error. For the RMS error, while the AR-POD does not yet outperform Kriging it did perform 13% better than the Gunes et al. method. While due to computational costs only 70 modes were computed, it can be seen that the AR-POD methods error was still decreasing as more modes were

added, leading to the possibility of an even higher accuracy reconstruction if the method had been allowed to continue.

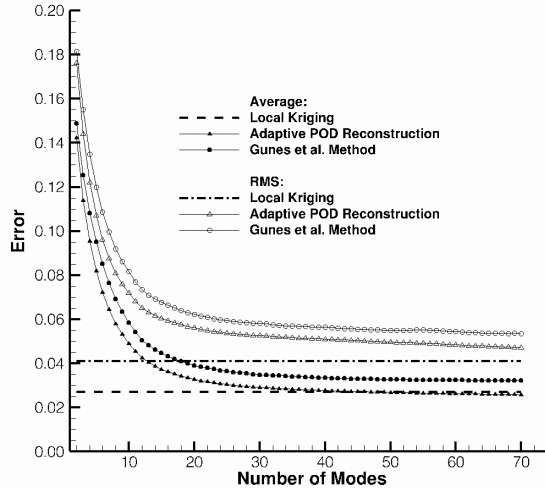


Figure 2.15. Average and RMS error for reconstruction of the turbulent channel flow field. The closed symbols denote average error while the open symbols are RMS.

It should be noted that these results come using the iterative convergence replacement for the AR-POD method. While not shown here, the authors found that when determining smoothness for this case, if the field was evaluated with direct replacement of the current step then points at the centers of the gappy blocks remained at lower and more smooth modes. While direct replacement showed improved results in select cases this iterative replacement appears to be a more universal approach.

2.9. Conclusions

A novel gappy POD methodology for adaptive reconstruction of PIV data was developed and characterized. This method improves upon the current gappy POD methodologies as well as upon different interpolation-based reconstructions for PIV data. Its enhanced performance stems from a) improved accuracy beyond what was previously reported and b) providing a solution to the final mode convergence problem that currently existed with some of the POD reconstruction techniques. By combining POD reconstruction with an adaptive convergence through a field smoothness parameter,

individual spatial points are reconstructed with different numbers of POD modes. This allows for high frequency spatial features to be reconstructed independently of lower frequency features. As a result the RMS error decreased by as much as 13% and 5% for the U and V velocity components respectively, when compare to the next best method (Gunes et al.). Also, because the method allows for measurements to be updated only if and when a new minimum in the field smoothness parameter is reached, points are not trapped into local minimums that can corrupt the data set. Finally, this work showed that the reduced reconstruction methodology proposed by Gunes et al. performs better with experimentally determined PIV data than the linear systems approach by Everson and Sirovich.

2.10. References

- Druault, P. and C. Chaillou (2007). "Use of Proper Orthogonal Decomposition for Reconstructing the 3D in-Cylinder Mean-Flow Field From PIV Data." Comptes Rendus Mecanique **335**(1): 42-47.
- (a) Eckstein, A. and P. P. Vlachos (2009). "Assessment of advanced windowing techniques for digital particle image velocimetry (DPIV)." Measurement Science and Technology **20**(7): 075402-075402.
- (b) Eckstein, A. and P. P. Vlachos (2009). "Digital particle image velocimetry (DPIV) robust phase correlation." Measurement Science & Technology **20**(5): 055401.
- Eckstein, A. C., J. Charonko, et al. (2008). "Phase correlation processing for DPIV measurements." Experiments in Fluids **45**(3): 485-500.
- Everson, R. and L. Sirovich (1995). "Karhunen-Loeve Procedure for Gappy Data." Journal of the Optical Society of America **12**(8): 1657-1664.
- Fore, L. B. (2010). "Reduction of peak-locking errors produced by Gaussian sub-pixel interpolation in cross-correlation digital particle image velocimetry." Measurement Science and Technology **21**(3): 035402-035402.
- Fore, L. B., A. T. Tung, et al. (2005). "Nonlinear Temporal Filtering of Time-Resolved Digital Particle Image Velocimetry Data." Experiments in Fluids **39**: 22-31.
- Gunes, H. and U. Rist (2007). "Spatial resolution enhancement/smoothing of stereo-particle-image-velocimetry data using proper-orthogonal-decomposition-based and Kriging interpolation methods." Physics of Fluids **19**(6): 064101-064101.
- Gunes, H. and U. Rist (2008). "On the use of Kriging for enhanced data reconstruction in a separated transitional flat-plate boundary layer." Physics of Fluids **20**(10): 104109-104109.
- Gunes, H., S. Sirisup, et al. (2006). "Gappy Data: To Krig or not to Krig?" Journal of Computational Physics **212**: 358-382.
- Hart, D. P. (1998). The Elimination of Correlation Errors in PIV Processing. 9th International Symposium on Applications of Laser Techniques to Fluid Mechanics. Lisbon, Portugal.
- Hart, D. P. (2000). "PIV error correction." Experiments in Fluids **29**(1): 13-22.
- Huang, H., D. Dabiri, et al. (1997). "On errors of digital particle image velocimetry." Measurement Science and Technology **8**: 1427-1440.
- Karri, S., J. Charonko, et al. (2009). "Robust wall gradient estimation using radial basis functions and proper orthogonal decomposition (POD) for particle image velocimetry (PIV) measured fields." Measurement Science & Technology **20**(4): 045401.
- Lee, K. and D. N. Mavris (2010). "Unifying Perspective for Gappy Proper Orthogonal Decomposition and Probabilistic Principal Component Analysis." AIAA Journal **48**(6): 1117-1129.
- Lophaven, S., H. Nielsen, et al. (2002). DACE, A Matlab Kriging Toolbox, Version 2.0, Report IMM-REP-2002-12.

- Ma, X., G. E. Karniadakis, et al. (2003). "DPIV - Driven Flow Simulation: A New Computational Paradigm." Proceedings of The Royal Society **459**(2031): 547-565.
- Murray, N. E. and J. M. Seiner (2008). "The effects of gappy POD on higher-order turbulence quantities." AIAA Paper 2008-241.
- Murray, N. E. and L. S. Ukeiley (2007). "An Application of Gappy POD: for subsonic cavity flow PIV data." Experiments in Fluids **42**: 79-91.
- Myers, D. E. (2002). "Interpolation of spatial data: Some theory for Kriging." International Journal of Geographical Information Science **16**(2): 205-207.
- Nogueira, J., A. Lecuona, et al. (1997). "Data Validation, False Vectors Correction and Derived Magnitudes Calculation on PIV Data." Measurement Science and Technology **8**: 1493-1501.
- Oliver, M. A. and R. Webster (1990). "Kriging: A Method of Interpolation for Geographical Information Systems." International Journal of Geographical Information Systems **4**(3): 313-332.
- Powell, M. J. D. (1992). The Theory of Radial basis Functions in 1990. W. Light, Oxford University Press: 105-207.
- Pun, C. S., A. Susanto, et al. (2007). "Mode-ratio bootstrapping method for PIV outlier correction." Measurement Science & Technology **18**(11): 3511-3522.
- Scarano, F. and M. L. Riethmuller (1999). "Iterative multigrid approach in PIV image processing with discrete window offset." Experiments in Fluids **26**(6): 513-523.
- Scarano, F. and M. L. Riethmuller (2000). "Advances in iterative multigrid PIV image processing." Experiments in Fluids **Suppl.**: S51-S60.
- Sirovich, L. (1987). "Turbulence and the Dynamics of Coherent Structures I-III." Quarterly of Applied Mathematics **45**: 567-571,573-590.
- Sirovich, L. (1989). "Chaotic Dynamics of Coherent Structures." Physica D **37**: 126-145.
- Soloff, S. M., R. J. Adrian, et al. (1997). "Distortion compensation for generalized stereoscopic particle image velocimetry." Measurement Science and Technology **8**: 1441-1454.
- Stanislas, M., K. Okamoto, et al. (2005). "Main Results of the Second International PIV Challenge." Experiments in Fluids **39**: 170-191.
- Tan, B.-T., K. Willcox, et al. (2003). "Applications of Proper Orthogonal Decomposition for Inviscid Transonic Aerodynamics." AIAA Paper **4231**.
- Tipping, M. E. and C. M. Bishop (1999). "Probabilistic principal component analysis." Journal of the Royal Statistical Society **61**(3): 611-622.
- Vedula, P. and R. J. Adrian (2005). "Optimal Solenoidal Interpolation of Turbulent Vector Fields: Application to PTV and Super-Resolution PIV." Experiments in Fluids **39**: 213-221.

- Venturi, D. (2006). "On Proper Orthogonal Decomposition of Randomly Perturbed Fields with Applications to Flow Past a Cylinder and Natural Convection Over a Horizontal Plate." Journal of Fluid Mechanics **559**: 215-254.
- Venturi, D. and G. E. Karniadakis (2004). "Gappy Data and Reconstruction Procedures for Flow Past a Cylinder." Journal of Fluid Mechanics **519**: 315-336.
- Westerweel, J. (1994). "Efficient Detection of Spurious Vectors in Particle Image Velocimetry Data." Experiments in Fluids **16**(3-4): 236-247.
- Westerweel, J. and F. Scarano (2005). "Universal outlier detection for PIV data." Experiments in Fluids **39**(6): 1096-1100.
- Zoldi, S. M. and H. S. Greenside (1997). "Karhunen-Loeve Decomposition of Extensive Chaos." Physical Review Letters **78**(9): 1687-1690.

3. Computation of Finite Time Lyapunov Exponents from Time Resolved Particle Image Velocimetry Data

3.1. Abstract

This work presents two new methods for computing Finite Time Lyapunov Exponents (FTLE) from noisy spatio-temporally resolved experimental data generated using Particle Image Velocimetry (PIV). These new approaches are based on the simple insight that the particle images recorded during PIV experiments represent Lagrangian flow tracers whose trajectories lend themselves to the direct computation of FTLE flow maps. We show that using this idea we can improve the reliability and accuracy of FTLE calculation through the use of either sequential Lagrangian particle tracking velocimetry (PTV), where individual particle paths over a fixed period of time are used to determine the flow map, or PTV flow map interpolation, where instantaneous tracking results are used to advect massless tracer particles creating the complete flow map. Comparisons of the traditional numerical integration method for computing FTLE fields with these new methods show that PTV flow map interpolation produces significantly more accurate estimates of the FTLE field for both synthetic data as well as experimental data. This is because the numerical integration estimates particle motion while PTV directly measures particle motion and therefore generates a more accurate flow map. Overall our results suggest that the numerical integration is not always a reliable approach when applied to noisy experimental PIV data. For cases where particle loss between frames is minimal, the sequential Lagrangian tracking can also produce better results but the final field is susceptible to error due to the unstructured nature of the raw flow maps. When comparing the ability to match the true separatrix of a flow, PTV flow map interpolation is shown to be a far superior method. The separatrix from PTV flow map interpolations has an 80% overlap with the true solution as compared to approximately 25% for the sequential Lagrangian tracking and only 1% for the numerical integration method. PTV flow map interpolation shows a significant advantage when the particle seeding is low, which is particularly relevant for applications to environmental or biological flows where adding seed particles is not always practical and investigation of Lagrangian flow structures must rely on naturally occurring flow tracers.

3.2. Introduction

Finite-Time Lyapunov Exponents (FTLE) can provide information on the mixing and transport mechanisms in a flow (Brunton and Rowley 2010; Shadden 2011) and they are applicable in both turbulent and laminar flows (Haller 2001). FTLEs are a measure of the exponential rate of divergence or convergence of the Lagrangian particle trajectories over a finite time. The calculation of FTLEs has been used previously in both experimentally (Shadden, Katija et al. 2007; Peng and Dabiri 2009) and computationally generated (Haller 2001; Wilson, Peng et al. 2009) flow fields.

The ridges, or high magnitude locations in FTLE fields are referred to here as Lagrangian coherent structures (LCS). Ridges can be defined precisely by appealing to differential geometric quantities (Shadden, Lekien et al. 2005). An alternative definition of LCS (Haller 2011) defines LCS more restrictively as hyperbolic material surfaces with extreme finite time normal repulsion or attraction. This eliminates spurious LCS such as those due to shear or stretching. Thus it is more correct to consider ridges of FTLE as candidate LCS, and while they provide insight to the Lagrangian skeleton of the flow, further criteria must be satisfied to classify a candidate LCS as a hyperbolic LCS. Nevertheless, FTLE ridge features can be used to determine the underlying transport structure in complex flow fields (Holmes, Lumley et al. 1996; Lekien and Ross 2010; Senatore and Ross 2011) revealing mixing barriers that inhibit transport, or when there is a high density of rapidly moving LCS, regions of increased mixing (Shadden, Lekien et al. 2005; Tallapragada and Ross 2008; Peng and Dabiri 2009).

While the calculation of LCS from FTLE fields has been used to better understand fluid dynamics behavior both numerically (Haller and Yuan 2000; Lekien and Ross 2010; Tallapragada and Ross 2013) and experimentally (Shadden, Dabiri et al. 2006; Shinneeb, Balachandar et al. 2006; Mathur, Haller et al. 2007; Charonko, Kumar et al. 2013), their application has been limited. Part of the limitation is due to the high computational cost in calculating the FTLE fields. Currently, in order to calculate these fields artificial flow tracers are numerically advected in time to determine the flow map for a flow field (Haller 2002). Determining this flow map using conventional methods is computationally costly (Brunton and Rowley 2010) and can yield incorrect values near boundaries (Ruiz, Boree et al. 2010). Additional

methods have also been developed for decreasing the computation cost for determining and tracking the motion of LCSs for a given flow field (Lipinski and Mohseni 2010).

The current work aims to efficiently and accurately calculate FTLE fields from experimentally measured particle image data of the type used for particle image velocimetry (PIV) or particle tracking velocimetry (PTV). Both are techniques for non-invasively measuring a fluid flow experimentally where flow tracers are added to a flow to probe the fluid's motion (Adrian 1991; Raffel, Willert et al. 1998; Adrian 2005). When properly matched with the experimental flow conditions, these particles are assumed to act as perfect flow tracers (Raffel, Willert et al. 1998), with zero response delay to the flow fluctuations i.e., similar to the numerical particles that are artificially added to the flow during the numerical calculation of the flow maps.

Previous work has shown that the computational cost can be decreased when investigating successive FTLE fields from a single data set by reducing the number of redundant particle integrations (Brunton and Rowley 2010) by numerically integrating particle trajectories over small time intervals to create short snapshots of the flow map. By using compositions of these flow map snapshots, FTLE fields over different initial and final integration times can be computed quickly and efficiently (Brunton and Rowley 2010). This procedure allows for different time intervals to be linked together providing a flow map at varying time intervals with reduced computational cost.

While this approach reduces the computational cost, it is still expensive and moreover it does not take advantage of the flow map information contained in experimental flow fields derived from particle images, i.e., the Lagrangian motion of the particle flow tracers. When PIV or PTV images are acquired they inherently contain information about the flow map over a short-time snapshot, i.e., the discrete particle motion from one frame to the next. This simple insight, suggests that if properly extracted and compiled, these measured particle trajectories can be used to more accurately and directly measure the FTLE/LCS field from experimental PIV data.

This work presents a new method for FTLE calculation by simply measuring the flow map directly from the flow tracer particles present in the field. Compared to the conventional numerical integration method, this new method offers an alternative that is better suited for use with particle image data because it exploits information already inherent in the recorded images to deliver increased accuracy and robustness. By measuring the motion of each of these particles from one time instant to the next, through the use of PTV, a direct measure the flow map can be produced. This new procedure, illustrated in Figure 3.1, eliminates the need for costly numerical integration. In addition, using PTV also has the additional benefit of better resolving near wall flows (Kahler, Scharnowski et al. 2012) which can increase the accuracy of the FTLE/LCS near boundaries.

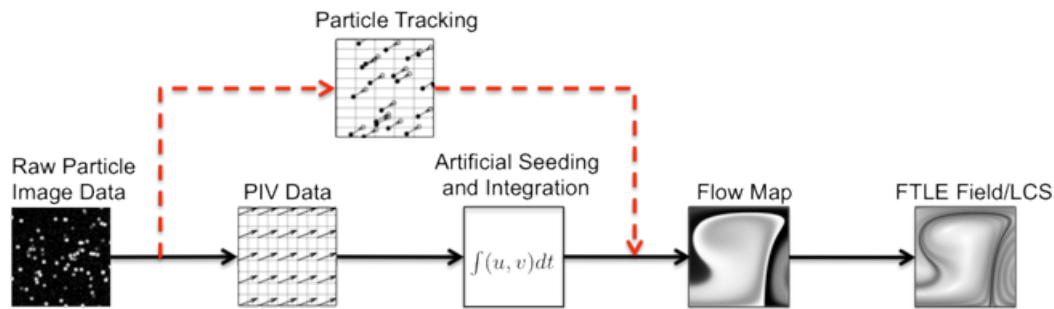


Figure 3.1. Flow chart showing the common procedure for computation of the FTLEs from experimental data and our novel procedure denoted with the red dashed line.

Two different forms of particle tracking can be utilized in order to determine the required flow maps for a given field. The first form is to use sequential Lagrangian particle tracking where individual particles are followed over a series of consecutive frames throughout the entire time of interest. The second method is to use the particle tracking between two adjacent frames and then combine these successive flow maps via interpolation (Brunton and Rowley 2010). The advantage of sequential Lagrangian particle tracking is that the particle tracks are direct measures of the flow map as they provide the exact path of a given particle for a specific location. The disadvantage to this method is that

experimentally it can be challenging to follow a particle over an extended period of time. Particles can be “lost” due to improper matching in the tracking algorithm or, in the case of planar PIV/PTV, they can be lost due to out-of-plane motion. Using tracking information only between two frames has the advantage over sequential Lagrangian tracking in that it can provide a higher density of successfully tracked particles. When limited to only two frames the tracking algorithm will not be as heavily influenced by losses and when properly compiled should provide a very good estimate of the true flow map.

The following provides a detailed analysis of using both Lagrangian particle tracking and instantaneous particle tracking for flow map determination of FTLE fields from experimental data. First a synthetic data set was created to test the methods as well as perform error analysis. This was followed by a demonstration of the methods on an experimental data set of a vortex ring.

3.3. Flow Map Determination

3.3.1. Flow Map Computation using Particle Tracking Methods

This work uses a multi-component particle tracking algorithm that has been developed for single and multiphase flows (Cardwell, Vlachos et al. 2010). The process works by calculating unique particle identifiers such as particle size, shape, and maximum intensity and uses this information to parametrically track the particles. By changing the relative weighting of these factors, along with the inter-particle distance of the possible matched particles, the algorithm can be tuned to work in highly turbulent flows with particles that may not follow the flow. Even non-flow tracers can lead to informative FTLE analysis (Tallapragada and Ross 2008; Peng and Dabiri 2009). When the particles follow the flow path, the algorithm can also use information produced from PIV to more efficiently predict particle motion and pair the particles. Using this method has shown great improvements in both the probability to match particles and in the accuracy of those matches (Cardwell, Vlachos et al. 2010). However, there are several other efficient PTV methods that can also be used to produce accurate PTV velocity field estimations (Ohmi and Li 2000; Mikheev and Zubtsov 2008; Ohmi and Panday 2009).

3.3.1.1. *Flow Map Compilation from Instantaneous Tracking*

Because two-frame tracking results are direct measures of an incremental flow maps over the inter-frame time, i.e., the particle motion between frames, it is possible to achieve more accurate measurements of the total flow map by combining these results together. This method was first proposed for numerical results by Brunton and Rowley (2010). They proposed that the complete flow map could be calculated from a compilation of small time step flow maps as in,

$$\Phi_{t_0}^{t_0+T} = \mathcal{I}\Phi_{t_0+(k-1)\Delta t}^{t_0+T} \circ \dots \circ \mathcal{I}\Phi_{t_0+\Delta t}^{t_0+2\Delta t} \circ \Phi_{t_0}^{t_0+\Delta t} \quad (3.1)$$

where $\Phi_{t_0}^{t_0+T}$ is the flow map calculated from time t_0 to time $t_0 + T$, etc., Δt is the time-step between successive frames, and $T = k\Delta t$. Because these flow maps are computed on a discrete grid, an interpolation, \mathcal{I} , is needed to compile the flow maps. Evaluating small time step flow maps consecutively allows for the total flow map to be computed. As the tracking results are obtained on an unstructured grid they must be interpolated onto the points coincident with the compiled flow map at a given time step. To this end, a thin plate smoothing spline, which provides a high accuracy interpolation while reducing the effects of noise in the tracking results, was used (Karri, Charonko et al. 2009). For a given location in the flow map, the 50 closest tracks centered about the given location were used in the interpolation. This number was chosen in an effort to balance the competing effects of having sufficient information to produce a proper interpolation and not over smoothing the data due to the inclusion of distant points in the interpolation. While the results presented here use a rectilinear flow map, this procedure is still valid if the initial flow map grid was on an unstructured mesh (Lekien and Ross 2010). A flow chart illustrating the traditional procedure along with the newly proposed method for calculating FTLE fields is shown in Figure 3.1.

3.3.1.2. *FTLE Computation from Sequential Lagrangian Tracking*

Lagrangian particle tracking results were compiled from the instantaneous PTV results by linking particle locations from the final position in time step t to initial particle positions in time $t + \Delta t$. Only

complete tracks over the entire time of interest, excluding any lost or gained particles, were used for computation of the FTLE field. Particles can be “lost”, incomplete matching, due to a number of factors including, but not limited to, out of plane motion and incorrect pairing with the previous step of the tracking procedure. This process produces a flow map that is regularly sampled in time, but irregularly sampled in space. In order to perform the FTLE computation the flow maps were first interpolated onto a rectilinear grid. Again a thin-plate spline using the 50 closest particles was used to perform the interpolation. After interpolation the FTLE was computed using the method described in the FLTE section below.

3.3.2. Numerical Particle Trajectory Method

To perform the numerical integration the software package “*Newman*” was used (Du Toit 2010). Newman determines the flow map by numerically integrating a grid of massless tracer particles evenly spaced through the field. To perform this integration a Runge-Kutta 4-5 with an adaptive time step algorithm with tunable absolute and relative initial tolerances was used. For the synthetic data results, the absolute and relative tolerances were set to 10^{-12} and 10^{-14} respectively with an initial time step set to 10^{-7} . For the experimental vortex ring data the absolute and relative tolerances were set to 10^{-10} and 10^{-9} respectively with an initial time step of 10^{-3} . After this numerical integration the FTLE is computed using the method described below.

3.4. FTLE Computation

Computation of FTLEs begins first by computing the right Cauchy-Green deformation tensor, C_{jk} , which is given by,

$$C = \left(\nabla \Phi_{t_0}^{t_0+T} \right)^* \cdot \nabla \Phi_{t_0}^{t_0+T} \quad (3.2)$$

where * denotes transpose, and $\Phi_{t_0}^{t_0+T}$ is the flow map generated by either particle integration or particle tracking. Next, the largest eigenvalue, λ_{\max} , from the deformation tensor is identified and used to yield the forward FTLE field σ at each point in the flow field at time t_0 , as in,

$$\sigma_{t_0}^{t_0+T} = \frac{1}{|T|} \ln\left(\sqrt{\lambda_{\max}(C)}\right) \quad (3.3)$$

3.5. Synthetic Data

In order to test this method on a field with a known solution the double gyre flow field was selected (Solomon and Gollub 1988; Solomon and Gollub 1988). This flow field is a standard test case in the FTLE/LCS literature (Shadden, Lekien et al. 2005; Brunton and Rowley 2010; Lekien and Ross 2010; Tallapragada and Ross 2013) as well as in the fluids community as it is a close approximation to the flow field found in 2D Rayleigh-Benard convection (Solomon and Gollub 1988; Solomon and Gollub 1988). This field can be most easily thought of as a pair of counter rotating vortices confined on all sides as shown in Figure 3.2. The time dependence of this flow is controlled by the asymmetric expansion and contraction of the vortices inside the domain. The flow field is described by the stream-function

$$\psi(t) = A \sin(\pi f(t)) \sin(\pi y) \quad (3.4)$$

where,

$$f(t) = a(t)x^2 + b(t)x \quad (3.5)$$

$$a(t) = \epsilon \sin(\omega t) \quad (3.6)$$

$$b(t) = 1 - 2\epsilon \sin(\omega t) \quad (3.7)$$

This formulation is valid over the domain of x from 0 to 2 and y from 0 to 1. The velocity field is given by

$$u = -\pi A \sin(\pi f) \cos(\pi y) \quad (3.8)$$

$$v = \pi A \cos(\pi f) \sin(\pi y) \frac{df}{dx} \quad (3.9)$$

where A is the scaling parameter for the magnitude of the velocity and ϵ determines how far the vortices grow and shrink. The original formulation of this comes from (Solomon and Gollub 1988) while this specific derivation was performed by (Shadden, Lekien et al. 2005). It is important to note that this solution does not satisfy the Navier-Stokes equations but rather is an approximation of a time-varying flow field with fixed boundaries. If $\epsilon = 0$ then the flow becomes time independent. When $\epsilon \neq 0$, then ϵ provides a measure of how much the separation line between the gyres moves in the x direction over a period of $2\pi/\omega$. For the work herein, ϵ was set to 0.25, ω was set to $\pi/5$ and A was set to 0.1. For results pertaining to this data the spatial domain is normalized using the characteristic length of the domain $x, y = 1, L$.

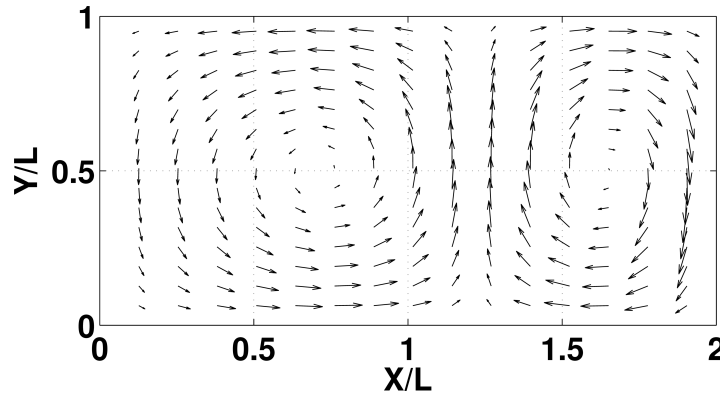


Figure 3.2. Vector field snap-shot of the double gyre flow field.

3.5.1. Artificial Image Generation

To generate images simulating an experimental environment, the benchmark velocities must be integrated at finite locations so that these locations can be used to simulate particles as would typically be seen in PIV/PTV experiments. To perform this integration, 30,000 random tracers were seeded

throughout the domain were integrated using MATLABs ode45 solver which is a Runge-Kutta based numerical differential equation solver that is 4th order accurate with a 5th order check. The equations were integrated using a time step that would allow for 500 evenly spaced realizations over one complete period of the flow, $2\pi/\omega$. Because the particle locations are were randomly distributed in space care needed to taken when performing gradient calculations, to this end the authors used radial basis functions to provide high accuracy estimation of these gradients (Karri, Charonko et al. 2009).

From this larger set of particles, randomly sampled subsets were extracted to generate images with specified seeding densities. Each seeding density was simulated 10 times (with a different subset of particles) in an effort to produce statistically significant results. The seeding densities chosen for the simulations were 500, 1000, 2500, 5000, 7500, 10,000 and 20,000 particles per image. The image size was 1024 by 512 pixels, which produced seeding concentrations of 0.001 to 0.038 particles per pixel for the 500 and 20,000 particle cases respectively. For comparison, in a typical PIV experiment there are approximately 10 particles in a 32 by 32 pixel window corresponding to a seeding density of 0.01 particles per pixel (Raffel, Willert et al. 1998; Adrian and Westerweel 2011).

The image generation was performed using the Gaussian approximation for light scatter from a particle illuminated from a thin sheet of laser light (Brady, Raben et al. 2009). The laser light distribution was also assumed to be Gaussian with the highest intensities at the center of the light sheet. As in an actual experiment, the particles were assumed to be non-uniform in size, with diameters assumed to continuously vary from 2 to 15 pixels.

3.6. PIV and PTV Procedure

The PIV processing was performed using an in-house developed code¹ employing the robust phase correlation technique (Eckstein and Vlachos 2009; Eckstein and Vlachos 2009) in conjunction with the

¹ PRANA software is freely distributed as open source <http://sourceforge.net/projects/qi-tools/>

multi-grid discrete window offset method (Scarano and Riethmuller 1999) and image deformation (Scarano 2002). The initial window size was determined using the $\frac{1}{4}$ rule, which suggests that the window size should be 4 times larger than the maximum particle displacement within. The second effective window resolution was 16 by 16 pixels with a 4 by 4 grid resolution creating 75% overlap between interrogation windows. Two iterations were performed at each window size of a total of 4 passes. To improve the deformation procedure outlier in the intermediate results were removed using the Universal Outlier Detection (UOD) (Westerweel and Scarano 2005) and then smooth while for the final pass only the UOD was applied.

In order to increase the accuracy and robustness of the PTV results, PIV information was used to predict the most likely location of particles in future frames. A weighting of 75% was given to the PIV estimation while 25% was based on the previous tracking information as this code can use previous tracks to better estimate a particle's future position. A two-pass median validation was also used to remove erroneous tracks (Duncan, Dabiri et al. 2010). After these tracks were removed, the new estimate on the next particle position was determined by a weighted average of its surrounding neighbors. Once these new estimates were established the tracking algorithm was re-run to find more accurate matches. Lagrangian particle tracks were acquired by linking the instantaneous particles tracked in successive frames by using the termination locations from the first frame as the starting location of particles in the second frame.

3.7. Experimental Data

In order to test this method on experimental flow fields, data from a laminar vortex ring in a semi-infinite domain was chosen (Stewart, Niebel et al. 2012). This data provided a good test-bed for the present work as previous studies have predicted the geometry of the FTLE/LCS from vortex rings (Shadden, Dabiri et al. 2006; Olcay, Pottebaum et al. 2010). The experimental setup consisted of a piston-cylinder arrangement with the fluid being ejected into a semi-infinite domain. The stroke-to-

diameter ratio (L/D) for the piston-cylinder was 1.2, which produced a Reynolds number of approximately 1,800, based on the circulation and kinematic viscosity.

To measure the fluid motion, neutrally buoyant hollow glass spheres with average diameters of 85 microns were added to the fluid. These particles were illuminated by a Nd:YAG dual head laser (New Wave Pegasus) firing at a constant rate of 500 Hz. The images were captured using an IDT XS-3 CMOS camera with a resolution of 1280 by 1024 pixels and a magnification of 63 microns per pixel providing a resolution of 2.9 diameters in the vertical direction and 6.1 diameter along the length. The spot diameter of the particles in the images was between 2 and 4 pixels. For more information on the experimental setup see the work of (Stewart, Niebel et al. 2012).

The PTV data was computed by using the multi-parametric particle tracking method (Cardwell, Vlachos et al. 2010). Particles were identified using a dynamic thresholding method with a lower pixel intensity limit of 50 (these were 8 bit images with a maximum intensity value of 255). After identification, the particles were sized using a least squares Gaussian method (Brady, Raben et al. 2009) with the diameter assigned at 4 standard deviations. Hybrid PIV-PTV tracking was used to increase the efficiency of the PTV algorithm. The multi-parametric tracking algorithm used a combination of particle size, intensity and estimated position to determine the optimal particle match. Position estimation was performed using both previous track information as well as PIV results. The PIV was processed using the same in-house code utilizing Robust Phase Correlation (RPC) (Eckstein and Vlachos 2009; Eckstein and Vlachos 2009) as the synthetic images.(Eckstein and Vlachos 2009; Eckstein and Vlachos 2009). Due to the high shear rate produced by the vortex, window deformation was also performed (Scarano 2002). An initial PIV window size of 32 by 32 pixels was selected. This window size was held constant for three iterations to allow the window deformation to converge (Scarano 2002). A final window size of 16 by 16 pixels was used and again allowed to converge over three iterations resulting in a total of six passes. Because the deformation method can be very sensitive to outliers in the intermediate results, outliers were identified using the UOD method and smoothed while only outlier detection was applied to the final

output field (Westerweel and Scarano 2005). Once the data was fully processed the PIV results were filtered using Proper Orthogonal Decomposition (POD) (Sirovich 1987) preserving 95% of the fluctuating energy. This step helped to reduce any noise that may have been present in the data.

3.8. Results and Discussion

3.8.1. Synthetic Data

Figure 3.3 shows the benchmark FTLE field computed at $t_0 = 0$ over one full period, $T = 2\pi/\omega$, for the double gyre. We consider this FTLE field the benchmark against which our methods should be compared. The dominant feature of this field is the ridge located in the center extending to the upper left. This ridge is the primary separatrix and will serve as a criterion to determine the effectiveness of the different methods to accurately resolve the FTLE field.

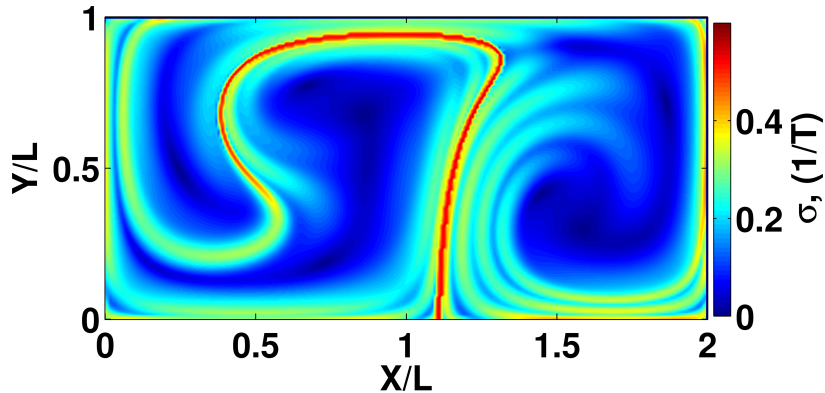


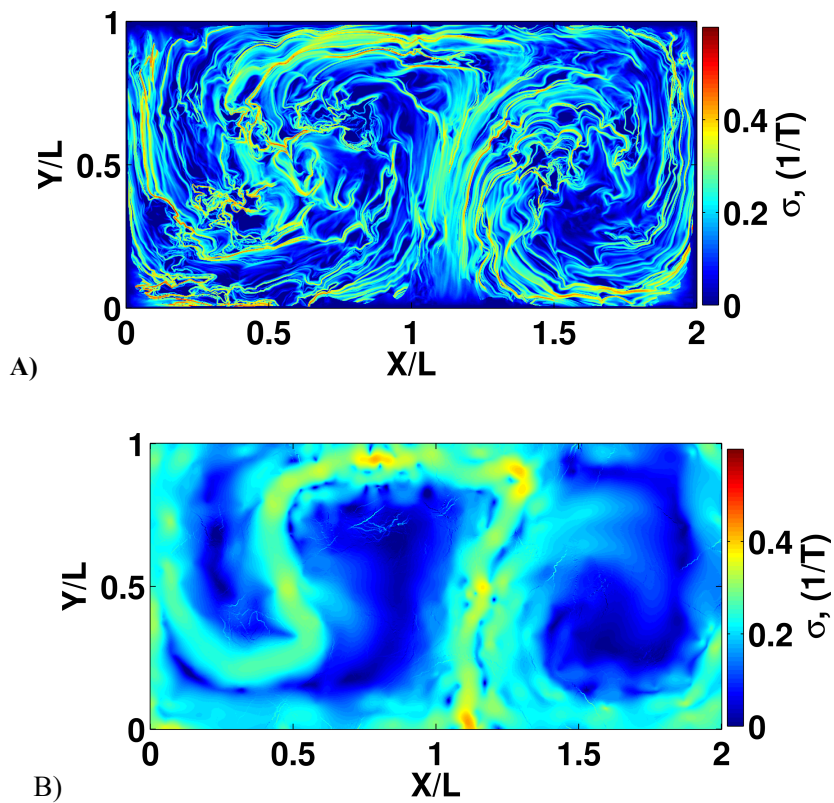
Figure 3.3. Resulting FTLE field from using the benchmark flow field. This field will be used as the basis of comparison for the synthetic data analysis.

For brevity only the 500, 5000 and 20000 particle cases will be shown in the following example figures, although all cases are included in the analysis. Figure 3.4 provides a qualitative comparison between three FTLE fields calculated using different methods from a set of 500 particles. Figure 3.4A was generated using numerical integration; Figure 3.4B using sequential Lagrangian tracking, and Figure 3.4C using PTV flow map interpolation. For the numerical integration massless tracer particles were

placed at every pixel, which produced a grid 8 times finer than the PIV field. For the PTV flow map interpolation the massless particles were placed at every fourth pixel which when using the 50 closest tracks produced an average window size of 95, 29 and 19 pixels for the 500, 5000, and 20000 particles cases respectively. These average windows correspond to relative lengths of 19%, 5.7% and 3.7% when normalized by the characteristic length, L , for the double gyre flow field. For this seeding density the PIV results contain a large amount of noise due to the small number of particles in each interrogation region and as a result, the numerical integration also contains a large amount of error. While increasing the window size would improve the PIV results the reduction in resolution would still yield compromised results (Olcay, Pottebaum et al. 2010). Finite Time Lyapunov Exponent fields can handle high error in the velocity field over a limited duration (Haller 2002), but long duration errors can strongly distort the field (Olcay, Pottebaum et al. 2010). For the sequential Lagrangian tracking, there are a small number of sequential Lagrangian tracks due to the low seeding density. As a result, the FTLE field appears to be under-resolved leading to a diffused and difficult to discern ridge. Unlike the numerical integration at this seeding density, the sequential Lagrangian tracking resolves the separatrix that is present in the benchmark solution, although the ridge appears to have a reduced peak value and is broader than in the benchmark. For the PTV flow map interpolation, even with this low seeding density the method returns a field that is sufficiently similar to that of the solution. Some discrepancies can be seen which again are most likely due to the limited number of tracks used during the flow map interpolation. This field is not only able to capture the main separatrix but also some of the smaller ridges seen in the FTLE field.

Figure 3.5 shows results from the case with a seeding density of 5000 particles where Figures 5A, 5B, and 5C correspond to the numerical integration, sequential Lagrangian tracking, and PTV flow map interpolation methods respectively. With an increased number of particles the numerical integration does an improved job at resolving the field. The method however, does struggle to capture the attachment of the separatrix to the lower wall. This inability stems from the poor numerical integration of velocities near walls. Because the measured velocity from PIV is, in a sense, an average of all the particle velocities

in the interrogation region, it is difficult to properly measure the velocity near a wall or near a location with zero velocity (Kahler, Scharnowski et al. 2012). For the sequential Lagrangian tracking, the field also shows improved estimation of the benchmark solution. Again, error in the flow map due to the discrete locations of the tracks appears as spurious ridges in the FTLE field. For the PTV flow map interpolation, the error in the tail of the separatrix appears to be gone and the noise that was seen in the previous case appears to be diminished.



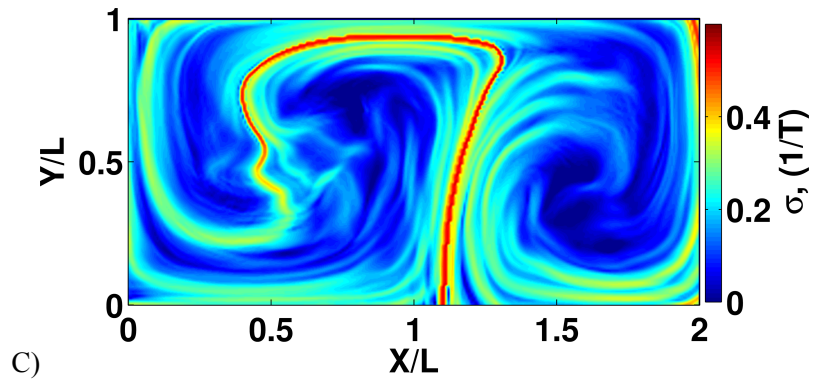
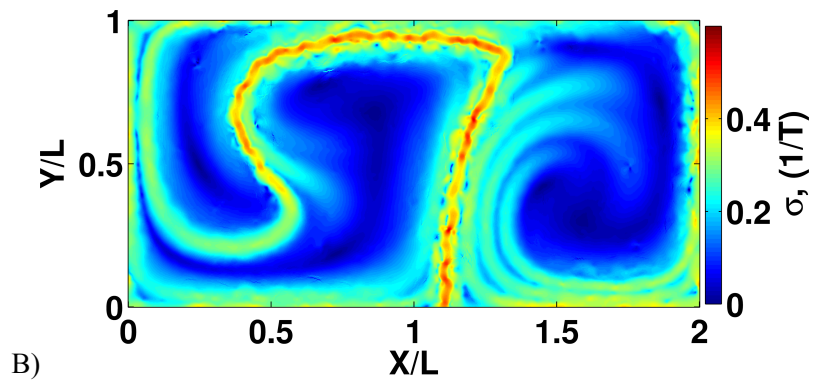
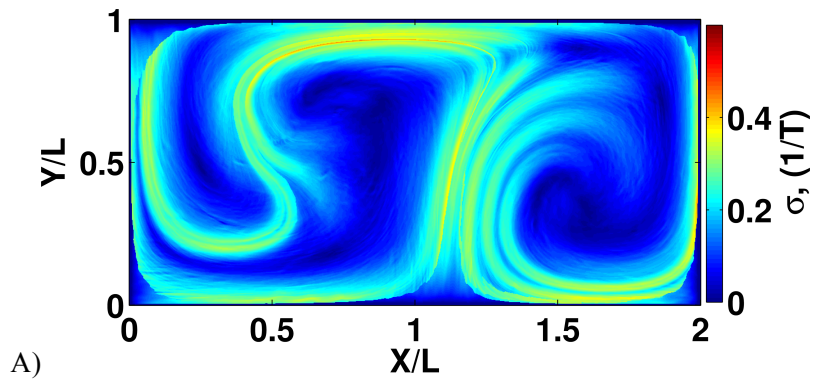


Figure 3.4. FTLE results for the 500 particles case where A), B) and C) represent numerical integration of the PIV velocity fields, sequential Lagrangian tracking, and the PTV flow map interpolation method respectively.



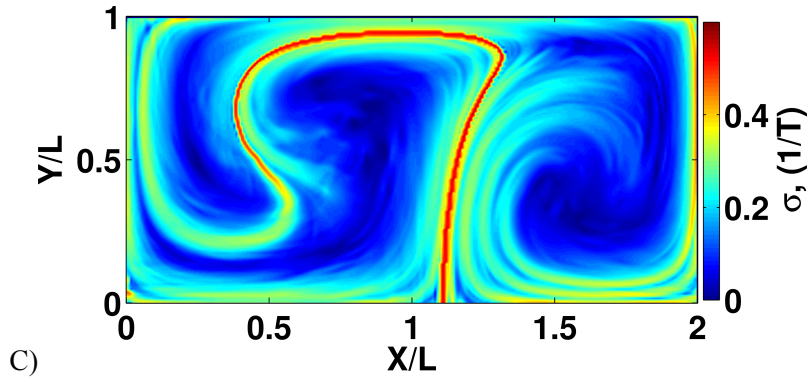
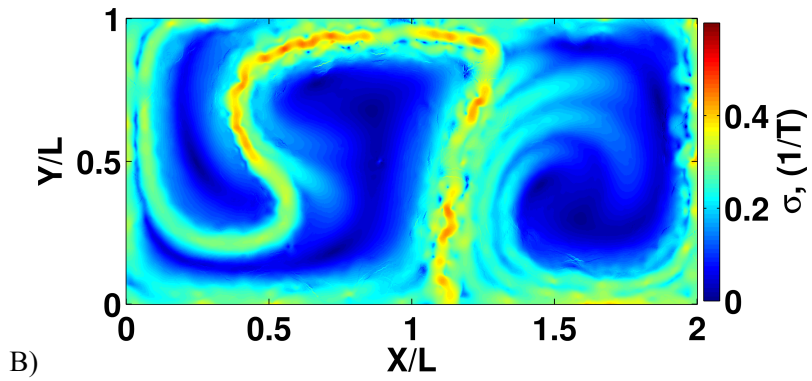
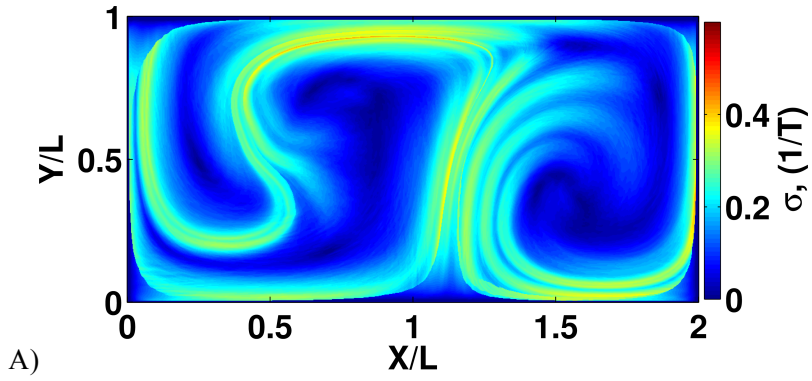


Figure 3.5. FTLE results for the 5000 particles case where A), B) and C) represent numerical integration of the PIV velocity fields, sequential Lagrangian tracking, and the PTV flow map interpolation method respectively.



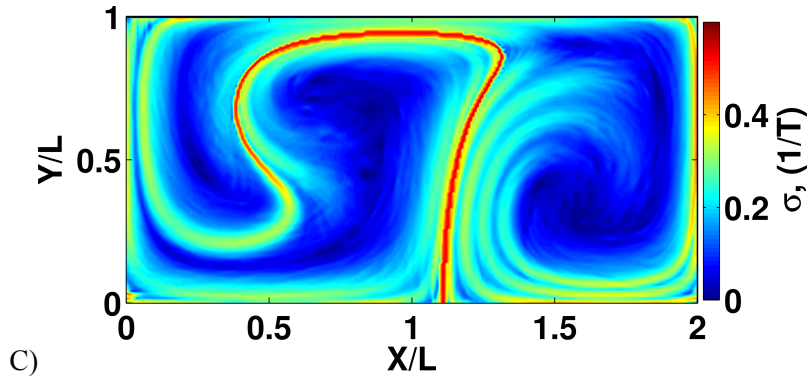


Figure 3.6. FTLE results for the 20000 particles case where A), B) and C) represent numerical integration of the PIV velocity fields, sequential Lagrangian tracking, and the PTV flow map interpolation method respectively.

Finally Figure 3.6 shows the results for the seeding density case of 20000 particles where again Figures 6A, 6B, and 6C correspond to the numerical integration, sequential Lagrangian tracking, and PTV flow map interpolation methods respectively. This case is noteworthy as it is most similar to the seeding density that would be found in an ideally seeded PIV/PTV fluid experiment. Again, for the numerical integration it can be seen that the secondary structures appear to be well resolved (the multiple finger-like structures in the right side of the image) while the main separatrix is still not fully captured. This shows that even with highly seeded data, numerical integration of PIV results may poorly capture features due to near wall dynamics. For the sequential Lagrangian tracking case, again the separatrix appears to be captured, but the noise is still significantly affecting the resolution of the FTLE features. However, the PTV flow map interpolation result shows good agreement with the solution. The separatrix appears to be well resolved with little noise present in the field. However it is worth noting that in Figure 3.5C and Figure 3.6C thin hair-like structures, which are spurious random ridges in the FTLE field, appear, which are not present in the benchmark solution.

For a quantitative analysis of these results, the normalized average error and normalized Root-Mean-Squared (RMS) error was calculated using the following,

$$\text{Normalized Average Error} = \frac{1}{N} \sum_{i=1}^N \left| \frac{\sigma(i)_{\text{Measured}} - \sigma(i)_{\text{Solution}}}{\sigma(i)_{\text{Solution}}} \right| \quad (3.10)$$

$$\text{Normalized RMS Error} = \sqrt{\frac{1}{N} \sum_{i=1}^N \left(\frac{\sigma(i)_{\text{Measured}} - \sigma(i)_{\text{Solution}}}{\sigma(i)_{\text{Solution}}} \right)^2} \quad (3.11)$$

where σ is calculated from t_0 to t_0+T for all of the cases using the solution σ as a benchmark for comparison and i are the different pixel locations for which the FTLE is calculated. These values were computed for each of the 10 cases at each seeding density. Figure 3.7 shows the average of all of these cases for each seeding density with the uncertainty bars showing the one standard deviation value computed from the 10 cases. For the average error, Figure 3.7A, it can be seen that the error decreases as the seeding density is increased. The numerical integration consistently contains higher error than the other methods reaching a minimum value of 0.136 for the 20000 particles case. Sequential Lagrangian tracking reaches a minimum average error of 0.0733 at the 10000 particles case. There is an increase in the error for the sequential Lagrangian tracking in the 20000 particles case to a value of 0.1085. This increase is due to the fact that as the seeding density increases, and the inter-particle distance decreases, there is an increased likelihood that particle mismatch could occur which would introduce error into the flow map and therefore the FTLE field. For the PTV flow map interpolation, the error continues to decrease as the seeding density is increased reaching a minimum at the 20000 particles case of 0.0579, which is the lowest value compared to any of the other cases. The variance between the cases at a given seeding density also diminishes as the seeding density increases. For the 5000 particles cases and above, the variance is less than 2.5% of the error on average.

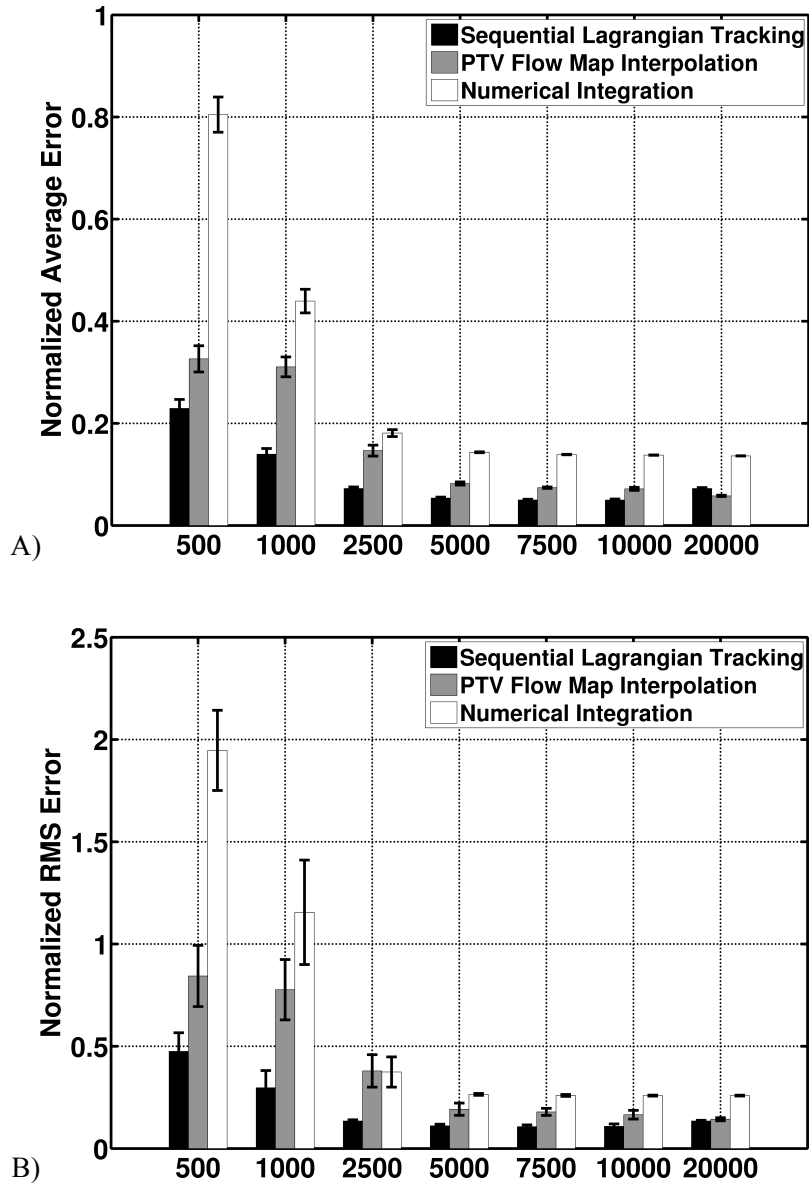


Figure 3.7. Normalized average (A) and Root-Mean-Squared (RMS) (B) error for all three of the methods tested.

For the normalized RMS error, as shown in Figure 3.7B, the error in the FTLE field for the different cases again decreases and levels off as the particle number reaches the 5000 particle case. Again for the highest seeding density the PTV flow map interpolation has the smallest RMS error of 0.1432. The numerical integration consistently has the highest RMS error with very large values at the lower seeding densities. The sequential Lagrangian tracking does well throughout the seeding densities until the 20000

particle cases where the error again rises as seen in the normalized average error. It can be understood from these results that the PTV flow map interpolation proves, under these imaging conditions, to be a superior method when compared to numerical integration and comparable to sequential Lagrangian tracking.

The FTLE difference calculations shown above may lead one to infer that the sequential Lagrangian tracking is almost always delivering the best results. However that would be misleading since Figure 3.4- Figure 3.6 clearly show that it fails to properly resolve the FTLE structure and is only producing comparable results in a spatially averaged sense, where one point spatial FTLE point is weighted equally with the next. Therefore, in addition to investigating the total FTLE field errors, we also investigated the ability of the given methods to properly determine the separatrix seen in the benchmark solution. To this end the amount of overlap between the benchmark separatrix and the calculation method was computed. This analysis is similar to that completed by Olcay, Pottebaum et al. (2010) with their analysis of the sensitivity of LCS identification on the flow field resolution. Figure 3.8 shows the benchmark separatrix (solid grey line) along with the separatrix from the three methods (colored lines) for the seeding density of 500 particles. For this study the separatrix was defined as the region above a threshold value of 0.40, or about 75% of the maximum value, which contained all of the primary ridge information. Here the PTV flow map interpolation clearly shows the best agreement with the benchmark solution. While the sequential Lagrangian tracking produces FTLE values close to that of the benchmark and thus performs well in a statistical sense when we calculate overall errors, here it can be seen that the separatrix is not well resolved and little overlap occurs.

Figure 3.9 shows the overlap for the seeding density of 5000 particles. Again, because of the poor near wall interpolation and velocity resolution, the separatrix is not clearly defined for the numerical integration. For the sequential Lagrangian tracking the separatrix appears noisy and not well resolved. The PTV flow map interpolation method still shows strong overlap with the benchmark solution throughout the length of the separatrix. For the final 20000 particle case, Figure 3.10, the results have a

similar appearance. The increased noise in the sequential Lagrangian tracking can be seen in the noisy separatrix values while the PTV flow map interpolation maintains a good correlation with the benchmark.

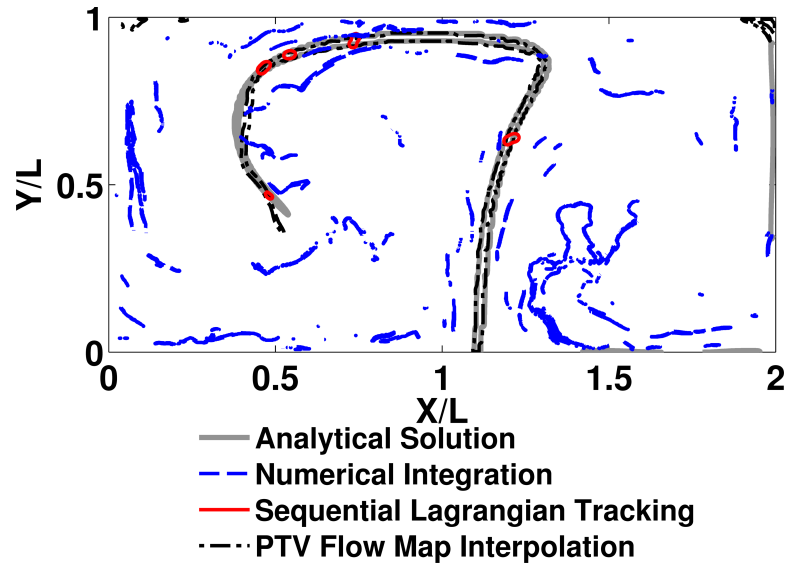


Figure 3.8. Separatrix analysis for the case of 500 particles. The solid grey line represents the separatrix from the benchmark solution.

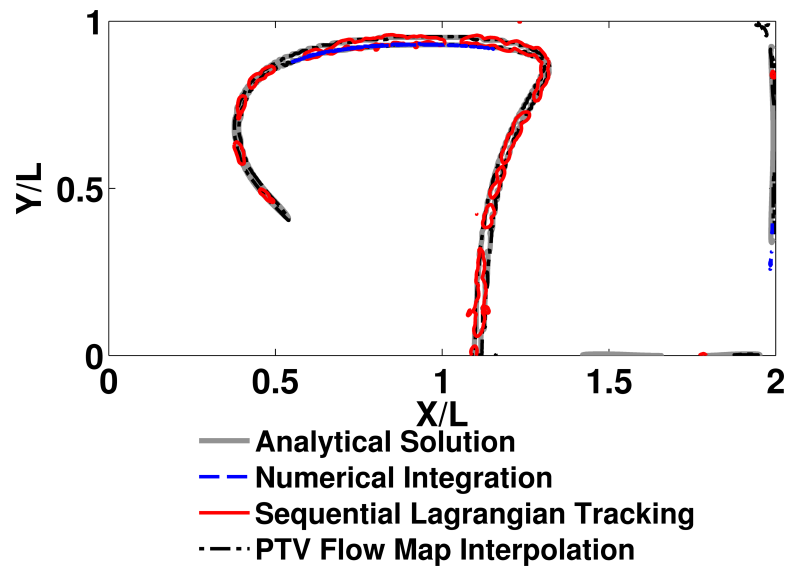


Figure 3.9. Separatrix analysis for the case of 5000 particles. The solid grey line represents the separatrix from the benchmark solution.

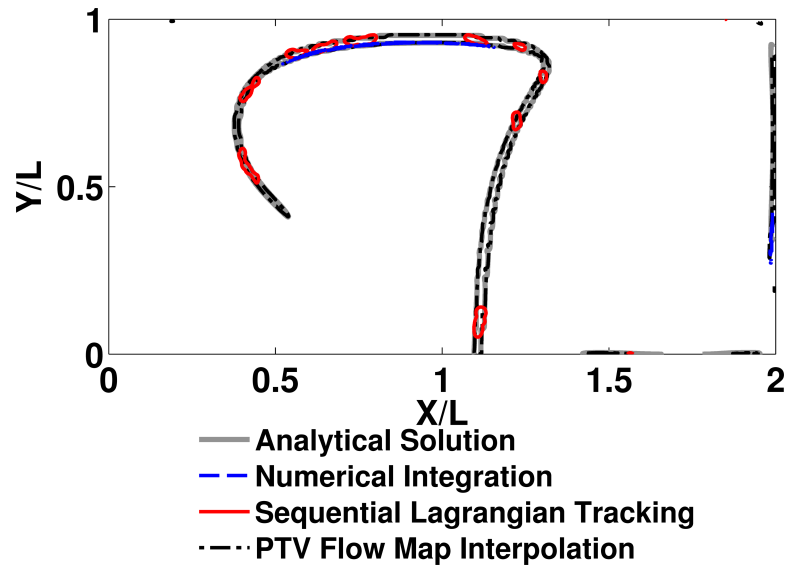


Figure 3.10. Separatrix analysis for the case of 20000 particles. The solid line represents the separatrix from the benchmark solution.

Figure 3.11 shows the overlap percentages for all of the cases and methods. Overlap was calculated by determining the number of FTLE pixel values above the given threshold that occupied the same position as those in the benchmark solution. It can be seen from this figure that the PTV flow map interpolation consistently does a better job at resolving the separatrix than the other methods. The numerical integration is not able to capture the separatrix due to the sharp near wall flow gradient and near wall integration. The sequential Lagrangian tracking performs better than numerical integration but underperforms when compared to the PTV flow map interpolation method. Also, the increased error that is present in the sequential Lagrangian tracking when increasing the seeding density from 10000 to 20000, leads to decreased overlap for the highest seeding density case.

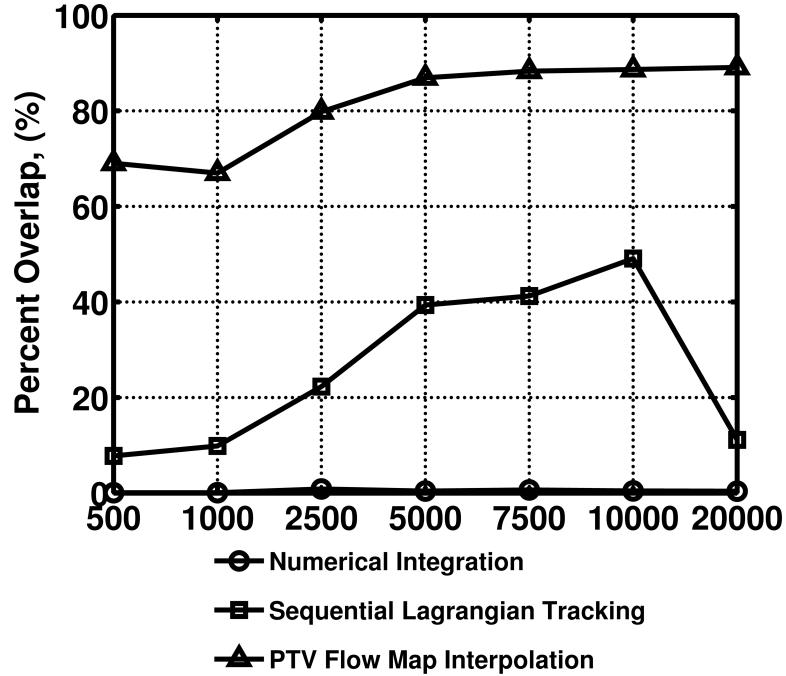


Figure 3.11. Percent overlap between the measure and true separatrix for the different methods.

Another method for measuring the performance of these methods is to use the Hausdorff distance (Dubuisson and Jain 1994). Hausdorff distances have been used in the imaging community for pattern recognition (Zhao, Shi et al. 2005). The Hausdorff distance computes the minimum distance between all of the points in two different sets and then returns the largest of these minimum distances as given by

$$d_H(X, Y) = \max \left\{ \sup_{x \in X} \inf_{y \in Y} d(x, y), \sup_{y \in Y} \inf_{x \in X} d(x, y) \right\} \quad (3.12)$$

where *sup* is the supremum and *inf* is the infimum. This metric helps to describe quality of a match between the two sets; the closer to zero, the better. For the purpose of this study each set will be composed of the largest continuous section of the FTLE above the threshold used in the previous overlap analysis and will be compared to the benchmark solution location above the same threshold. The use of only the largest continuous section is appropriate since, without *a priori* knowledge, this would be chosen as the dominant feature of the field. The results are normalized using the characteristic length, *L*. The result of this comparison is shown in Figure 3.12. It can be seen from this figure that the PTV flow map

interpolation significantly outperforms the other two methods. While qualitatively it could be seen that the PTV flow map interpolation was producing a strong match with the solution, the Hausdorff distance allows for a more quantitative comparison. Again it can be seen from this figure that the sequential Lagrangian tracking improves as the seeding density is increased but then digresses as the seeding density is increased to 20,000. The PTV flow map interpolation shows continuous improvement as the seeding density increases, reaching its smallest value of 0.0082 at a seeding density of 20,000.

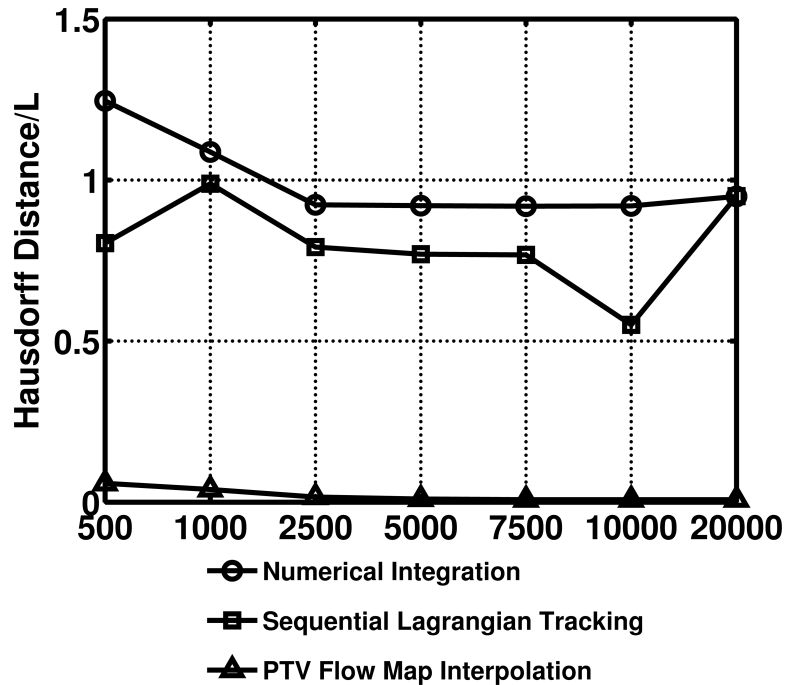


Figure 3.12. Hausdorff distance for all three methods compared with the solution.

3.8.2. Experimental Data

Figure 3.13 shows the velocity field along with the non-dimensional vorticity for the laminar vortex ring experimental case. As typically seen with a vortex ring, the field has maximum vorticity in the two counter rotating cores of the vortex ring cross-section. The seeding density was measured from the particles used during the matching of the particle tracking; it was 0.0172 particles per pixel, which is similar to the 0.0191 particles per pixels seen in the 10000 particles case for the synthetic data. Some noise in the velocity field can be seen in the wavy pattern present in the vorticity magnitude inside the

vortex ring. Noise in the velocity field can become amplified when derivatives are calculated (Etebari and Vlachos 2005), thus the vorticity field may show noise that is not immediately apparent in the velocity field.

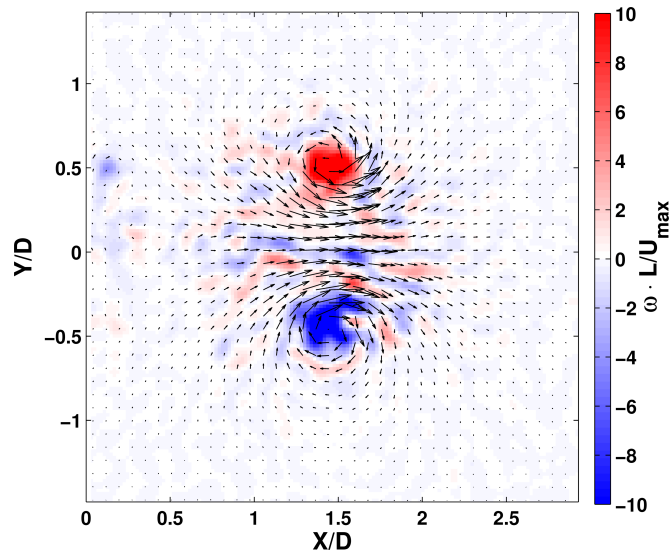
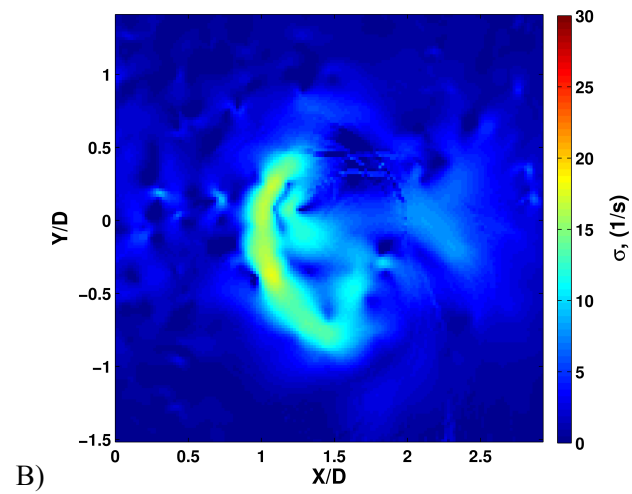
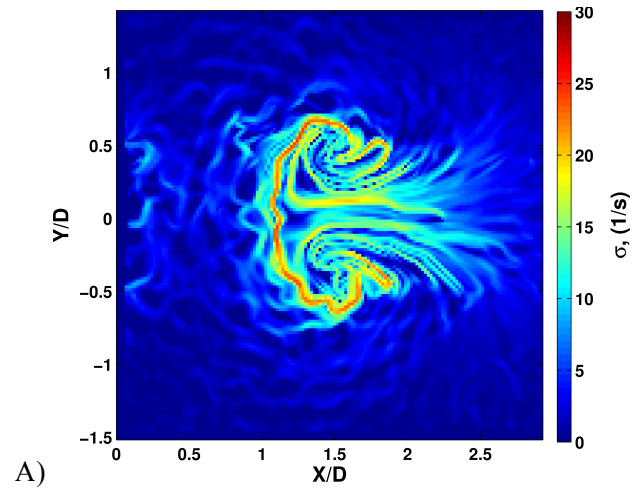


Figure 3.13. Velocity field with the corresponding vorticity field magnitude calculated from PIV data for the experimental laminar vortex ring.

Calculating the forward time FTLE fields for all three methods yields the results shown in Figure 3.14. These results show the FTLE field calculated using 75 frames. The numerical integration produces a strong separatrix around the vortex core along with smaller noisier features in the far field. The shape of the separatrix is to be expected as it represents the boundary between fluid parcels that entrained into the vortex and those that are simply swept around the vortex. The sequential Lagrangian tracking, Figure 3.14B, fails to capture the separatrix around the vortex ring. In experimental data particles can be lost during the particle tracking process for a number of reasons, with the most notable being the out-of-plane motion. This loss of particles reduces the number of sequential tracks that can be used to calculate the FTLE and therefore produces a field with poor resolution of the separatrix. Figure 3.14C shows the results from the PTV flow map interpolation. This field also shows a strong separatrix, similar to the numerical integration, but with a smoother shape and less noise in the far field. In comparison, this

method produces an FTLE field around the vortex ring that most strongly resembles the fields that are seen in the literature (Shadden, Dabiri et al. 2006; Olcay, Pottebaum et al. 2010).



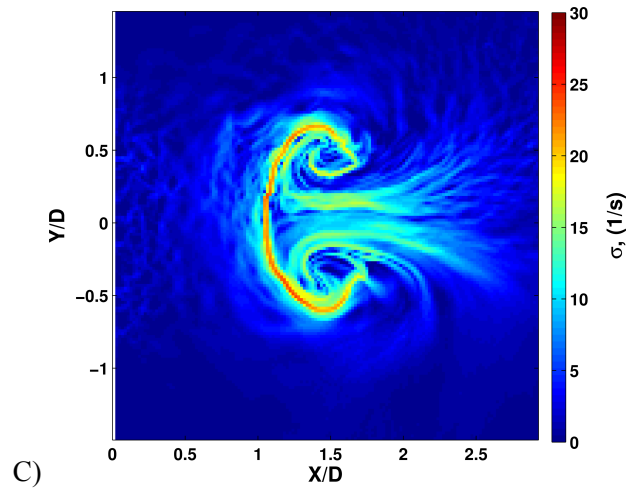
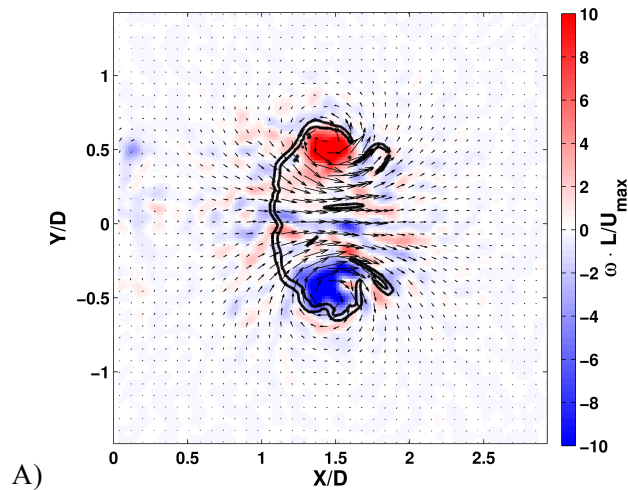


Figure 3.14. Results for the experimental data from a laminar vortex ring. A), B), and C) show the FTLE results for the numerical integration, sequential Lagrangian tracking, and the PTV flow map interpolation respectively.

To better illustrate the relationship between the separatrix and the vortex ring vorticity field, Figure 3.15 shows the vorticity field overlaid with the separatrix from the numerical integration and PTV flow map interpolation. Again it can be seen that the PTV flow map interpolation appears less susceptible to noise in the velocity field as it produces a smoother separatrix. While the PTV method has less “structure” in the front (right side) of the vortex, this is attributed to noise and it is not actually present in the flow field.



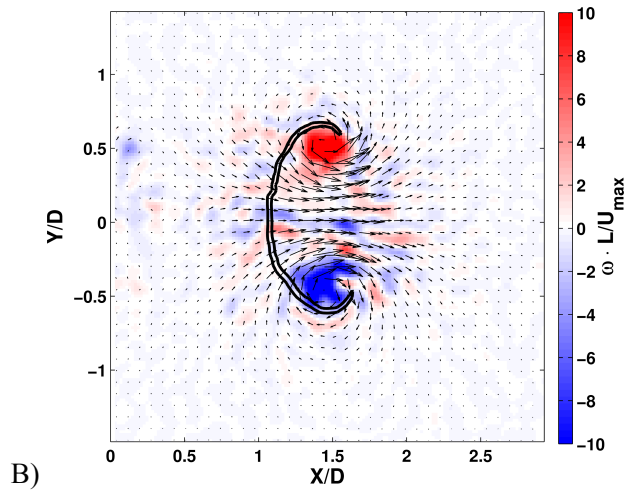


Figure 3.15. Separatrix overlaid with the non-dimensional vorticity field for the numerical integration (A) and the PTV flow map interpolation (B).

3.9. Conclusions

This work presents two new methods for computing FTLE fields based on sequential Lagrangian tracking and PTV flow map interpolation, and compares them against the traditional numerical integration of velocity field data. The focus is on application to noisy fluid measurements using PIV or PTV generated data where we take advantage of the fact that the flow map information is inherently contained in the Lagrangian motion of the particle flow tracers. Using this fundamental principle we show that the FTLE fields can be calculated with increased accuracy directly from the measured particle trajectories.

We show that PTV flow map interpolation produces the most accurate estimates of the FTLE field for both synthetic data as well as experimental data. For cases where particle loss between frames is minimal, the sequential Lagrangian tracking can produce reasonable results but can also be significantly affected by the unstructured nature of the data on which the flow maps are based upon. As sequential Lagrangian tracking is following the complete particle path, and thus should provide the best estimate of the particle flow map, it is note worthy that it does not perform as PTV flow map interpolation. When comparing the ability to resolve the true separatrix of a flow field, the PTV flow map interpolation was

shown to be far superior with an average overlap percentage of 80% as compared to ~25% and ~1% for the sequential Lagrangian tracking and numerical integration respectively.

The PTV flow map interpolation shows a significant advantage over the other methods when the particle seeding is low. This can be particularly important for applications to environmental or biological flows where adding seed particles is not practical and investigation of Lagrangian flow structures must rely on naturally occurring flow tracers to produce the flow map. These results also demonstrate that when analyzing experimental data it is advantageous to use the PTV flow map interpolation for the computation of FTLE/LCS over numerical particle integration. The method not only produces strong measures of the FTLE field but also outperforms numerical integration of data with near-wall flow fields. PTV flow map interpolation is also more computationally cost effective as each snap-shot of the flow map only needs to be interpolated once whereas numerical integration can require multiple iterations. The PTV flow map interpolation also requires far fewer massless flow tracer (16 times less for the synthetic data) and thus few computations than the numerical integration procedure.

Future work should investigate these methodologies on three-dimensional data sets. While not shown here, the methods described are directly applicable to three-dimensional data. This approach should increase the efficiency of the tracking-based methods as extension to 3D will increase the number of possible matches in the tracking procedure while numerically integrating velocity fields in 3D will become significantly more computationally expensive.

3.10. *References*

- Adrian, R. and J. Westerweel (2011). Particle Image Velocimetry, Cambridge University Press.
- Adrian, R. J. (1991). "Particle-Imaging Techniques For Experimental Fluid-Mechanics." Annual Review of Fluid Mechanics **23**(1): 261-304.
- Adrian, R. J. (2005). "Twenty years of particle image velocimetry." Experiments in Fluids **39**: 159-169.

- Brady, M. R., S. G. Raben, et al. (2009). "Methods for Digital Particle Image Sizing (DPIS): Comparisons and improvements." Flow Measurement and Instrumentation **20**(6): 207-219.
- Brunton, S. L. and C. W. Rowley (2010). "Fast Computation of Finite-Time Lyapunov Exponent Fields for Unsteady Flows." Chaos **20**: 1-12.
- Cardwell, N. D., P. P. Vlachos, et al. (2010). "A Multi-parametric Particle Pairing Algorithm for Particle Tracking in Single and Multiphase Flows." Measurement Science and Technology **22**.
- Charonko, J., R. Kumar, et al. (2013). "Vortices Formed on the Mitral Valve Tips Aid Normal Left Ventricular Filling." Annals of Biomedical Engineering **41**(5).
- Du Toit, P. C. (2010). Transport and separatrices in time dependent flows. Ph.D., California Institute of Technology.
- Dubuisson, M.-P. and A. K. Jain (1994). "A modified Hausdorff distance for object matching." Pattern Recognition **1**.
- Duncan, J., D. Dabiri, et al. (2010). "Universal outlier detection for particle image velocimetry (PIV) and particle tracking velocimetry (PTV) data." Measurement Science and Technology **21**(5): 057002.
- Eckstein, A. and P. P. Vlachos (2009). "Assessment of advanced windowing techniques for digital particle image velocimetry (DPIV)." Measurement Science and Technology **20**(7): 075402-075402.
- Eckstein, A. and P. P. Vlachos (2009). "Digital particle image velocimetry (DPIV) robust phase correlation." Measurement Science & Technology **20**(5).
- Etebari, A. and P. P. Vlachos (2005). "Improvements on the accuracy of derivative estimation from DPIV velocity measurements." Experiments in Fluids **39**(6): 1040-1050.
- Haller, G. (2001). "Distinguished material surfaces and coherent structures in three-dimensional fluid flows." Physica D **149**: 248-277.
- Haller, G. (2002). "Lagrangian coherent structures from approximate velocity data." Physics of Fluids **14**(6): 1851-1861.
- Haller, G. (2011). "A variational theory of hyperbolic Lagrangian Coherent Structures." Physica D **240**(7): 574-598.
- Haller, G. and G. Yuan (2000). "Lagrangian coherent structures and mixing in two-dimensional turbulence." Physica D **147**: 352-370.

- Holmes, P., J. L. Lumley, et al. (1996). Turbulence, Coherent Structures, Dynamical Systems and Symmetry, Cambridge University Press.
- Kahler, C. J., S. Scharnowski, et al. (2012). "On the uncertainty of digital PIV and PTV near walls." Experiments in Fluids **52**(6): 1641-1656.
- Karri, S., J. Charonko, et al. (2009). "Robust wall gradient estimation using radial basis functions and proper orthogonal decomposition (POD) for particle image velocimetry (PIV) measured fields." Measurement Science & Technology **20**(4).
- Lekien, F. and S. D. Ross (2010). "The computation of finite-time Lyapunov exponents on unstructured meshes and for non-Euclidean manifolds." Chaos **20**(1): 017505.
- Lipinski, D. and K. Mohseni (2010). "A ridge tracking algorithm and error estimate for efficient computation of Lagrangian coherent structures." Chaos **20**(1).
- Mathur, M., G. Haller, et al. (2007). "Uncovering the Lagrangian Skeleton of Turbulence." Physical Review Letters **98**: 1-4.
- Mikheev, a. V. and V. M. Zubtsov (2008). "Enhanced particle-tracking velocimetry (EPTV) with a combined two-component pair-matching algorithm." Measurement Science and Technology **19**(8): 085401-085401.
- Ohmi, K. and H.-y. Li (2000). "Particle-tracking velocimetry with new algorithms." Measurement Science and Technology **11**: 603-616.
- Ohmi, K. and S. P. Panday (2009). "Particle Tracking Velocimetry using the genetic algorithm." Journal of Visualization **12**(3): 217-232.
- Olcay, A. B., T. S. Pottebaum, et al. (2010). "Sensitivity of Lagrangian coherent structure identification to flow field resolution and random errors." Chaos **20**(1): -.
- Peng, J. and J. O. Dabiri (2009). "Transport of Inertial Particles by Lagrangian Coherent Structures: Application to Predator-Prey Interaction in Jellyfish Feeding." Journal of Fluid Mechanics **623**: 75-84.
- Raffel, M., C. E. Willert, et al. (1998). Particle image velocimetry, Springer-Verlag.
- Ruiz, T., J. Boree, et al. (2010). "Finite time lagrangian analysis of an unsteady separation induced y a near wall wake." Physics of Fluids **22**(7): 075193.
- Scarano, F. (2002). "Iterative image deformation methods in PIV." Measurement Science and Technology **13**.
- Scarano, F. and M. L. Riethmuller (1999). "Iterative multigrid approach in PIV image processing with discrete window offset." Experiments in Fluids **26**(6): 513-523.

- Senatore, C. and S. D. Ross (2011). "Detection and characterization of transport barriers in complex flows via ridge extraction of the finite time Lyapunov exponent field." International Journal for Numerical Methods in Engineering **86**: 116301174.
- Shadden, S. C. (2011). Lagrangian Coherent Structures. Transport and Mixing in Laminar Flows: From Microfluidics to Oceanic Currents. R. Grigoriev. Weinheim, Germany, Wiley-VCH Verlag GmbH & Co. KGaA.
- Shadden, S. C., J. O. Dabiri, et al. (2006). "Lagrangian analysis of fluid transport in empirical vortex ring flows." Physics of Fluids **18**: 1-11.
- Shadden, S. C., K. Katija, et al. (2007). "Transport and stirring induced by vortex formation." Journal of Fluid Mechanics **593**: 315-331.
- Shadden, S. C., F. Lekien, et al. (2005). "Definition and properties of Lagrangian coherent structures from finite-time Lyapunov exponents in two-dimensional aperiodic flows." Physica D **212**: 271-304.
- Shinnee, A., R. Balachandar, et al. (2006). Quantitative Investigation of Coherent Structures in a Free Jet Using PIV and POD. ASME Joint U.S. - European Fluids Engineering Summer Meeting. Miami, FL: 1-8.
- Sirovich, L. (1987). "Turbulence and the Dynamics of Coherent Structures I-III." Quarterly of Applied Mathematics **45**: 567-571,573-590.
- Solomon, T. H. and J. P. Gollub (1988). "Chaotic Particle-Transport in Time-Dependent Rayleigh-Benard Convection." Physical Review A **38**(12): 6280-6286.
- Solomon, T. H. and J. P. Gollub (1988). "Passive Transport in Steady Rayleigh-Benard Convection." Physics of Fluids **31**(6): 1372-1379.
- Stewart, K., C. Niebel, et al. (2012). "The decay of confined vortex rings." Experiments in Fluids: 1-9.
- Tallapragada, P. and S. D. Ross (2008). "Particle segregation by Stokes number for small neutrally buoyant spheres in a fluid." Physical Review E **78**: 1-9.
- Tallapragada, P. and S. D. Ross (2013). "A set oriented definition of finite-time Lyapunov exponents and coherent sets." Communications in Nonlinear Science and Numerical Simulation **18**(5): 1106-1126.
- Westerweel, J. and F. Scarano (2005). "Universal outlier detection for PIV data." Experiments in Fluids **39**(6): 1096-1100.
- Wilson, M. M., J. Peng, et al. (2009). "Lagrangian coherent structures in low Reynolds number swimming." Journal of Physics-Condensed Matter **21**.

Zhao, C., W. Shi, et al. (2005). "A new Hausdorff distance for image matching." Pattern Recognition Letters **26**(5).

4. Experimental Three Dimensional Lagrangian Coherent Structures of Inertial Particles in Flows

4.1. Abstract

This work provides an experimental method for simultaneously measuring finite time Lyapunov exponent fields for multiple particle groups, including non-flow tracers, in three-dimensional multiphase flows. From sequences of particle images, e.g., from fluid experiment imaging techniques, we can directly compute the flow map and coherent structures, skipping the computationally costly numerical integration. This is especially useful for finding three-dimensional Lagrangian coherent structures for inertial particles, which do not follow the bulk fluid velocity, as we demonstrate for a grid turbulence experiment. The technique described may provide a new means for exploring the physics of experimental multi-phase flows.

Finite Time Lyapunov Exponents (FTLE) are a powerful and increasingly popular tool for describing mixing and transport in both turbulent and laminar flow fields (Haller 2001; Brunton and Rowley 2010). FTLEs provide a measure of the exponential rate of divergence or convergence of Lagrangian particle trajectories and can be used both experimentally and numerically to describe a flow field, which may have a high degree of spatiotemporal complexity (Haller 2001; Shadden, Katija et al. 2007). While primarily used to describe single-phase flow behavior (Haller 2001; Haller 2005; Shadden, Dabiri et al. 2006) some works have attempted to account for inertial particles by modeling the particles' motion through simulations (Haller and Sapsis 2008; Tallapragada and Ross 2008; Peng and Dabiri 2009). This procedure can provide insight, but does not provide direct information about the true observable inertial particle trajectories. Often, the inertial particle equations of motion make simplifying assumptions (e.g., the Maxey-Riley equations (Maxey and Riley 1983)) which lead to significant differences between the

modeled and true motion. This brief communication reports a method to directly determine FTLEs from experimental data for inertial particles through the use of particle tracking velocimetry (PTV) without any a-priori assumptions about particle motion.

FTLEs are computed via the Cauchy-Green deformation tensor C_{jk} ,

$$C = \left(\nabla \Phi_{t_0}^{t_0+T} \right)^* \cdot \nabla \Phi_{t_0}^{t_0+T} \quad (4.1)$$

where $*$ denotes transpose, and $\Phi_{t_0}^{t_0+T}$ is the flow map (diffeomorphism) of particle locations from time t_0 to t_0+T . From the maximum eigenvalue of C , the FTLE field defined in the measurement volume is,

$$\sigma_{t_0}^{t_0+T} = \frac{1}{|T|} \ln \left(\sqrt{\lambda_{\max}(C)} \right) \quad (4.2)$$

It is typical when computing FTLEs from experimental data to use a numerical integration routine to numerically advect artificial tracer particles to determine the flow map from the estimated velocity field (Shadden, Dabiri et al. 2006; Shadden, Katija et al. 2007; Lekien and Ross 2010). While this can be effective for single-phase flow it neglects the fact that inertial particles, bubbles, or active particles may fail to follow the bulk fluid motion or the fact that tracking individual particles can provide a direct measure of a short duration flow map. While numerical routines can be modified to estimate inertial particle behavior via modeling as mentioned above, this procedure does not directly measure inertial particle trajectories. However, using time resolved PTV to obtain snap shots of the particle motion allows direct measurement of the particle flow map while also allowing for parameterization of the particle flow map based on unique identifying characteristics, such as size, shape or color, providing, e.g., a one-parameter family of particle flow maps with particle size as the parameter. The concept of merging small flow map snap shots to estimate a complete flow map was put forth by Brunton and Rowley (Brunton and Rowley 2010) for results of fluid computations and later adapted for experimental data as PTV interpolation by Raben et al. (Raben, Ross et al. 2013). Through this method it is possible to

simultaneously determine FTLEs for multiple particle groups within the same measurement volume and compare them to the bulk flow field. It has also been shown that this method can provide high accuracy flow map computation results even when the particle concentration drops below what is typically used for PIV/PTV (Raben, Ross et al. 2013). This is an important aspect; when the particles are separated into groups, some groups will have smaller particle population densities requiring a method suitable to provide high resolution FTLE information with low resolution velocity information in order to properly determining the FTLE values.

To study the motion of inertial particles in an experimental environment, data were collected in a vertical water tunnel that was designed to generate homogeneous isotropic grid turbulence, as described in (Raben, Charonko et al. 2012). For this experiment a bar thickness of the grid, b , of 0.3175 cm was used with the gap between bars equal to the width of the bar. Overlapping bars created a square lattice, which was located 8 cm upstream from the measurement location. Two different types of particles were added to the flow: $85 \pm 20 \mu\text{m}$ diameter silver coated hollow glass spheres that were tuned to be neutrally buoyant and were used to act as flow tracers; and solid glass particles with diameters ranging from approximately 150 - 200 μm that were added downstream (top of the tunnel) and had an approximate mass density of 2600 kg/m^3 . The vertical nature of the tunnel created opposing motion as gravity pulled the negatively buoyant particles down while the bulk flow was moving mostly upward.

Time resolved imaging techniques such as particle image velocimetry (PIV) have made it possible to study the Lagrangian motion of a flow field experimentally (Mathur, Haller et al. 2007; Shadden, Katija et al. 2007). With the recent development of volumetric image techniques (Elsinga, Scarano et al. 2006) it is now possible to investigate particle trajectories in a fully three-dimensional flow field. Because these imaging techniques make no assumptions on particle motion (e.g., must be a tracer following the bulk flow) they can be effective in capturing non-flow tracer particle motion (e.g., inertial particles) as well as bulk flow motion.

Time resolved tomographic imaging was used to collect information on the complete particle field as well as fully resolve the three-dimensional fluid motion. A New Wave Pegasus laser was used to illuminate all the particles in the measurement volume. Three Photron FASTCAM APX-RS high-speed CMOS cameras were used to simultaneously image this light field, recording images at 250 Hz. These images were reconstructed into a three-dimensional light intensity distribution using the Multiplicative Algebraic Reconstruction Technique employ in the DaVis 8.1 software (Herman and Lent 1976; Elsinga, Scarano et al. 2006).

Once the images have been reconstructed, the particles' size and motion are determined. Particles were first located in the volume using a simple thresholding method and then sized using an intensity weighted pixel count. In an effort to track the particles, a multi-component particle tracking algorithm developed for single and multiphase flows (Cardwell, Vlachos et al. 2010) was adapted to three-dimensional data. The method worked by comparing unique particle identifiers, such as size, peak intensity, and proximity, to match particles in consecutive images. This method has been shown to work well in turbulent flows even with non-flow tracers (Cardwell, Vlachos et al. 2010).

Figure 4.1 shows a histogram of the particle sizes present in the measurement volume. Due to factors such as camera arrangement and the MART reconstruction algorithm (Herman and Lent 1976), the particle size may be over-estimated. As these factors should affect all particles equally, and the concern here is not exact particle size but rather relative size, this should not affect the results. For this study, the particle size distribution was divided into only three groups. The first group was small particles, most likely including the tracer particles that should follow the bulk fluid motion. The second group was medium particles, which contained a mixture of flow tracers and smaller silica particles. The final group was the large particles, primarily the large glass particles that will tend not to follow the bulk fluid motion. When computing the FTLE field, the complete particle distribution was used as a control, as this total group provides an estimate of the FTLE field that would be found if no particle sizing procedure had been applied to the data and all the particles were (erroneously) treated as flow tracers.

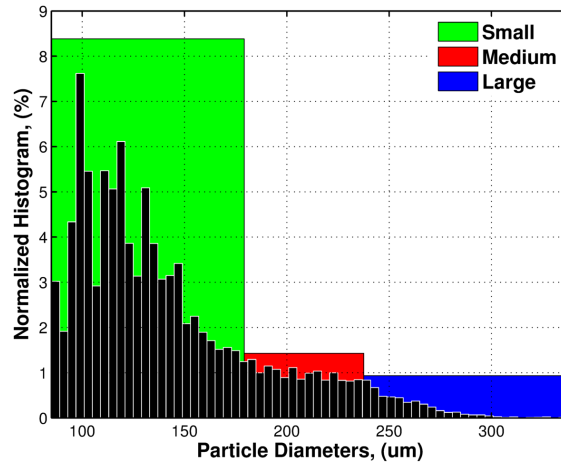


Figure 4.1. Normalized particle diameter distribution within the measurement volume.

For each particle group, the FTLE field can be calculated with an integration time of 1s which is equal to 250 frames. For two-dimensional flows, FTLE fields are often characterized by the elevated ridges, or connected lines with high FTLE values, which are referred to as Lagrangian coherent structures (LCS) and reveal hyperbolic or shear-dominated structures. In three-dimensional fields, the locus of elevated values are two-dimensional surfaces. Figure 4.2 shows iso-surfaces of high FTLE values as proxies for true ridges for both the forward and backward FTLE fields. Ridges in the forward FTLE field reveal repelling surfaces where particles are exponentially diverging away from one another while the backward FTLE shows attracting surfaces which may be related to clustering cores for inertial particles. From Figure 4.2A it can be seen that there is a significant difference in the FTLE fields based on the particle size. The iso-surface for the large particle group is dominated by a large structure in the upper left of the domain. It could be seen from the raw data that during this time that there was an influx of larger particles that begin to spread throughout the volume, which would explain the elevated FTLE values in this region. For the small particle group the iso-surface shows a structure that extends from the lower right of the domain up to the top. This structure could indicate that the influx of large particles

forced the flow tracers to be redirected around the large particle cluster causing a divergence in the small particle trajectories.

Figure 4.2B shows the backward FTLE, which will indicate locations of particle clustering. Previous works that have investigated particle clustering have used the second invariant of the velocity gradient tensor, Q , sometimes referred to as the Okubo-Weiss parameter, as an indicator for where particles are likely to found, (Squires and Eaton 1991; Eaton and Fessler 1994; Guala, Liberzon et al. 2008; Haller and Sapsis 2008) where Q is defined as:

$$Q = \frac{1}{2}(\omega^2 - s^2) \quad (4.3)$$

with ω and s representing vorticity and strain rate, respectively. For scaling purposes Q is often normalized by the ensemble average of vorticity squared, $Q^* = Q / \langle \omega^2 \rangle$, as was done here and produced normalized values between -1.5 and 0.5 which is in agreement with the literature for turbulent flow (Guala, Liberzon et al. 2008). When Q^* is negative this indicates a region of high strain and low vorticity, which, when particles are added to the flow, has been shown to correlate with preferential particle concentration (Squires and Eaton 1991; Eaton and Fessler 1994; Guala, Liberzon et al. 2008; Haller and Sapsis 2008). To illustrate regions where particles should cluster a Q^* iso-surface showing the location of three standard deviation away from the zero in the negative direction based on the mean field, is also shown in Figure 4.2. It can be seen from Figure 4.2B that while there exist some smaller regions of high backward FTLE throughout the domain, the attracting LCS locations are predominantly located near the location of higher negative Q^* . Since the flow is time-dependent, there is no reason to expect perfect agreement between the Eulerian Q^* field and attracting LCSs.

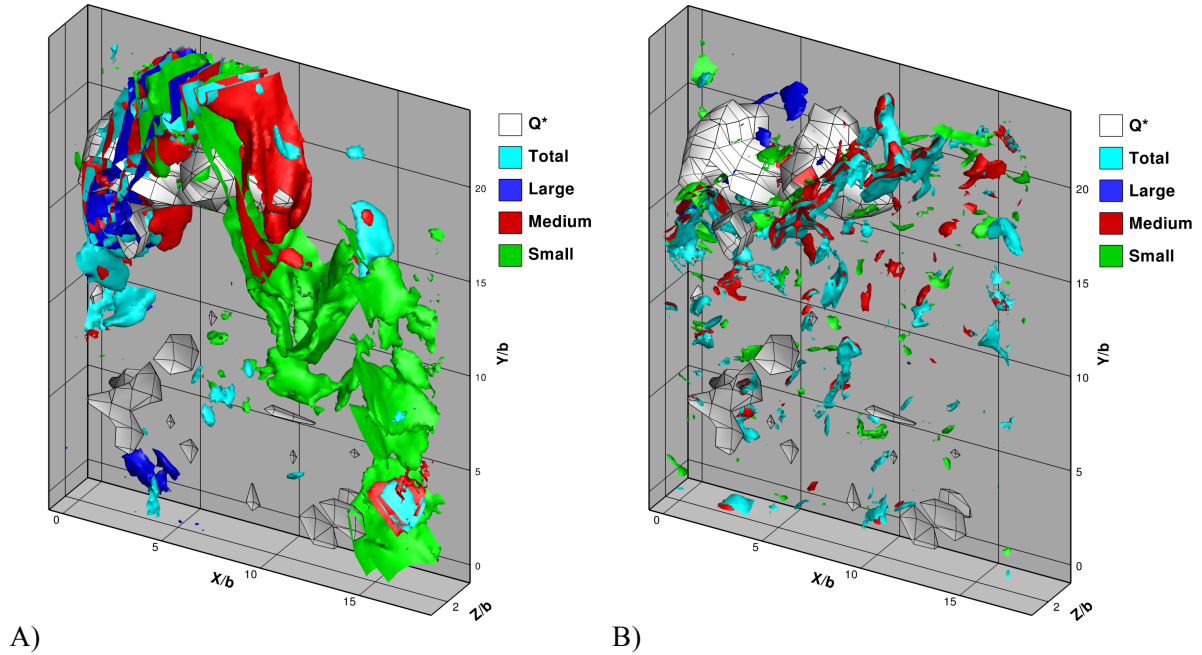


Figure 4.2. Iso-surfaces of the forward (A) and backward (B) FTLE fields based on the different components in the flow.

To further investigate the locations of particle clustering, Figure 4.3 shows backward FTLE values on the center Z plane for each of the 4 different particle groupings, where a thick black line representing the same iso-contour of Q^* is included. In addition an iso-contour for -3.0 and -1.5 times the standard deviation and a zero contour are also included. It can be seen from this figure that while there are some similarities in the locations of the elevated backward FTLE values between the different groups, there are also some important differences. Figure 4.3A shows the FTLE field for the total particle group, which we note is not a superposition of the FTLE field for the size-based groups. Elevated FTLE values are seen in close proximity to the highly negative Q^* values as this will be a location where particles will cluster (Guala, Liberzon et al. 2008). For the large particles, Figure 4.3D, elevated values are again seen near highly negative Q^* but in a different location from that seen with the total particle group. In this case the large particles appear attracted to a region just above the Q^* iso-contour, on the opposite side from zero Q^* iso-contour (the zero iso-contour would suggest particle repulsion). The large particles also have a

lower maximum FTLE value, which may indicate that their attraction to this region is not as strong as some of the other particles groups.

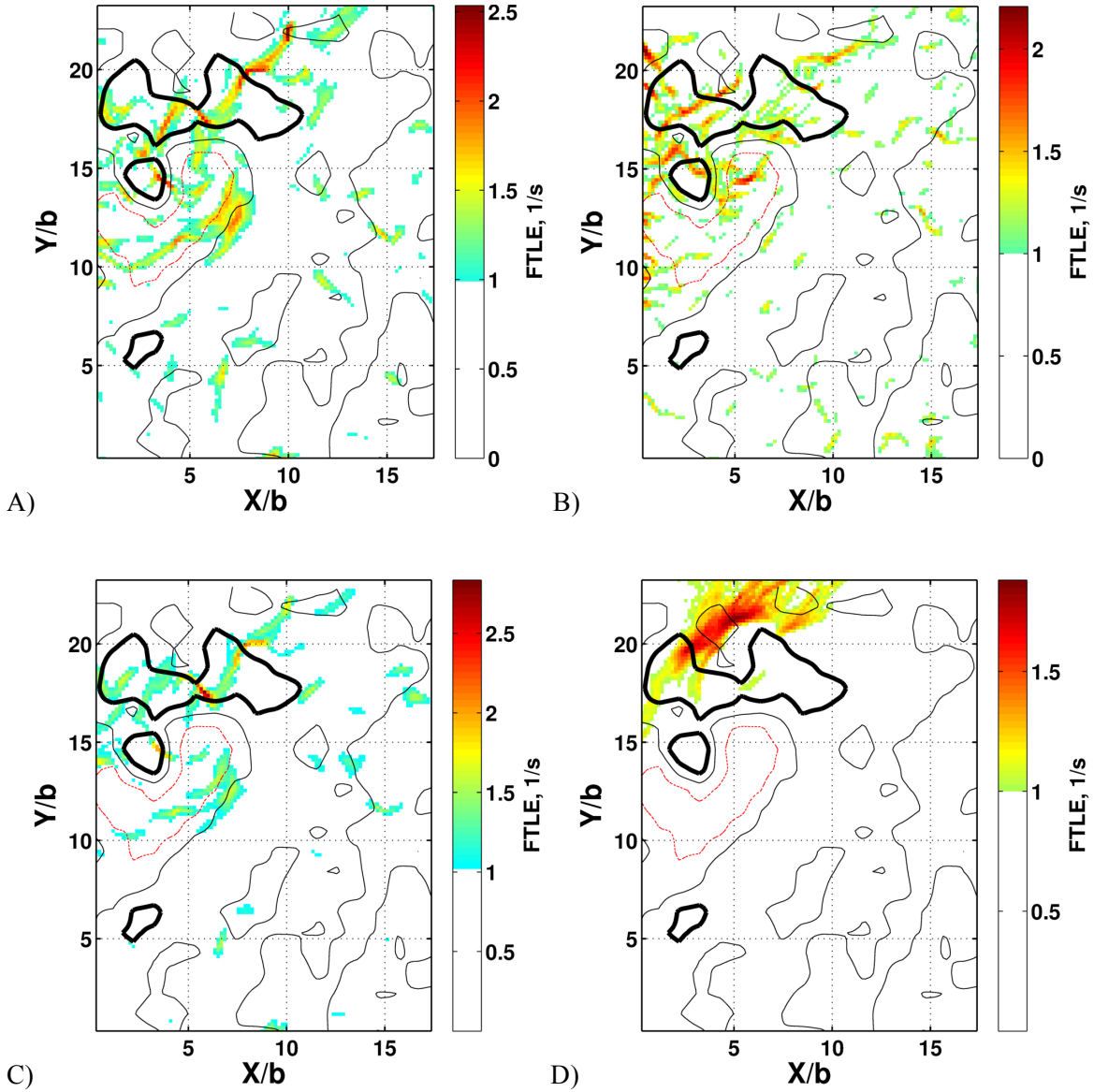


Figure 4.3. Contours of Backward time FTLE values for the total location of particles A), the small particle sizes B) the medium particles sizes C) and finally the large particle sizes, D). The thick line shows iso-contour for -3 std (surface shown in Figure 4.2), while the thick line shows an iso-contour for -1.5 std and the dashed line is the zero iso-contour.

The medium particle group also has elevated FTLE values in close proximity to the Q^* strongly negative iso-contour, as seen in Figure 4.3C. As this group is most likely a collection of flow tracers and

smaller inertial particles it is interesting to see that very high FTLE values appear to be located inside the Q^* iso-contour mean that particle clustering associated with this group most closely coincides with the Q^* grouping. For the smallest particles, Figure 4.3B, it can again be seen that the elevated FTLE values are located near the Q^* iso-contour. This particle group appears to have more scatter than the other groups which is mostly due to the fact that as flow tracers these particles are more susceptible to the turbulent fluctuations in the volume and thus will have a more spatially distributed structure. Again, because Q^* is an Eulerian field and ours is a temporally varying flow there is no expectation of perfect agreement with the LCS but it does help to illustrate the behavior.

To summarize, this work has shown that three-dimensional FTLE fields can be calculated for inertial particles in experiments through the use a non-flow tracer flow map determination technique that uses particle tracking and sizing information to directly measure the size-parameterized families of flow maps. The use of particle tracking for the direct calculation of the FTLEs is an important advancement as it is capable of uniquely determining the flow maps for different groups of particles, e.g., grouped by size in our experiment, but other parameterizations are possible. Using this method it is possible to directly measure inertial particle FTLE fields and Lagrangian coherent structures without making assumptions about the underlying particle equations of motion. This may have relevance for the experimental study of inertial particle motion in fluids and multi-phase flows.

4.2. References

- Brunton, S. L. and C. W. Rowley (2010). "Fast Computation of Finite-Time Lyapunov Exponent Fields for Unsteady Flows." *Chaos* **20**: 1-12.
- Cardwell, N. D., P. P. Vlachos, et al. (2010). "A Multi-parametric Particle Pairing Algorithm for Particle Tracking in Single and Multiphase Flows." *Measurement Science and Technology* **22**.

- Eaton, J. K. and J. R. Fessler (1994). "Preferential Concentration of Particles by Turbulence." International Journal of Multiphase Flow **20**: 169-209.
- Elsinga, G. E., F. Scarano, et al. (2006). "Tomographic particle image velocimetry." Experiments in Fluids **41**(6): 933-947.
- Guala, M., A. Liberzon, et al. (2008). "Experimental study on clustering of large particles in homogeneous turbulent flow." Journal of Turbulence **9**(34): 1-20.
- Haller, G. (2001). "Distinguished material surfaces and coherent structures in three-dimensional fluid flows." Physica D **149**: 248-277.
- Haller, G. (2005). "An objective definition of a vortex." Journal of Fluid Mechanics **525**: 1-26.
- Haller, G. and T. Sapsis (2008). "Where do inertial particles go in fluid flows?" Physica D-Nonlinear Phenomena **237**(5): 573-583.
- Herman, G. T. and A. Lent (1976). "Iterative Reconstruction Algorithms." Computers in Biology and Medicine **6**(4): 273-294.
- Lekien, F. and S. D. Ross (2010). "The computation of finite-time Lyapunov exponents on unstructured meshes and for non-Euclidean manifolds." Chaos **20**(1): 017505.
- Mathur, M., G. Haller, et al. (2007). "Uncovering the Lagrangian Skeleton of Turbulence." Physical Review Letters **98**: 1-4.
- Maxey, M. R. and J. Riley (1983). "Equations of motion for a small rigid sphere in a nonuniform flow." Physics of Fluids **26**(4): 883.
- Peng, J. and J. O. Dabiri (2009). "Transport of Inertial Particles by Lagrangian Coherent Structures: Application to Predator-Prey Interaction in Jellyfish Feeding." Journal of Fluid Mechanics **623**: 75-84.
- Raben, S., J. Charonko, et al. (2012). "Adaptive gappy proper orthogonal decomposition for particle image velocimetry data reconstruction." Measurement Science and Technology **23**(2).

- Raben, S. G., S. D. Ross, et al. (2013). "Computation of Finite Time Lyapunov Exponents from Time Resolved Particle Image Velocimetry Data." Submitted to Experiments in Fluids.
- Shadden, S. C., J. O. Dabiri, et al. (2006). "Lagrangian analysis of fluid transport in empirical vortex ring flows." Physics of Fluids **18**: 1-11.
- Shadden, S. C., K. Katija, et al. (2007). "Transport and stirring induced by vortex formation." Journal of Fluid Mechanics **593**: 315-331.
- Squires, K. D. and J. K. Eaton (1991). "Preferential Concentration of Particles by Turbulence." Physics of Fluids a-Fluid Dynamics **3**(5): 1169-1179.
- Tallapragada, P. and S. D. Ross (2008). "Particle segregation by Stokes number for small neutrally buoyant spheres in a fluid." Physical Review E **78**: 1-9.

5. The Developing Region of Wall-Jets

5.1. Abstract

Wall jets have many applications in engineering ranging from active flow control to film cooling. While a large number of studies have focused on the fully developed flow regime where wall-jets exhibit self-similar velocity profiles, this study investigates the developing flow region and provides scaling arguments for their growth and behavior. Firstly, this work provides a relationship for development length, which describes the length of the inviscid core of the jets downstream of the exit, as a function of Reynolds number which has yet to be applied to wall-jets. The development length illustrates the diffusion of momentum from the core and the behavior of the jet. During this diffusion of momentum the velocity profiles evolve in the streamwise and vertical directions creating a highly anisotropic flow governed by an inner wall-bounded shear-layer and an outer free shear-layer. This work provides scaling relationships for the growth of these layers, which are denoted by the location where the velocity profile is one half of its maximum (referred as $Y_{1/2}^T$ and $Y_{1/2}^B$ respectively). It is shown that these layers grow linearly as a function of streamwise location. A Reynolds number independent scaling is also provided for the $Y_{1/2}^B$ with respect to the boundary layer momentum thickness. We also find that the locations of $Y_{1/2}^T$ and $Y_{1/2}^B$ coincide with the locations of peak Reynolds stress. This collocation asserts that these locations not only scale the profile but also identify the shear layer locations. Vortex formation is another mechanism that is used to diffuse momentum and aids in the development of these jets. This work uses vortex identification to show the location of vortex formation as a function of Reynolds numbers as well as shows a clear agreement between vortex location and the $Y_{1/2}^T$ and $Y_{1/2}^B$ locations.

5.2. Introduction

Wall-jets are formed by injecting high-speed momentum driven fluid along the surface of a wall. As such, these flows are characterized by strong anisotropy especially along the wall-normal direction

because the inner (near-wall) flow resembles a boundary layer while the outer region corresponds to a free shear layer. Since the early work by Glauert (1956), wall-jets have received attention primarily due to their importance to many engineering applications including heating and cooling, film cooling in gas-turbines, and aerodynamic flow control. The review by Launder and Rodi extensively discusses the physics and state-of-the-art up until 1983 (Launder and Rodi 1983). This work, like the many that followed, focused on the fully developed downstream region of the jet leaving the development region largely unstudied. Because many engineering applications employ wall jets inside the development region, a full understanding of the development region flow is important for proper utilization.

Chun and Schwarz (1967) showed that for wall jets, the critical Reynolds number for transition to turbulence is on the order of 57. Based on this knowledge, we can assume that for most engineering applications wall jets will either be transitional or fully turbulent. The transfer of momentum from the core of the jet to the outer flow dominates the development process for these jets. One important parameter that has yet to be investigated for wall jets is the development length (Wang and Law 2002; Lee and Chu 2003), which is the streamwise location at which the centerline velocity begins to decay as the profile transitions, for example from a top-hat exit profile to a more self-similar Gaussian shape. Understanding the importance of this length scale, as well as the transfer of momentum will help to provide a better understanding of the profile development.

Fully developed turbulent wall jets have been shown to possess a self-similar profile, allowing for scaling parameters to be applied across a large range of Reynolds numbers (Schneider and Goldstein 1994; Amitay and Cohen 1997). The anisotropic characteristics of this turbulent flow, large velocity dynamic range, regions of high shear, and the variation in length scales combine to generate a formidable flow field that challenges conventional experimental methods. Previous studies typically used point measurement methods such as hot wire, Pitot probe, and Laser Doppler Anemometry (LDA) to deliver either high spatial resolution (Karlsson, Eriksson et al. 1992; Grissom, Smith et al. 2007) or temporal resolution (Bajura and Szweczyk 1975) and primarily focused on the fully developed regime of the flow.

Scaling of wall-jet growth has received significant attention (Launder and Rodi 1981; Wygnanski, Katz et al. 1992; Eriksson, Karlsson et al. 1998; George, Abrahamsson et al. 2000; Afzal 2005; Barenblatt, Chorin et al. 2005). However, because of the differences in length scales governing the inner and outer flow regions, complete scaling is difficult. This challenge is more pronounced in the developing flow regime where the flow is not yet self similar. Often the scaling is based on the vertical distance from the wall at which the velocity is equal to one-half of the maximum streamwise velocity as illustrated by Figure 5.1. Given the asymmetry of the flow, this yields two characteristic heights of $Y_{1/2}^T$ and $Y_{1/2}^B$ for the outer and inner region respectively. This approach has been proven effective for scaling the velocity profiles across Reynolds numbers and streamwise locations (Launder and Rodi 1981; Launder and Rodi 1983; Karlsson, Eriksson et al. 1992; Schneider and Goldstein 1994; Eriksson, Karlsson et al. 1998) and Barenblatt, Chorin et al. (2005) showed that $Y_{1/2}^T$ and $Y_{1/2}^B$ can be used to formulate a model to account for the incomplete similarity of the jet.

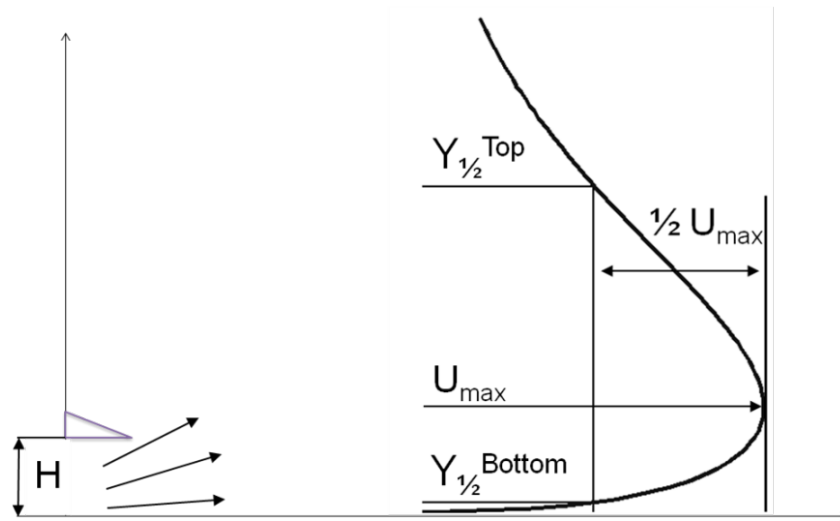


Figure 5.1. Diagram showing the two vertical locations used for scaling. The top and bottom regimes are the locations where the U velocity is one half the maximum.

The scaling of these vertical locations ($Y_{1/2}^T$ and $Y_{1/2}^B$) with respect to the streamwise location has also been the subject of several investigations. The growth of $Y_{1/2}^T$ was first thought to be linear (Launder and

Rodi 1983; Karlsson, Eriksson et al. 1992; Eriksson, Karlsson et al. 1998). Later it was postulated that with regards to downstream locations at $X/H > 20$, where X/H is the streamwise distance from the jet slot, the growth behaves more like a power law (George, Abrahamsson et al. 2000; Barenblatt, Chorin et al. 2005). This idea was improved upon by Barenblatt, Chorin et al. (2005) by looking at the scaling of the $Y_{1/2}^B$ as well as $Y_{1/2}^T$. In their work, Barenblatt et al. showed these length scales are sufficient to completely scale these jets as well as provided growth rates for $Y_{1/2}^T$ and $Y_{1/2}^B$ at the downstream locations.

Bajura and Szewczyk (1975) showed that the transition process for wall jets contains multiple stages which rely heavily on vortex formation and coalescences between the inner and outer regions of the jet. However, their work only had illustrative depictions of the process. Gogineni and Shih (1997) and Gogineni, Visbal et al. (1999) investigated transitional wall jets both numerically as well as through the use of PIV. These works showed the effect of vortex formation inside as well as outside of the outer shear layer. Although their study was limited to $Re=2150$, results clearly showed vortex pairing across the shear layer which led to break up and turbulent transition of the jet (Gogineni, Visbal et al. 1999).

The aim of this study is to resolve the flow characteristics of wall jets in the developing flow regime across a range of Reynolds numbers between $Re \sim 150-10,000$ (Re defined based on the jet slot height and exit velocity) and provide scaling arguments for the behavior and growth of these jets in this understudied region. The relationship of the development length to Reynolds number is investigated. Scaling relationships for the growth of $Y_{1/2}^T$ and $Y_{1/2}^B$ are also deduced as well as their relationship to the turbulence characteristics in this region. Vortex identification was used to show the relationship to the $Y_{1/2}^T$ and $Y_{1/2}^B$ in this development region and the effects of vortex formation.

5.3. Experimental Methods and Facilities

This experiment was conducted using a jet with a slot height (H) of 2 mm and an aspect ratio of 18.5:1 (jet width / height). A total of nine different Reynolds numbers were tested ranging from 150 –

10,000. The Reynolds numbers were based on the slot height and nozzle exit velocity. Table 5.1 shows each Reynolds number and corresponding exit velocity. The mid-spanwise plane of the jet was investigated, focusing on a 4 mm height by 22 mm width field of view (2H x 11H). Room temperature high-pressure dry air was supplied through a plenum connected to the jet slot through a one-sided bell-mouth contraction. Table 5.1 provides a summary of the experimental conditions and Figure 5.2 shows a schematic of the test setup.

Table 5.1. Experimental Parameters.

Reynolds Number	Jet Exit Velocity	Sampling Rate	Pulse Separation
150	1.10 m/s	1000 Hz	65 μ s
200	1.49 m/s	1000 Hz	47 μ s
750	5.63 m/s	1000 Hz	12 μ s
1,000	7.51 m/s	1000 Hz	9 μ s
1,500	11.25 m/s	1000 Hz	6 μ s
2,000	14.95 m/s	2000 Hz	5 μ s
5,000	37.47 m/s	2000 Hz	2 μ s
7,500	56.20 m/s	2000 Hz	1 μ s
10,000	75.44 m/s	2000 Hz	0.92 μ s

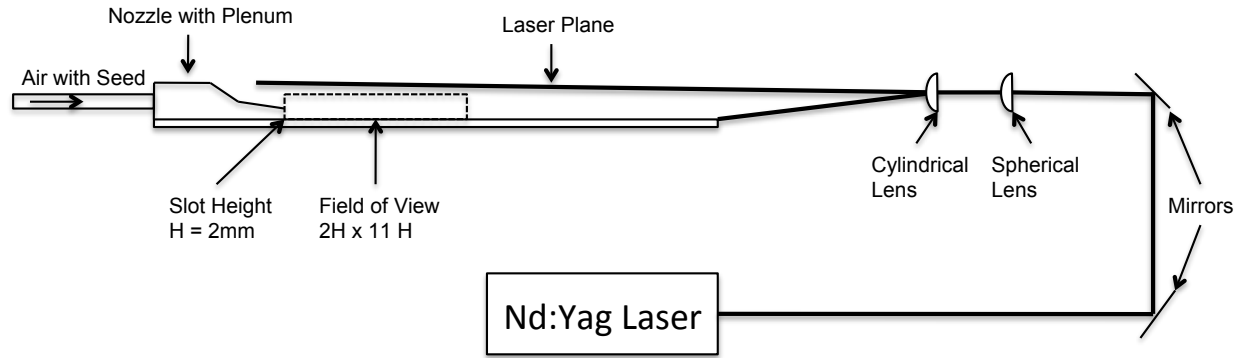


Figure 5.2. Experimental Setup. The red box represents the field of view of the camera while the green line is the laser plane entering from the right.

All measurements in this study were performed with Digital Particle Image Velocimetry (DPIV) using a Pegasus Nd:YAG dual head laser from New Wave. An IDT XS-5 CMOS digital camera with kHz sampling was utilized for data collection. To achieve the required sampling rate, the resolution was set to 256×1280 for all cases. The flow fields for the lower Reynolds numbers ($Re=150 - 1500$) were sampled at 1 kHz while cases for higher Reynolds numbers ($Re=2000 - 10000$) were sampled at 2 kHz. Pulse separations were optimized based on the flow speed and the desired DPIV resolution, ensuring that the recorded displacements did not exceed $\frac{1}{4}$ of the interrogation window size. Seeding was generated using a Laskin nozzle with Diethylhexel Sebacate (DHS). The estimated seeding density was 20 particles per 32×32 pixel window with an approximate droplet size of $1.0 \mu\text{m}$. Based on the fluid properties, the flow tracer Stokes number was on the order of 1×10^{-5} to 1×10^{-3} for velocity ranges of $1 - 75 \text{ m/s}$, respectively. Direct seeding of the outer flow was not performed in order to avoid any interaction (injection of momentum) of the seeding jet with the wall jet flow, which would inadvertently change the flow characteristics. Thus, only preexisting and residual flow tracers were present in the surrounding air above the shear layer, which resulted in fewer particles per interrogation window in the outer flow region.

All DPIV images were processed using an in-house developed open-source PIV software package PRANA², that utilizes the Robust Phase Correlation (RPC) technique (Eckstein, Charonko et al. 2008; Eckstein and Vlachos 2009; Eckstein and Vlachos 2009) coupled with a second-order discrete window offset technique (Scarano and Riethmuller 1999) and window deformation (Scarano 2002). The RPC method provides higher accuracy and reduces peak-locking effects versus standard cross-correlation techniques. Each Reynolds number was processed using a 64 x 32 pixel window for the first pass that used a Gaussian spatial filter reducing the effective window resolution down to 32 x 16 pixels. This first pass was iterated twice in order to refine the deformation (Scarano 2002). The second pass used uneven windows where a 16 x 8 pixel window was used to search a 32 x 16 pixel window in the second image. Uneven windows allow for a reduction in window size, which can yield an increase in resolution while still allowing for optimum particle displacement matching. Again, deformation iterations were performed to improve the accuracy. The final grid resolution produced a vector every 3 pixels or 422 x 81 (34182) vectors over the entire domain.

Due to the sensitivity of window deformation to erroneous measurements, the fields were validated and smoothed between each pass to prevent “tearing” in the images. The universal outlier detection (UOD) method was used to remove bad vectors (Westerweel and Scarano 2005). During the first PIV pass, two UOD passes were used between each iteration using a window size of 7 x 7 vectors and decreasing thresholds of 3 and 2 standard deviations. For the second PIV pass a UOD window size of 5 x 5 vectors with thresholds of 4 and 2.5 were performed. After validation, the fields were smoothed using a Gaussian smoothing function with the standard deviation set to 2 vectors. While this was performed between each of the PIV passes, with the exception of the final fields. A final pass of UOD was performed to catch any remaining vectors that may have presided.

² PRANA software is freely distributed as open source <http://sourceforge.net/projects/qi---tools/>

In an effort to remove any anomalies in the temporal information the data were filtered using proper orthogonal decomposition utilizing the method of snap shots (Sirovich 1989; Everson and Sirovich 1995). Here, the data was reconstructed such that 95% of the fluctuating energy was preserved which required between 1000 and 2300 modes depending on Reynolds number. This number is far less than 5000 snap shots processed, which assures that low order fields will be properly reconstructed and still contain the underlying physical information.

5.4. Results and Discussion

As mentioned in §1 wall jets can be divided into three different regimes: near-wall boundary layer, mixing layer, and outer shear layer. These three regimes are identified by the location of streamwise velocity equal to one-half of the maximum velocity. This happens at two locations along the profile and is noted as $Y_{1/2}^T$ and $Y_{1/2}^B$ in Figure 5.1, for the top and bottom locations respectively. Many previous works have shown that normalizing the vertical axis by the location of $Y_{1/2}^T$ produces a self-similar profile in fully developed jets (Karlsson, Eriksson et al. 1992; Schneider and Goldstein 1994; Barenblatt, Chorin et al. 2005). Our investigation focused in the region of $[X/H=0-11]$ where the flow is developing and the velocity profiles are not yet self-similar.

In order to compare with previous works, the normalized streamwise velocity profiles were plotted with respect to their $Y_{1/2}^T$ location, shown in Figure 5.3. The velocity profiles are normalized by the maximum velocity at each location, forcing all the profiles to have a maximum value of 1. All the Reynolds numbers are shown in each plot using different symbols, while the four plots correspond to different streamwise positions $X/H=1$, $X/H=4$, $X/H=8$, $X/H=11$ respectively. For the upstream locations the profiles resemble top-hat shapes while at the downstream locations, the profiles appear more Gaussian. This evolution and its dependence on Reynolds number will be discussed in the following section.

It can be seen that for the majority of the cases and for most of the streamwise positions, the velocity profiles fall closely on top of each other, especially for the top layer; however, they do not entirely collapse. Due to the extent of the range of Reynolds numbers considered in this study, it could be expected that different Reynolds number would develop at different rates which would explain the disagreement with the lower two Reynolds numbers. As stated by Barenblatt, Chorin et al. (2005) the wall jet presents an incomplete similarity where the entire profile can not scale by one characteristic length, which is illustrated by the disagreement between the profiles in the inner layer region. While scaling by the $Y_{1/2}^B$ would produce agreement in the lower region a similar disagreement would be seen in the top section of the profile. While this incomplete scaling has been shown for fully developed profiles this work shows that this dissimilarity is also evident in the development region for these jets.

The downstream velocity profiles that approximate the fully developed region strongly resemble previous results for similar experiments (Chun and Schwarz 1967; Launder and Rodi 1983; Schneider and Goldstein 1994; Gogineni, Visbal et al. 1999; Hall and Ewing 2007). In Figure 5.3D the empirical curve given by Schneider and Goldstein (1994), equation (5.1), is plotted along with the time averaged velocity profiles at streamwise location of $X/H = 11$. Because Schneider's work focused on the fully developed flow velocity profiles, good agreement was seen only for the farthest downstream locations of this study. The coefficients also needed to be modified in order to apply to this region. Here the empirical coefficients were found to be 2.4, 0.42, and 0.91 for C_1 , C_2 , and C_3 respectively which is different than those found by Schneider and Goldstein of 1.4, 0.28 and 0.66. The major reason for disagreement between these profiles, and thus a change in the coefficients, is the different growth rates for the $Y_{1/2}^T$ and $Y_{1/2}^B$ locations as well as the location of the maximum velocity, $Y_{U_{max}}$. In the development region, where the jet is just beginning to spread and the momentum is primarily in the core, the U_{max} location is more centered between the $Y_{1/2}^T$ and $Y_{1/2}^B$ heights as opposed to the fully developed downstream profiles which

has a U_{\max} proportionally closer to $Y_{1/2}^B$ location. The growth rate for $Y_{1/2}^T$ is sufficiently larger the $Y_{1/2}^B$ and thus exhibits greater spread in the fully developed profile as will be discussed later.

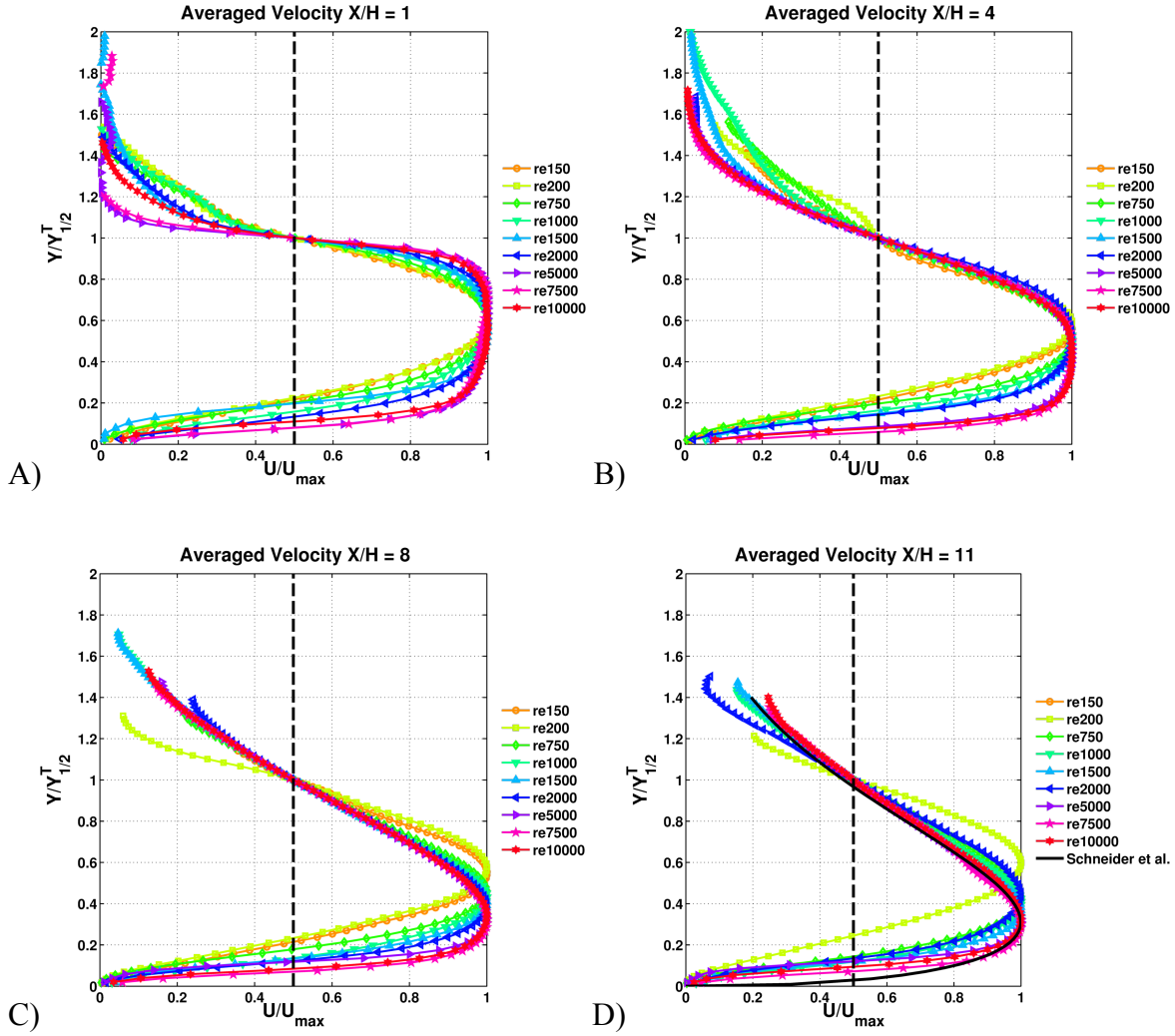


Figure 5.3. Time average velocity profiles for different Reynolds numbers at different X/H locations: A) X/H=1, B) X/H = 4, C) X/H = 8, D) X/H = 11.

$$\frac{U}{U_{\max}} = C_1 \left(\frac{Y}{Y_{1/2}^T} \right)^{C_2} \left[1.0 - \operatorname{erf} \left(C_3 \frac{Y}{Y_{1/2}^T} \right) \right] \quad (5.1)$$

5.4.1. Development Length and Scaling of Streamwise Velocity

The transfer of momentum from the core of the wall jet to its surroundings plays a large role in the development and behavior of the wall jet. One method that has been used for free round jets to describe the diffusion of momentum as the jet develops is to define a development length. The development length is the distance at which the inviscid core extends past the orifice and for turbulent round jets this value is typically 6.4 diameters (Wang and Law 2002; Lee and Chu 2003). While the development length has been studied for other types of jets, it has yet to be investigated with respect to wall jet data, partly due to the limited number of studies in the development region.

Figure 5.4 shows the development length for the different Reynolds as calculated by the location at which the time-averaged velocity drops below 2.5% of the maximum value. Noise in the images has effected the centerline for the $Re = 2000$ cases leading to a small inconsistency with the other cases. In order to provide a fair comparison with round jets this figure also includes development length as a function of hydraulic diameter (D_H). When comparing the development normalized by hydraulic diameter, the values are lower than what is expected from a free round jet, $D_H \sim 6.4$. This reduction is to be expected as viscous effects from the wall will cause the jet to break down more quickly than would be seen with a free jet. This figure also shows that for lower Reynolds number the core of the jet begins to break down over a relatively short length ($\sim 1H$) and starts diffusing momentum shortly after exiting the slot, while for larger Reynolds number the inviscid core is persistent for longer and requires more length to develop. The effects of development length are also see in Figure 5.3 where the lower Reynolds number cases begin to show a fully developed Gaussian shape more quickly than their higher Reynolds number counter parts. Good agreement is seen when fitting the development length using a logarithmic fit. Figure 5.4 also provides a logarithmic fit to the data as a function of Reynolds number. This fit shows that the development length grows as function of Reynolds number, almost tripling in length for every order of magnitude increase in Reynolds number. With respect to the hydraulic diameter the development length triples with an increase in two orders of magnitude in Reynolds number. This relationship means that in order to increase the development length a significant increase in Reynolds

number is required, which could impact implementation in engineering applications where increased develop length is advantageous.

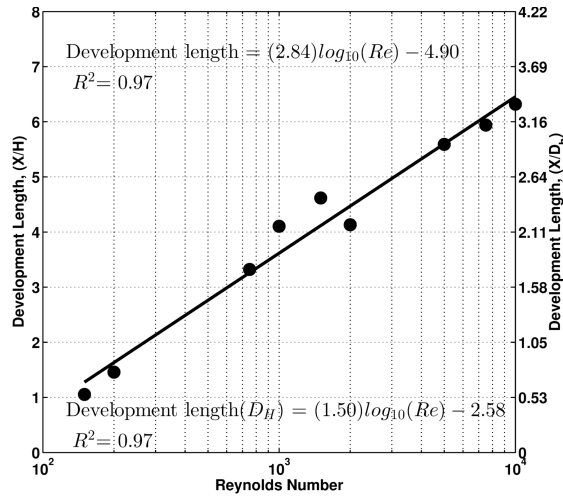


Figure 5.4. Development length as a function of Reynolds number.

The effect of the development length is also seen in the decay of streamwise velocity, Figure 5.5A. For each case no change in velocity is seen before the development length while a clear decay appears thereafter. Most previous studies that have investigated velocity decay rate have done so at downstream locations $X/H > 20$, and thus have not noticed this effect (Wynanski, Katz et al. 1992; Eriksson, Karlsson et al. 1998; George, Abrahamsson et al. 2000). Figure 5.5A shows that following the development length, a linear decay for each Reynolds numbers can be seen. Performing a linear fit to the velocity decay after the development length produces an average decay rate of -0.0245 ± 0.00457 (one standard deviation). Previous work has shown a Reynolds number dependence for the fully developed profiles (Wynanski, Katz et al. 1992) but in the development region this decay is constant.

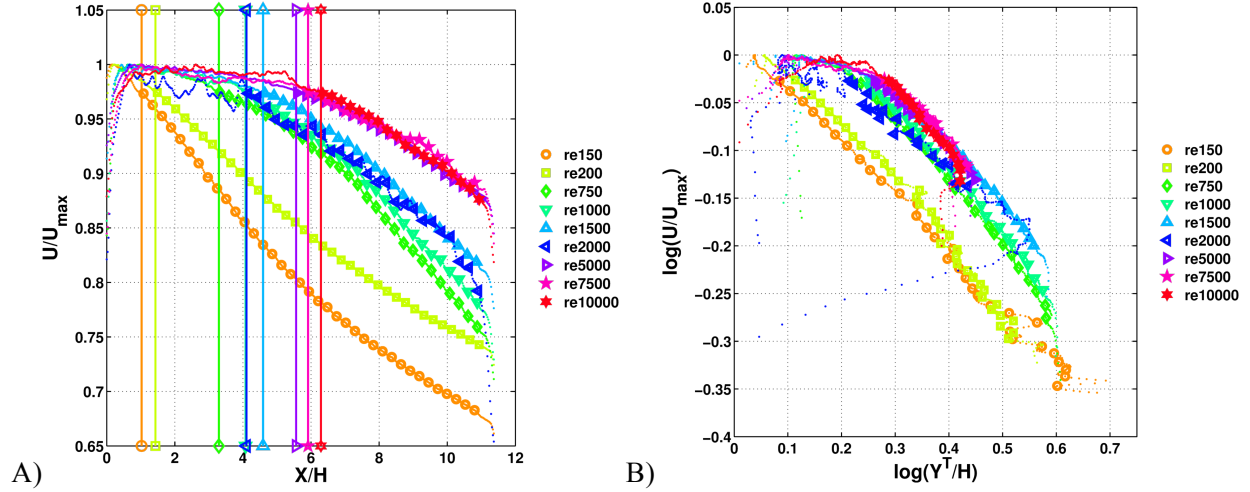


Figure 5.5. Decay of streamwise velocity as a function of distance (A), and decay of maximum velocity scaled by the growth of the $Y_{1/2}^T$ (B). In (A) and (B) markers are shown at only every 10th measurement location for clarity. The development length for each case is noted in (A) with a vertical line using the same line markers at either end.

Previous studies have also shown that in the far downstream region, $X/H > 20$, a logarithmic decay to velocity can be seen when scaled against the location of $Y_{1/2}^T$ as shown in equation (5.2),

$$\frac{U_{\max}}{U_0} = B \left[\frac{Y_{1/2}^T}{H} \right]^n \quad (5.2)$$

where U_{\max} is the local maximum value and U_0 is the exit velocity. Figure 5.5B shows the decay rate of velocity scaled using this equation, which better illustrates that a consistent slope can be seen for all of the Reynolds numbers. In this form, the decay rate is -0.61 ± 0.077 which is in good agreement with previous works that focused on the downstream section where the slopes were found to be on the order of ~ 0.575 (Eriksson, Karlsson et al. 1998; George, Abrahamsson et al. 2000). The agreement seen when scaling the velocity decay by the $Y_{1/2}^T$ indicates that the velocity decay and thus momentum transfer to the outflow is the dominate factor in causing these jets to spread. An equally important note is that while this process starts at different locations in the development regions the decay is Reynolds number independent and can be seen in both the fully developed and development region of the jet.

5.4.2. *Scaling of $Y_{1/2}^{T,B}$ and Y_{Umax} Locations*

The transfer of momentum from the core velocity decay causes the wall jet to spread, which in turn raises the location of $Y_{1/2}^T$ away from the wall as the flow moves downstream. Figure 5.6A shows the location of the $Y_{1/2}^T$ and $Y_{1/2}^B$ for the different Reynolds numbers as a function of streamwise location. For the $Y_{1/2}^T$ locations it is seen that in the development region the growth is linear and constant between Reynolds numbers. Averaging across the different Reynolds numbers produces a growth rate of 0.0595 ± 0.00168 , which is similar to previous studies for the fully developed regions, 0.073 ± 0.004 . As well as focusing on the fully developed region these studies also tended towards higher Reynolds numbers, $Re = 7,000 - 53,000$ (Launder and Rodi 1983; Karlsson, Eriksson et al. 1992; Eriksson, Karlsson et al. 1998). The reason for a slow growth rate in the development regions is due in part to the development length. As the diffusion of momentum from the core will provide the primary mechanism for the jet to spread, until the development length is reached and inviscid core is fully broken down, the jet growth rate will be diminished.

Figure 5.6B shows the behavior of $Y_{1/2}^B$ as a function of streamwise location. Due to the viscous effects near the wall the $Y_{1/2}^B$ does not naturally collapse as well as $Y_{1/2}^T$. Reynolds numbers 150 and 200 have clearly linear trends, with growth rates of 0.016. For the Reynolds numbers 750 and greater the average growth rates of $4.38 \times 10^{-3} \pm 1.49 \times 10^{-3}$ which is much lower than the growth rate seen for the $Y_{1/2}^T$. Previous work has shown the viscous effects from the wall are only seen over a short section of the velocity profile, much shorter than what is seen for typical boundary layer flows (Wynanski, Katz et al. 1992). This means that while viscous effects will influence the growth of $Y_{1/2}^B$ location the $Y_{1/2}^T$ location will have a resemblance much closer to a free jet. These different growth rates of the inner and outer region reemphasize the complex nature of these wall jets that are governed by multiple length scales.

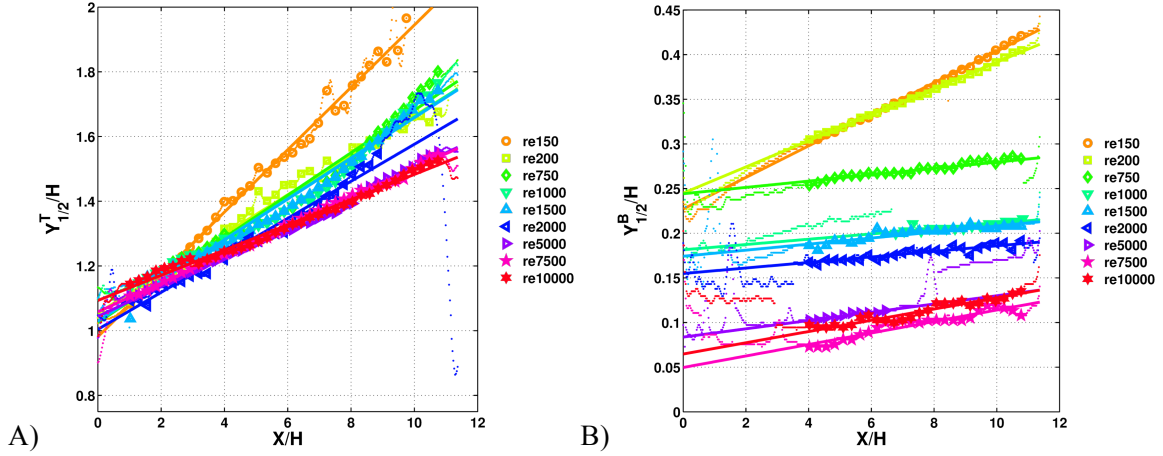


Figure 5.6. Growth the $Y_{1/2}^T$ height as a function of streamwise distance, (A), as well Growth of the $Y_{1/2}^B$ height as a function of streamwise distance. For each Reynolds number only every 10th marker is shown for clarity.

As Reynolds number increases the inner wall layer thickness will decrease moving the location of $Y_{1/2}^B$ closer to the wall. Because this region of the wall jet should have a behavior that resembles a classic boundary layer, we propose to use some of the same arguments to help with the scaling. Momentum thickness is commonly used for scaling boundary layers, but because this is not a true boundary layer with a bulk flow velocity, Launder and Rodi (1981) proposed a modified version of the equation where the velocity profile would be integrated from the wall to the location where U reaches its maximum value, as shown in equation (5.3):

$$\theta(x) = \int_0^{Y_{U_{\max}}} \frac{u}{U_0} \left(1 - \frac{u}{U_0} \right) dy \quad (5.3)$$

where u is the profile velocity, U_0 is maximum velocity at the current location, and $Y_{U_{\max}}$ is the vertical location of the maximum streamwise velocity. Computing the momentum thickness for all of the Reynolds numbers as a function of length produces results seen in Figure 5.7. As expected, the momentum thickness decreases with increasing Reynolds number and converges to a near zero growth rate at a Reynolds number of 5000. This decreasing momentum thickness means that the viscous effects are seen over a smaller percentage of profile as Reynolds number is increased.

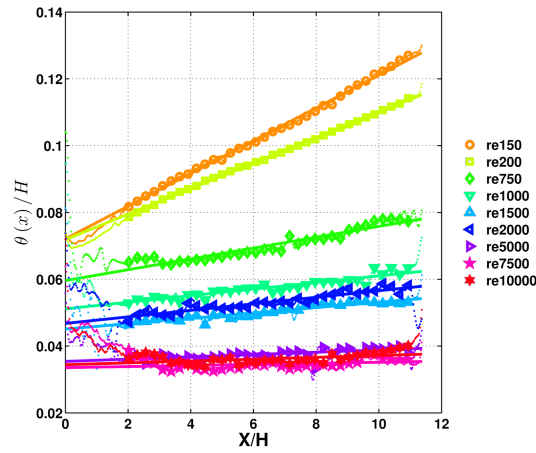


Figure 5.7. Growth of the momentum thickness of the wall jet, where markers are shown at only every 10th measurement location for clarity

Scaling the location of $Y_{1/2}^B$ by the momentum thickness as a function of streamwise location produces the results seen in Figure 5.8. For this plot we have normalized the streamwise distance by the respective development length, (L_d). Figure 5.8A shows the complete plot while Figure 5.8B shows a zoomed in portion near the development length. Figure 5.8B indicates that after the development equilibrium is reached and the ratio between $Y_{1/2}^B$ and θ reaches a constant value. For a better quantification of this result, Figure 5.8C provides the average $Y_{1/2}^B / \theta$ before and after the development length. The average value from all of the Reynolds numbers after the development length is 3.52 ± 0.37 , which means that on average the $Y_{1/2}^B$ location is at least three times larger than the momentum thickness. This constant relationship signifies that after the development length the growth of these two heights are constant with respect to one another. This constant relationship supports the argument that $Y_{1/2}^B$ can be universally scaled in the development region by the momentum thickness of the near wall boundary layer.

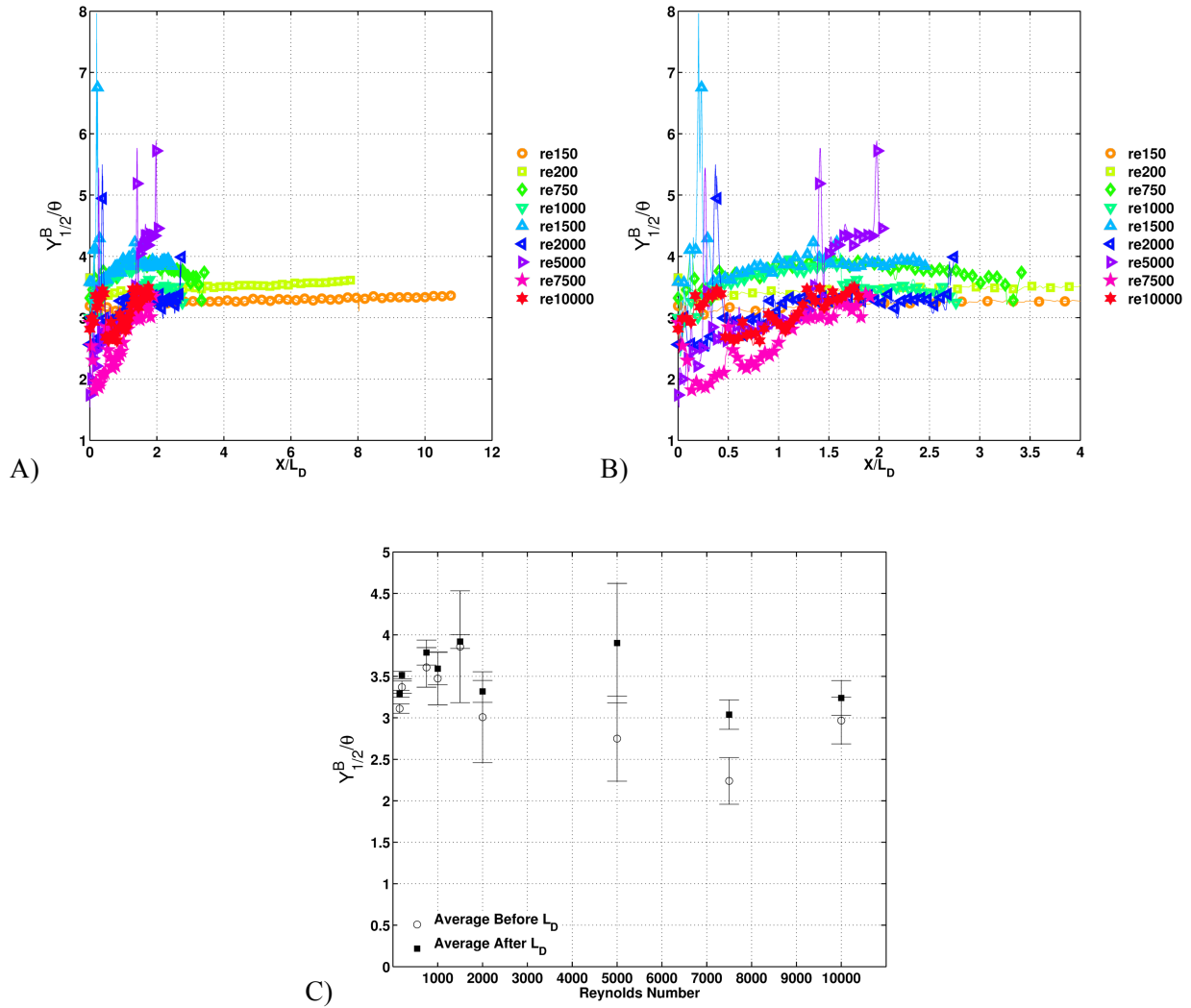


Figure 5.8. Growth of $Y_{1/2}^B$ normalized by the momentum thickness as a function of streamwise location normalized by the development length (A). (B) provides a zoomed in look at the early lengths.

The equilibrium after the development length is also seen in the profile velocity at the momentum thickness scaled by the local maximum. Using a spline interpolation we can determine the velocity that corresponds to the momentum thickness as a function of streamwise distance. Figure 5.9 depicts this relationship and shows that after the development length is reached this velocity ratio becomes constant. While the Reynolds numbers do not collapse, the equilibrium with respect to development length is still important as it reinforces the transition that occurs as the development length is reached.

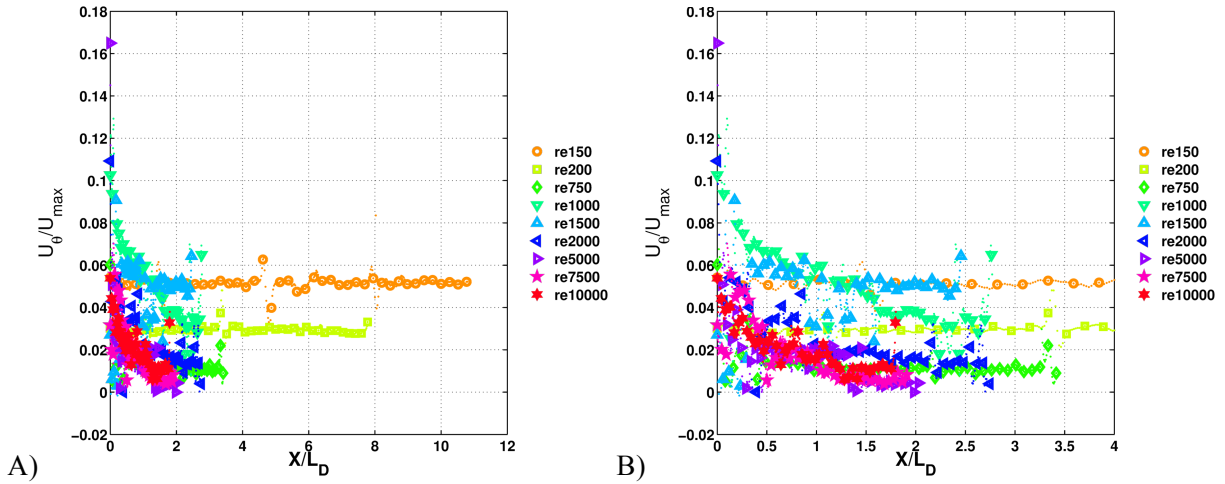


Figure 5.9. Ratio of profile velocity at the momentum thickness to the maximum U velocity. (B) provides a zoomed in view of (A).

In addition to scaling the $Y_{1/2}^T$ and $Y_{1/2}^B$ locations, Figure 5.10 shows the trend for the location of maximum streamwise velocity, U_{\max} . For the lowest two Reynolds numbers it is seen that the location grows linearly over the developing region, meaning that as the jet develops it moves away from the wall in a linear fashion. For the other Reynolds numbers a parabolic shape is seen. It should be noted that near the exit of the jet it is difficult to experimentally determine the location of U_{\max} as the profile is a top-hat shape and many locations have the same value. The parabolic shape is due to the fact that as the jet first exits the slot, momentum is transferred more quickly to the outer flow than what is lost due to viscous effects. The asymmetry in the momentum diffusion leads to asymmetry in the velocity core as a function of streamwise location. By the time the peak velocity begins to decay the profile has taken a more fully developed form and begins a more self-similar growth with streamwise distance.

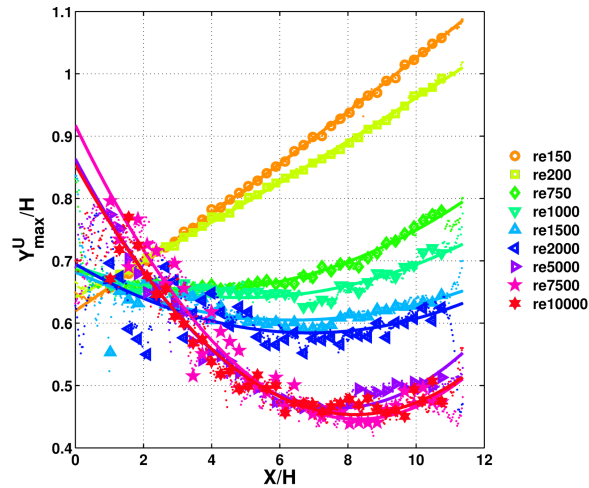


Figure 5.10. Location of U_{\max}^U as a function of streamwise location.

5.4.3. Turbulent Statistics and Scaling

Figure 5.11 and Figure 5.12 show the Reynolds stress profiles for increasing downstream distances normalized by the jet exit velocity. While previous works did not report results for this development region, the downstream locations have values that are in agreement with previously published works (Launder and Rodi 1983; George, Abrahamsson et al. 2000). Near the exit, Figure 5.11A shows the existence of two dominant peaks in the streamwise Reynolds stress values which occur at the near wall location and in conjunction with the location of $Y_{1/2}^T$ which is to be expected, as this position should be the location of the upper shear layer of the jet. As the jet progresses downstream, Figure 5.11B-D, a spread is seen in the Reynolds stress profile near the $Y_{1/2}^T$ location which correlations with the growth of the shear layer. Momentum is transferred from the jet core by way of turbulent fluctuations in the upper shear layer. As the jet develops, more momentum is transferred and thus the width of the shear layer grows. Because of the lack of particles in the external flow, some false peaks in Figure 5.11A were the result of erroneous correlations.

The second peak in Reynolds stresses, seen near the wall, is lower in magnitude in comparison to the upper peak for the low Reynolds number cases (150 and 200), while becoming more dominant for the

higher Reynolds numbers. The width of the lower peak is much tighter in comparison to the upper peak as the length scale for the near wall layer is much smaller than that seen with the free shear layer. As will be shown in the following section, these near wall fluctuations contribute the vortex formation occurring in the near wall boundary layer.

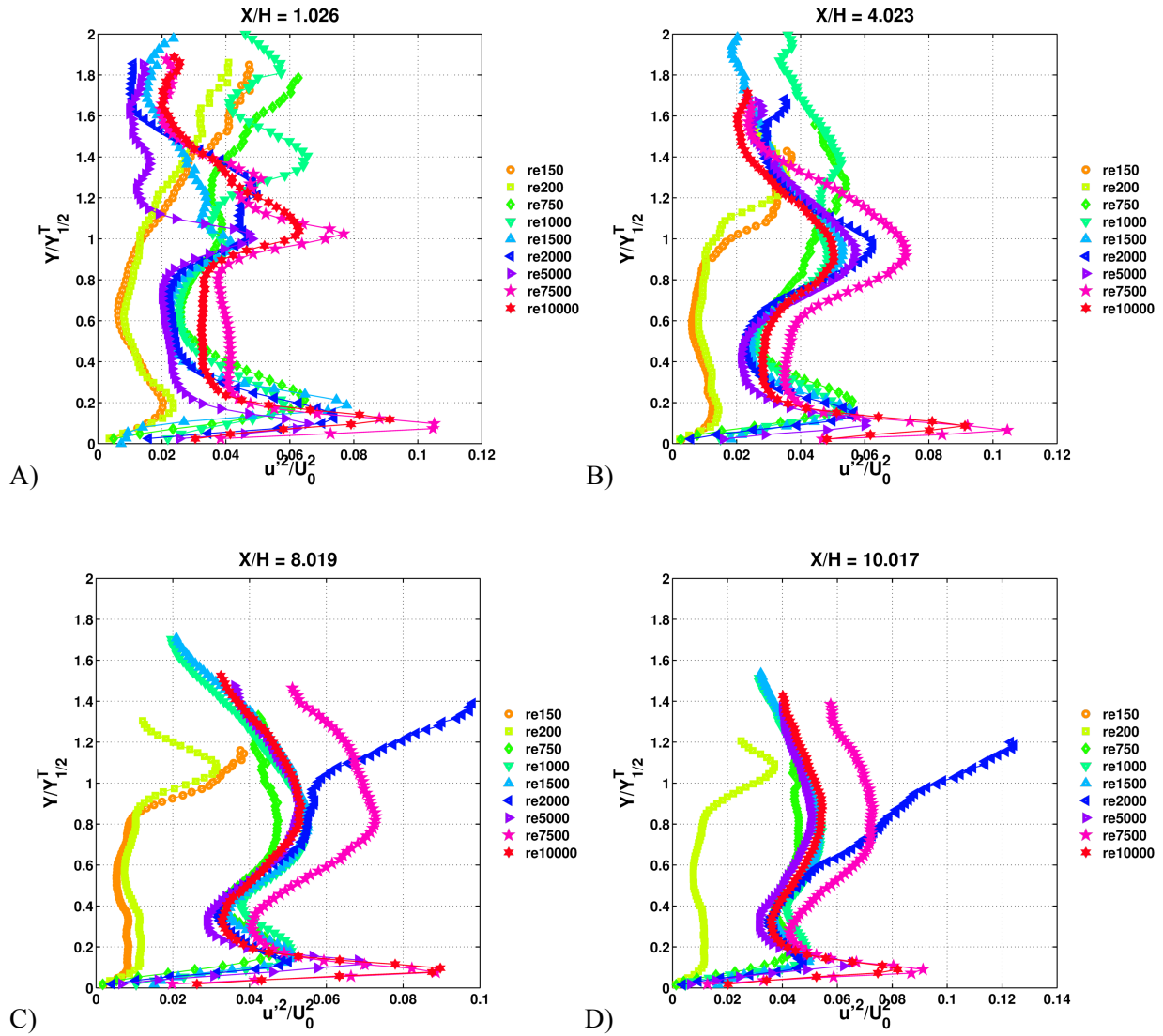


Figure 5.11. Profiles of streamwise velocity fluctuation, u' , normalized by the exit velocity, U_0 , for down stream distances of $X/H = 1$ (A), $X/H = 4$ (B), $X/H = 8$ (C), and $X/H = 10$ (D).

For the wall normal Reynolds stresses, Figure 5.12, the profiles are characterized primarily by a peak located at the upper shear layer without additional peaks near the wall. This profile shape has been

reported in previous studies (Eriksson, Karlsson et al. 1998). Again there is a spread in the wall normal fluctuation at the upper shear layer similar to that seen with the streamwise Reynolds stresses. As a large amount of diffusion and mixing will take place in this shear layer it is to be expected that this will coincide with high streamwise and wall normal fluctuations.

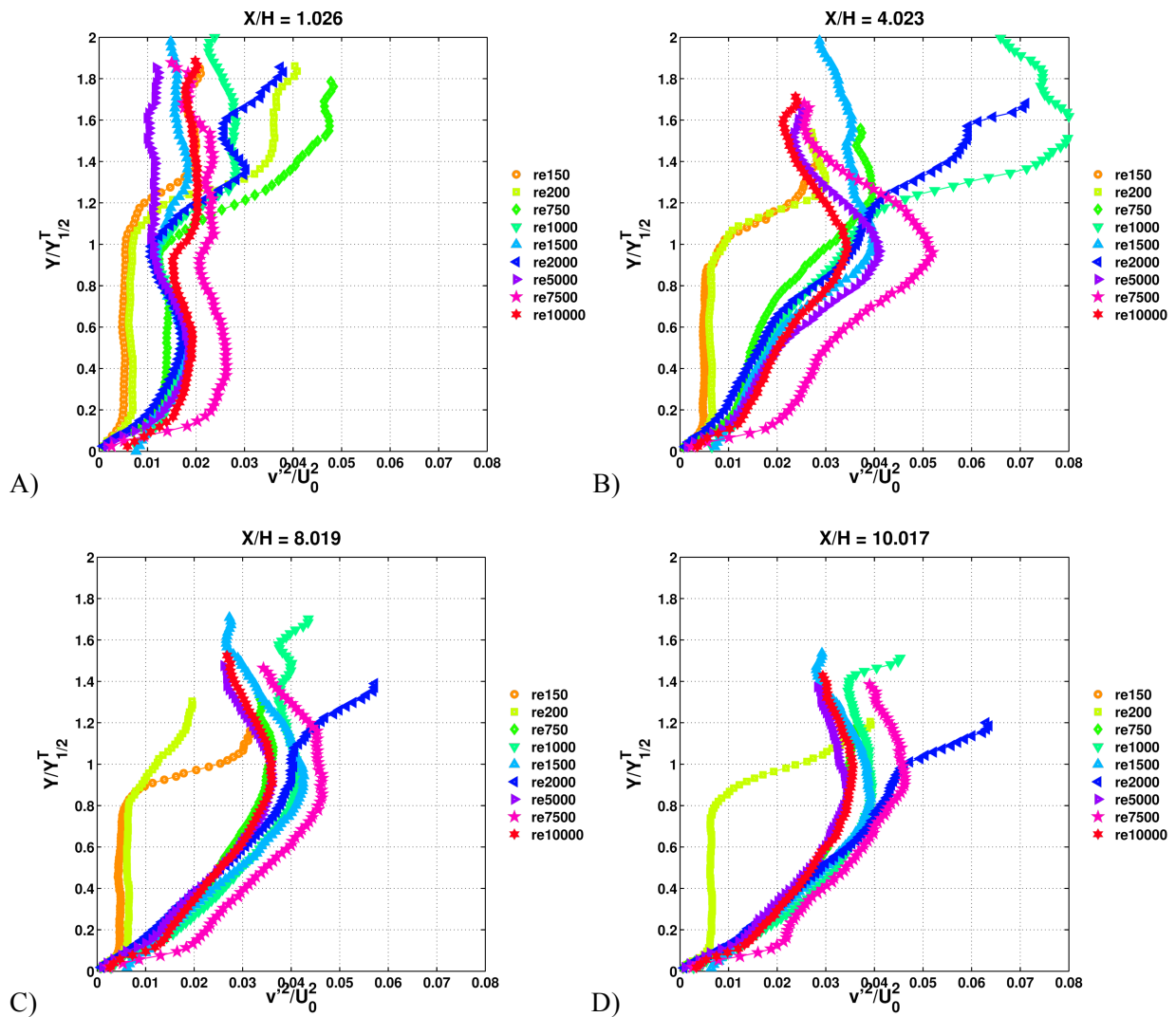


Figure 5.12. Profiles of wall normal velocity fluctuation, v' , normalized by the exit velocity, U_0 , for downstream distances of $X/H = 1$ (A), $X/H = 4$ (B), $X/H = 8$ (C), and $X/H = 10$ (D).

Figure 5.11 and Figure 5.12 indicate that the vertical locations of peak Reynolds stress appears to be correlated the $Y_{1/2}^T$ and $Y_{1/2}^B$ locations. Figure 5.13 quantifies this observations by plotting the location of

maximum u' and v' as a function of $Y_{1/2}^T$ and $Y_{1/2}^B$. In an effort to reduce the effect of noise and erroneous peaks from the outer flow, the first maximum location above the U_{\max} location was used to correlate with $Y_{1/2}^T$, while the first maximum beneath U_{\max} was chosen for scaling against $Y_{1/2}^B$. The locations of the peak streamwise Reynolds stress, Figure 5.13A, shows clear agreement with $Y_{1/2}^T$ location. As we expect the shear layer to be identified by a location of maximum Reynolds stress this figure shows a strong connection between the location of the shear layer the $Y_{1/2}^T$. For the lowest two Reynolds numbers (150 and 200) some disagreement is seen, which is most likely the result of insufficiently resolving the outer flow. Poor image quality at the downstream location for Re 2000 resulted in some disagreement with the other cases. The location of the near wall peak in the u' profiles shows a strong agreement with the $Y_{1/2}^B$ location, Figure 5.13B.

Figure 5.13C shows that the maximum location in wall normal Reynolds stress again shows a strong agreement with the locations of $Y_{1/2}^T$. This continues to support the notion that $Y_{1/2}^T$ is coincident with the shear layer location in the development region. Due to the fact that no peak near the wall was seen for the v' data, scaling with respect to $Y_{1/2}^B$ was not included. While the $Y_{1/2}^T$ and $Y_{1/2}^B$ locations have been primarily used to scale velocity profiles, this work shows that these parameters also aid in scaling the Reynolds stress in the development regions, which has previously not been shown.

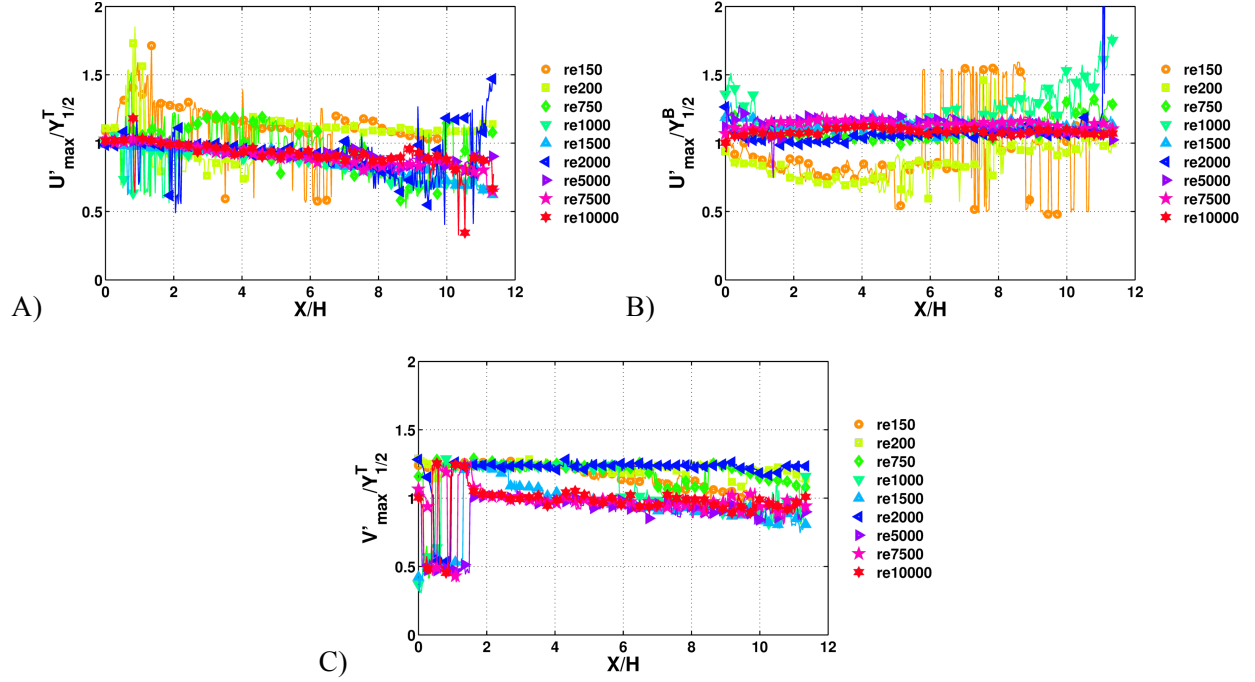


Figure 5.13. Locations of maximum streamwise, u' , and wall normal, v' , Reynolds stress normalized by the $Y^T_{1/2}$ and $Y^B_{1/2}$ locations. A) and B) show maximum u' locations normalized by the $Y^T_{1/2}$ and $Y^B_{1/2}$ heights respectively while C) show locations for v' normalized by $Y^T_{1/2}$.

5.4.4. Vortex Identification

As vortex formation and interaction will be a factor in the development process for these jets, this work looks to quantify the role of vortices in development region. In order to identify and determine the location of vortices the λ_{ci} vortex identification scheme (λ_{ci} -VIS) was applied on the instantaneous data after filtering with proper orthogonal decomposition (POD) (Chong, Perry et al. 1990; Zhou, Adrian et al. 1999). The λ_{ci} -VIS states that a vortex can be identified by first finding the eigenvalues of the velocity gradient tensor, Equations (5.4) and (5.5).

$$0 = \det \left(\frac{du_i}{dx_j} - \lambda I \right) \quad (5.4)$$

$$C = \max(\text{Im}(\lambda)) \quad (5.5)$$

where Im denotes the imaginary part of the complex term λ . It has been shown that a vortex exists when a complex eigenvalue exists (Chong, Perry et al. 1990; Zhou, Adrian et al. 1999; Christensen and Adrian 2001). Experimental data inherently has a given amount of noise, which can produce a λ_{ci} without the presence of a vortex. For this reason a threshold for the λ_{ci} value was used in order to prevent false positives from corrupting the data. The threshold was held constant for all cases by normalizing the velocity gradients by the inlet velocity and the physical vector spacing. This process allowed for a global threshold with a value of 0.3 to be used for all Reynolds numbers. Vortex circulation was also calculated by computing the line integral of the velocity along the λ_{ci} iso-contour of the identified vortex. Circulation was normalized by slot height and free-stream velocity (Gogineni, Shih et al. 1993).

From the instantaneous spatial data, it is possible to see the formation and ejection of near wall vortices in the flow. Traditionally when studying vortex interaction in boundary layer flows cross power-spectra is often used (Bajura and Szewczyk 1975; Durbin and Wu 2007). Due to the high velocity and high image magnification a sampling rate of 2kHz was not sufficient to fully resolve the temporal behavior; however, information can still be gleaned from this data set. Figure 5.14 show a series of non-consecutive snap shots of the vorticity field for the Reynolds number 1000 case along with the location of vortices as well as an iso-contour of the Q2 burst events. Q2 burst events, shown by quadrant analysis, have been used previously for describing vortex behavior in turbulent boundary layer flows (Robinson 1991; Cantwell 1993). Previous wall jet studies have qualitatively shown, for a limited number of Reynolds, that burst events will occur when vortices from the outer flow approach the wall (Bajura and Szewczyk 1975; Gogineni, Visbal et al. 1999).

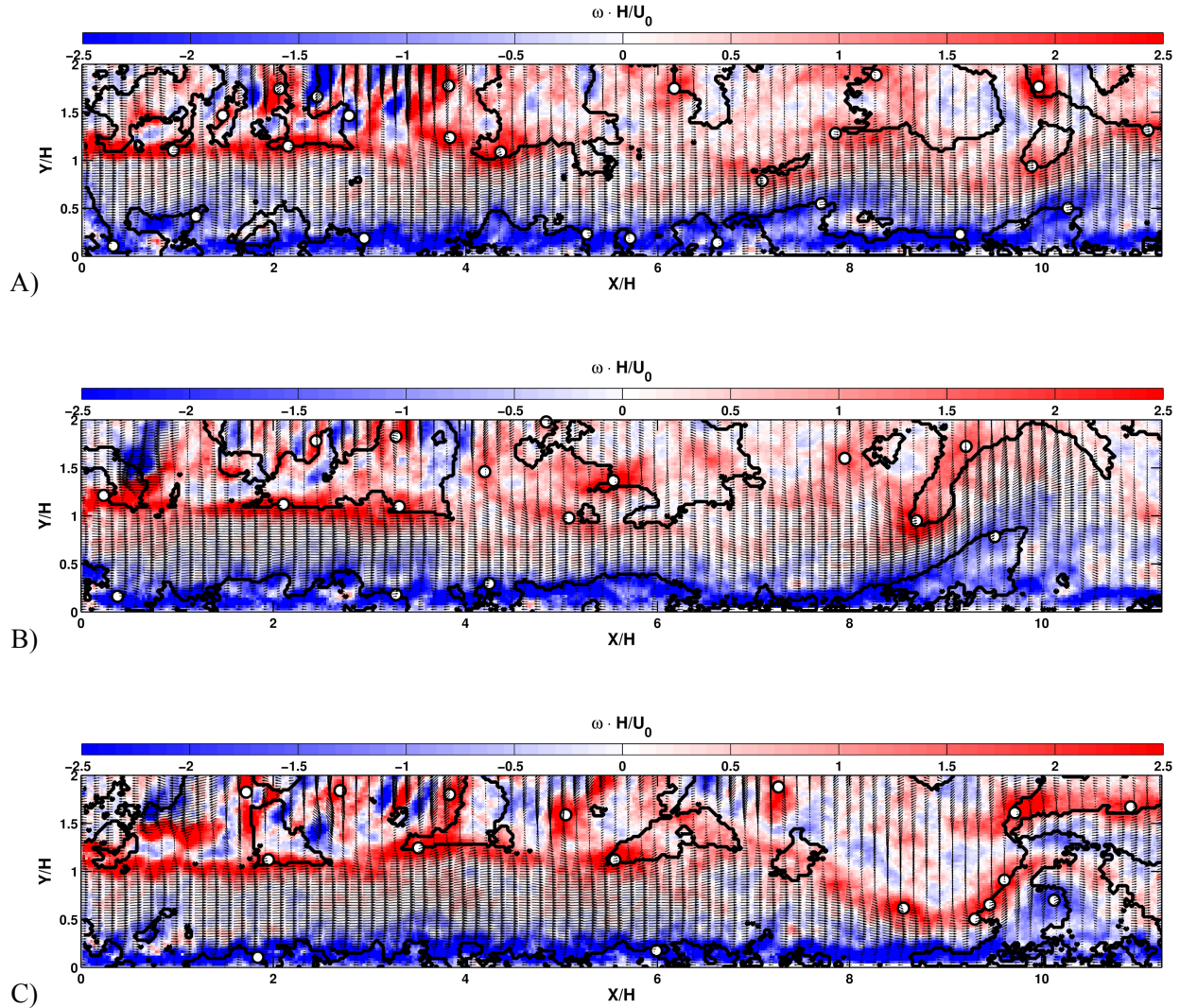


Figure 5.14. Snap shots of near wall vortex ejection for the Re 1000 case. The color contour shows normalized vorticity while the white circles indicate vortices identified with the λ_{ci} method. The iso-contour lines enclose Q2 events that are seen in the field.

Figure 5.14A depicts this process. At a streamwise location of $X/H=7$ two vortices can be seen with one vortex in the bulk of the flow while the other is near the wall with the burst event forming underneath. At this location, elevated levels of vorticity have begun to detach from the wall with a vortex located at the head, suggesting the development of hair-pin vortex (Zhou, Adrian et al. 1999; Durbin and Wu 2007). The Q2 event beneath the near wall vortex, supports that this event is an ejection away from the wall. A similar event also exists at $X/H = 10$. Figure 5.14B at X/H of 9 shows a more evolved

ejection where the near wall vortex has moved further away from the wall and a clear Q2 event is present underneath the near wall vortex. A nearly completed ejection can be seen in Figure 5.14C at X/H of 10, where the near wall vortex has separated from the wall. This behavior of near wall vortex ejection is seen in this development region for all of the Reynolds numbers except for Re 150 and 200. Because these cases have a more laminar behavior in this development region there is less interaction between the upper and lower shear layers and their transition will take place further down stream, outside of the region measured in this study.

Figure 5.15 more directly quantifies the location of burst events as a function of wall normal location. This figure shows a histogram of the burst events for the different Reynolds numbers as a function of vertical location. For all the Reynolds numbers studied, the highest probability of a burst event is seen near the wall. A rise in burst event frequency can be seen near the out shear layer but with reduced strength when compared to the near wall Figure 5.15A. Figure 5.15B shows the peak in burst events near $Y_{1/2}^B$ location. These near wall burst events eject near wall vortices away from the wall and into the bulk flow diffusing momentum as the jet develops.

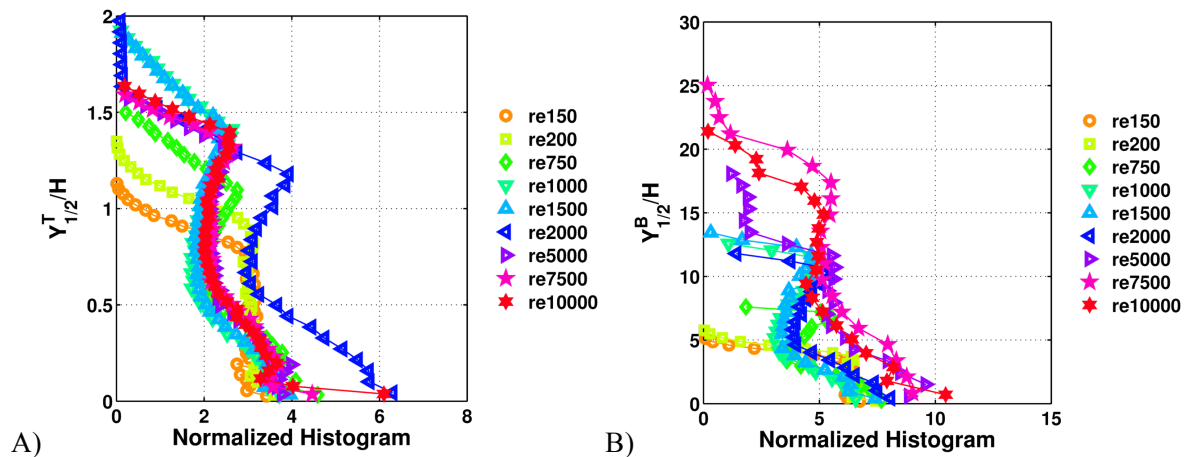


Figure 5.15. Histogram of burst versus their vertical location scale by $Y_{1/2}^T$ (A) and $Y_{1/2}^B$ (B).

To show the vertical location of vortex formation, Figure 5.16 displays normalized histograms for all of the vortices with respect to the $Y_{1/2}^T$ and $Y_{1/2}^B$. This figure shows that as Reynolds number increases, vortex population moves from the near wall region to the inner layer. Again for the higher Reynolds numbers, vortices occur most frequently at the $Y_{1/2}^T$ location. For Reynolds numbers 150-200 a spike is seen in the histogram near the wall showing the high population of vortices near the wall. For Reynolds numbers 750 - 1500 this spike has increased in percentage, which could indicate a transitional Reynolds number, where shear layer and near wall flow are becoming equally important to the formation of vortices. The presence of elevated burst events near the wall, Figure 5.15, helps to support the notion that the outer vortices are contributing to the ejection near the wall. For the highest Reynolds number (2,000-10,000) the near wall spike is far less significant because of the prevalence of vortex formation at the $Y_{1/2}^T$ location.

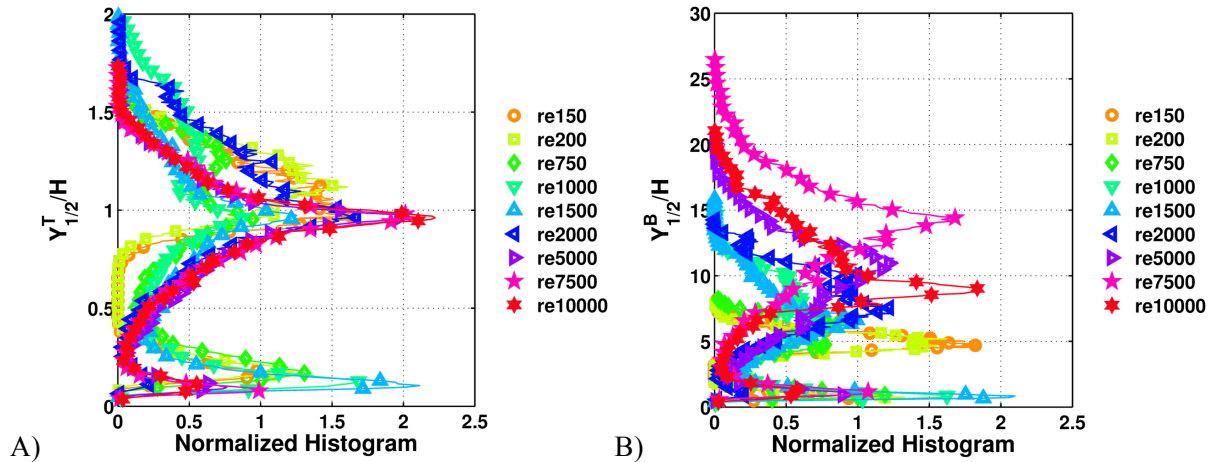


Figure 5.16. Normalized histograms for the vortex locations in the vertical direction with the vertical axis normalized by the $Y_{1/2}^T$ and $Y_{1/2}^B$ respectively.

Figure 5.17 shows the distribution of normalized circulation values for the different Reynolds numbers. Once normalized, this wide range of Reynolds number produces circulation values that fall close together. Figure 5.17 B and C shows the most probable clockwise and counter-clockwise (negative and positive circulation respectively) circulation values as well as their normalized histogram values,

which illustrates the difference between these Reynolds numbers. From this figure, it is seen that vortices for Reynolds numbers 150-200 have a high concentration of vortices with a normalized strength of -0.07. The negative circulation indicates that these vortices are most likely near wall vortices due to the direction of rotation as well as the information learned from Figure 5.16. As Reynolds number is increased the percentage of near wall vortices with negative circulation increases for the $Re=750 - 1500$ cases. The influence of the large-scale shear layer structures, as seen from Figure 5.14, is the most pronounced in these cases. As these structures in the shear layer approach the wall they will feed energy to the near wall structure, which leads to an increase in circulation in these vortices and promote an ejection away from the wall. This increase in interaction between the layers for these Reynolds number suggests that this is a transitional range as the flow has evolved passed the laminar behavior and is moving towards a more turbulent regime. As Reynolds number is increased further, the circulation near the wall decreases while the number of positive circulation remains relatively constant. While some interaction between the top shear layer and the near wall boundary layer still exists, the presence of the high momentum core limits the interaction in the development region. While these circulation strengths are different from the values first reported by (Gogineni, Shih et al. 1993) their analysis only used vorticity contours to determine vortex location and size instead of a vortex identification scheme such as the λ_{ci} -VIS. This work provides a more complete look at not only the vortex production in the development region but also the effect of Reynolds number on this vortex production. As vortex production can play a large role in the transfer of momentum, it is important to understand its behavior to better understand the development of the wall jet.

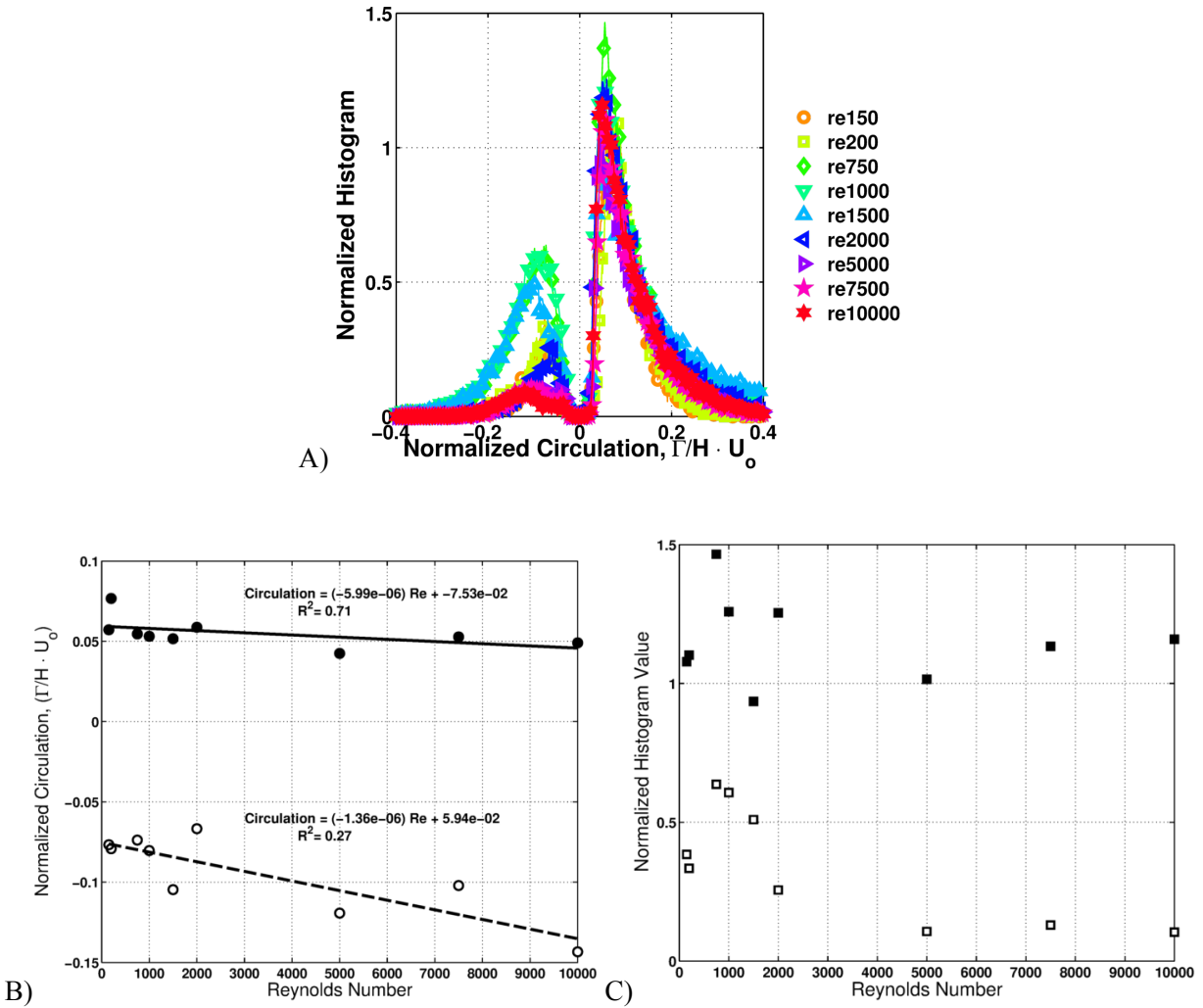


Figure 5.17. Normalized histogram of normalized circulation strengths for the different Reynolds numbers(A) as well as peak circulation values from the histogram (B), and their relative contribution in the distribution (B). The open symbols show negative circulation (clock wise rotation) while the closed symbols represent positive circulation (counter-clock wise rotation)

5.5. Conclusion

This work has provided an in-depth look at the development region for wall jets across a wide range of Reynolds numbers. The effect of momentum diffusion at the jet exit has an effect on many of the characteristics that make up the wall jet. The diffusion of momentum is most clearly seen in the development length for these different Reynolds numbers, which has not been previous investigated for wall jets. It was shown that as Reynolds number is increased, the development length increases. Due to

the influence of the wall, the development lengths for wall jets are seen to be shorter than what is proposed for free round jets. While the development lengths is a function of Reynolds number, this worked showed that the decay in maximum velocity is constant after the development length, with an average decay rate of -0.61 ± 0.077 , which is in good agreement with previous studies. As Reynolds number is increased, the location of maximum streamwise velocity was seen to become parabolic as function of streamwise location. This shape is the result of momentum diffusing faster to the outer shear layer than what is lost to the near wall effects.

The diffusion of momentum also directly impacts the growth of the profile heights that are typically used to scale these jets. It has been shown that the growth of the $Y_{1/2}^T$ height is constant respect to Reynolds number, producing an average growth rate of 0.0595 ± 0.00168 . Up until now, previous studies focused on the fully developed self-similar region, a growth rate in the development region is missing from current literature and plays an important role in the development of these jets. In an effort to scale the growth rate for the $Y_{1/2}^B$ location, this work has proposed to normalize the height by a modified boundary layer momentum thickness. This procedure has shown to produce better agreement between the Reynolds numbers and suggests a more universal collapse of the height in the fully developed region. These heights are also useful when scaling the location of Reynolds stress, which has not been addressed in previous studies. It was observed that the peak locations in the Reynolds stress coincide with the locations of $Y_{1/2}^T$ and $Y_{1/2}^B$, which places grater significance on these scaling terms in the development region. Vortex identification was also applied to this data due to the direct impact of vortex production on momentum transfer and jet development. The results showed that there is a correlation between the location of vortices and the $Y_{1/2}^T$ and $Y_{1/2}^B$ heights. It was also seen that for lower Reynolds number cases there was a higher probability of near wall vortices, which transitioned to a higher probability in the shear location as the Reynolds number increased. These findings help to provide a more complete

understanding of the wall jet in the development region and illustrate the dominant effect of momentum transfer on the behavior of the developing wall jet.

5.6. References

- Afzal, N. (2005). "Analysis of power law and log law velocity profiles in the overlap region of a turbulent wall jet." Proceedings of the Royal Society A: Mathematical, Physical and Engineering Sciences **461**(2058): 1889-1910.
- Amitay, M. and J. Cohen (1997). "Instability of a two-dimensional plane wall jet subjected to blowing or suction." Journal of Fluid Mechanics **344**: 67-94.
- Bajura, R. A. and A. A. Szewczyk (1975). "Experimental Investigation of Laminar Two-Dimensional Plane Wall Jet." Physics of Fluids **13**(7).
- Barenblatt, G. I., a. J. Chorin, et al. (2005). "The turbulent wall jet: a triple-layered structure and incomplete similarity." Proceedings of the National Academy of Sciences of the United States of America **102**(25): 8850-8853.
- Cantwell, B. J. (1993). "On the Behavior of Velocity-Gradient Tensor Invariants in Direct Numerical Simulations of Turbulence." Physics of Fluids a-Fluid Dynamics **5**(8): 2008-2013.
- Chong, M. S., A. E. Perry, et al. (1990). "A general classification of three-dimensional flow fields." Physics of Fluids A **2**(5): 765-777.
- Christensen, K. T. and R. J. Adrian (2001). "Statistical evidence of hairpin vortex packets in wall turbulence." Journal of Fluid Mechanics **431**: 433-443.
- Chun, D. H. and W. H. Schwarz (1967). "Stability of the Plane Incompressible Viscous Wall Jet Subjected to Small Disturbances." Physics of Fluids **10**(5): 911-915.
- Durbin, P. and X. Wu (2007). "Transition Beneath Vortical Disturbances." Annual Review of Fluid Mechanics **39**(1): 107-128.
- Eckstein, A. and P. P. Vlachos (2009). "Assessment of advanced windowing techniques for digital particle image velocimetry (DPIV)." Measurement Science and Technology **20**(7): 075402-075402.
- Eckstein, A. and P. P. Vlachos (2009). "Digital particle image velocimetry (DPIV) robust phase correlation." Measurement Science & Technology **20**(5).
- Eckstein, A. C., J. Charonko, et al. (2008). "Phase correlation processing for DPIV measurements." Experiments in Fluids **45**(3): 485-500.

- Eriksson, J., R. Karlsson, et al. (1998). "An experimental study of two dimensional plane turbulent wall jet." Experiments in Fluids **25**: 50-60.
- Everson, R. and L. Sirovich (1995). "Karhunen-Loeve Procedure for Gappy Data." Journal of the Optical Society of America **12**(8): 1657-1664.
- George, W. K., H. Abrahamsson, et al. (2000). "A similarity theory for the turbulent plane wall jet without external stream." Journal of Fluid Mechanics **425**: 367-411.
- Glauert, M. B. (1956). "The wall jet." Journal of Fluid Mechanics **1**(06): 625-625.
- Gogineni, S. and C. Shih (1997). "Experimental investigation of the unsteady structure of a transitional plane wall jet." Experiments in Fluids **23**(2): 121-129.
- Gogineni, S., C. Shih, et al. (1993). "PIV Study of a Two-Dimensional Transitional Wall Jet." AIAA **1**.
- Gogineni, S., M. Visbal, et al. (1999). "Phase-resolved PIV measurements in a transitional plane wall jet: a numerical comparison." Experiments in Fluids **27**(2): 126-136.
- Grissom, D., B. Smith, et al. (2007). "Rough Wall Boundary Layer Noise: An Experimental Investigation." AIAA paper: 1-35.
- Hall, J. W. and D. Ewing (2007). "Three-Dimensional Turbulent Wall Jets Issuing from Moderate-Aspect-Ratio Rectangular Channels." AIAA Journal **45**(6): 1177-1186.
- Karlsson, R. I., J. Eriksson, et al. (1992). "LDV Measurements in a Plane Wall Jet in a Large Enclosure."
- Launder, B. E. and W. Rodi (1981). "The Turbulent Wall Jet." Progress in Aerospace Sciences **19**: 81-128.
- Launder, B. E. and W. Rodi (1983). "The turbulent wall jet - measurements and modeling." Annual Review of Fluid Mechanics **15**: 429-459.
- Lee, J. J. H. and V. H. Chu (2003). Turbulent Jets and Plumes: a Lagrangian Approach, Springer.
- Robinson, S. K. (1991). "Coherent Motions in the Turbulent Boundary-Layer." Annual Review of Fluid Mechanics **23**: 601-639.
- Scarano, F. (2002). "Iterative image deformation methods in PIV." Measurement Science and Technology **13**.
- Scarano, F. and M. L. Riethmuller (1999). "Iterative multigrid approach in PIV image processing with discrete window offset." Experiments in Fluids **26**(6): 513-523.

- Schneider, M. E. and R. J. Goldstein (1994). "Laser Doppler measurement plane wall jet in a two-dimensional plane wall jet." Physics of Fluids **6**(9): 3116-3129.
- Sirovich, L. (1989). "Chaotic Dynamics of Coherent Structures." Physica D **37**: 126-145.
- Wang, H. W. and A. W. K. Law (2002). "Second-order integral model for a round turbulent buoyant jet." Journal of Fluid Mechanics **459**: 397-428.
- Westerweel, J. and F. Scarano (2005). "Universal outlier detection for PIV data." Experiments in Fluids **39**(6): 1096-1100.
- Wynanski, I., Y. Katz, et al. (1992). "On the applicability of various scaling laws to the turbulent wall jet." Journal of Fluid Mechanics **234**: 669-690.
- Zhou, J., R. Adrian, et al. (1999). "Mechanisms for generating coherent packets of hairpin vortices in channel flow." Journal of Fluid Mechanics **387**: 353-396.

6. Conclusions

This dissertation presents work for the direct determination of three-dimensional time varying flow structures. There are a few important conclusions that should be reiterated. In chapter 2 it was shown that the newly proposed adaptive “gappy” POD procedure produces reconstructed fields with higher accuracy in comparison to other currently available reconstruction methods. This procedure has also been shown to be effective even when the amount of missing information reaches as high as 80%.

Chapter 3 provided a novel methodology for directly determining FTLE fields from experimental particle image data. This new procedure takes advantage of particle motion inherently captured in these images to reduce computational cost by removing the need for numerical integration. Additionally, the method produces superior results especially in low seeding density environments. Experimental data from an unconfined vortex ring was used to demonstrate the applicability of this method for realistic conditions. The resulting FTLE field was in good agreement with what has been shown in literature and out performed the other methods tested in this study.

The demonstration of this new FTLE methodology on inertial particles in a three-dimensional flow field was executed in chapter 4. Using tomographic imaging, it was possible to capture both neutrally buoyant and inertial particles simultaneously, which could then be separated numerically based on their apparent size. This newly developed FTLE methodology was then applied to the different particle groups in an effort to demonstrate how this technique could be used to study inertial particle behavior. A clear difference in the FTLE fields was seen between the inertial particles and the flow tracers indicating the method’s applicability to multiphase flows. The resulting FTLE fields were also compared with currently published methods for demonstrating particle clustering, which showed some agreement.

The final chapter of this worked discussed the behavior of wall jets in the development region for a wide range of Reynolds numbers. While the vast majority of previous studies have investigated wall jets

in the downstream self-similar region, this work focuses on the development region. It was shown that the transfer of momentum plays a large roll development of these jets. A clear Reynolds number dependence on the development length was shown. Higher Reynolds number jets exhibited a longer development length suggesting that less momentum was transferred to the surrounding flow over this region. This result was confirmed when observing the growth of the $Y_{1/2}^T$. As momentum is transferred out of the core, the jet's profile begins to expand. Jets with larger Reynolds number and longer development lengths correspond to a slower growth of the $Y_{1/2}^T$ locations in comparison to lower Reynolds number jets. A connection was also shown between the locations of $Y_{1/2}^T$ and $Y_{1/2}^B$ and the locations of peak Reynolds stress. As the jet develops and momentum is transferred out of the core, the Reynolds stresses showed increased fluctuations at the upper shear layer coinciding with the $Y_{1/2}^T$ location. This work also showed the roll of vortex formation in the development region. Vortices are seen to interact between the near wall and free shear layer. This interaction leads to an ejection from the wall where vortices are produces and enter the bulk flow.